

N72-20898

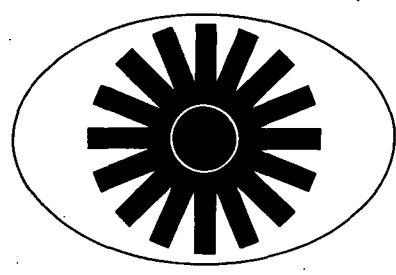
AN ANALYTICAL AND EXPERIMENTAL STUDY OF THE BEHAVIOR OF
SEMI-INFINITE METAL TARGETS UNDER HYPERVELOCITY IMPACT

TEES-9075-CR-71-02

by

BASAVARAJU CHAKRAPANI AND JAMES L. RAND

CASE FILE
COPY



TEES

TEXAS ENGINEERING EXPERIMENT STATION
TEXAS A & M UNIVERSITY
COLLEGE STATION TEXAS 77843

October 1971

Prepared for

NASA Manned Spacecraft Center

Meteoroid Sciences

Houston, Texas 77058

Under Contract NGR 44-001-106

AN ANALYTICAL AND EXPERIMENTAL STUDY OF THE BEHAVIOR OF
SEMI-INFINITE METAL TARGETS UNDER HYPERVELOCITY IMPACT

TEES-9075-CR-71-02

by

BASAVARAJU CHAKRAPANI AND JAMES L. RAND

October 1971

Prepared for

NASA Manned Spacecraft Center

Meteoroid Sciences

Houston, Texas 77058

Under Contract NGR 44-001-106

Prepared by

Texas Engineering Experiment Station

Texas A&M University

College Station, Texas 77843

FOREWORD

This report, TEES 9075-CR-71-02, is submitted by Texas Engineering Experiment Station in partial fulfillment of Contract NGR 44-001-106. It is also submitted by Basavaraju Chakrapani to the Graduate College of Texas A&M University in partial fulfillment of the requirement for the degree of Doctor of Philosophy in Mechanical Engineering in October 1971.

ABSTRACT

An Analytical and Experimental Study of the
Behavior of Semi-infinite Metal Targets Under
Hypervelocity Impact (December 1971)

Basavaraju Chakrapani, B.E., Andhra University;
M. Tech., Indian Institute of Technology;

Directed by: Dr. James L. Rand

In this study the material strength and strain rate effects associated with the hypervelocity impact problem were considered. A yield criterion involving the second and third invariants of the stress deviator and a strain rate sensitive constitutive equation were developed. The part of total deformation which represents change in shape is attributable to the stress deviator. Constitutive equation is a means for analytically describing the mechanical response of a continuum under study. The accuracy of the yield criterion was verified utilizing the published two and three dimensional experimental data. The constants associated with the constitutive equation were determined from one dimensional quasi-static and dynamic experiments. Hypervelocity impact experiments were conducted on semi-infinite targets of 1100 aluminum, 6061 aluminum alloy, mild steel, and commercially pure lead using spherically shaped and normally incident pyrex projectiles. The strain rates encountered in such impacts were determined in the vicinity of the axis of symmetry taking into account the initial

hydrodynamic and the subsequent material strength affected regimes. The determination of strain rates was based on the attenuation of the peak pressure with the advancing shock front in the target. Using the developed constitutive equation and the strain rates in the material strength affected regime, the stress-strain curve and the dynamic yield strength were obtained. This dynamic yield strength was adapted into an existing penetration equation and the crater depths were predicted.

Good agreement was found to exist between the theory and experiment indicating that the dynamic yield strength of the target material is an important parameter. The error in predicting the crater depths was within 5% except in the case of lead targets. The discrepancy with reference to lead targets may be attributed to the complex behavior of lead in quasi-static as well as dynamic testing because of its soft nature and probable thermal effects.

ACKNOWLEDGEMENT

The author wishes to express his regard and sincere appreciation to Dr. James L. Rand for his invaluable guidance and encouragement. The author is especially grateful to Dr. J. George H. Thompson for his encouragement, help and suggestions while serving as the chairman of the committee. He is also grateful to Dr. H. S. Wolko, Dr. W. B. Ledbetter, Dr. H. J. Sweet, and Dr. W. S. McCulley for their suggestions while serving as members of the committee.

The author wishes to acknowledge his gratitude to Mr. B. G. Cour-Palais of NASA-Manned Spacecraft Center, Houston, and Mr. James Kester of Lockheed Electronic Company for their assistance in conducting the Hypervelocity Impact Experiments and to Mr. Charles E. Nelson and Professor C. Hays for their coordination. Finally the author is thankful to Dr. J. George H. Thompson and Dr. B. P. C. Sekhara Rao who suggested and helped extensively for the author's continuation toward Ph.D. This research was supported by NASA Grant NGR 44-001-106.

TABLE OF CONTENTS

	Page
ABSTRACT.	iii
ACKNOWLEDGEMENT	v
TABLE OF CONTENTS	vi
LIST OF TABLES.	viii
LIST OF FIGURES	ix
NOMENCLATURE.	xi
CHAPTER	
I. INTRODUCTION	1
II. LITERATURE REVIEW.	4
III. OBJECTIVES	12
IV. YIELD CRITERION.	15
V. STRAIN RATE SENSITIVE CONSTITUTIVE EQUATION	25
VI. EXPERIMENTAL PROCEDURE	36
Need for Experimentation	36
Quasi-Static Tests	38
Dynamic Testing.	44
Hypervelocity Impact Experiments	49
VII. DETERMINATION OF STRAIN RATES IN HYPERVELOCITY IMPACT	53
General Discussion of the Problem.	53
Determination of the Initial Pressure	

	Page
and Shock Wave Speeds Generated due to impact.	54
Calculation of the Steady State Regime.	60
Attenuation of the Peak Pressure.	66
Consideration of Strength Effects	69
Tail of the Shock Wave.	78
Determination of the Attenuation Constants.	82
Strain Rates.	84
Discussion on Strain Rates.	85
VIII. PREDICTION OF CRATER DEPTHS	88
Derivation of Penetration Equation.	88
Determination of Dynamic Yield Strength	90
Prediction of Crater Depths	91
Discussion of Results	93
IX. SUMMARY AND CONCLUSIONS	97
REFERENCES	100
APPENDIX	
A. STRESS DEVIATOR	108
B. CALCULATION OF STRAIN RATES	112
VITA	135

LIST OF TABLES

	Page
Table 4.1 Verification of the Proposed Yield Criterion for 3 Dimensional Loading	23
Table 6.1 Initial Rockwell Hardness of Target Samples	45
Table 6.2 Constants in Constitutive Equation.	50
Table 6.3 Penetration Depths.	52
Table 7.1 Impact Hugoniot Values.	59
Table 7.2 Representative Values of Strain Rates Along the Axis of Symmetry.	86
Table 8.1. Theoretical and Experimental Crater Depths.	95

LIST OF FIGURES

	Page
Figure 4.1 Verification of the Proposed Yield Criterion for 2 Dimensional Loading.	21
Figure 5.1 Plot of $\ln(\exp F-1)$ - vs - $\ln(\dot{\epsilon}/\dot{\epsilon}_0)$ for Annealed Aluminum.	31
Figure 5.2 Functional Relationship of m and C with Respect to Strain for Annealed Aluminum, $\ln(\exp F-1) = m \ln(\dot{\epsilon}/\dot{\epsilon}_0) + C$	33
Figure 5.3 Experimental and Theoretical Rate Sensitivity for Annealed Aluminum (99.995% Pure) .	34
Figure 6.1 Quasi-Static and Dynamic Response of 1100 Aluminum.	40
Figure 6.2 Quasi-Static and Dynamic Response of Commercially Pure Lead	41
Figure 6.3 Quasi-Static and Dynamic Response of Mild Steel	42
Figure 6.4 Quasi-Static and Dynamic Response of 6061 Aluminum Alloy	43
Figure 6.5 Split Hopkinson Pressure Bar Apparatus	47
Figure 6.6 Hypervelocity Impact Test Configuration.	51
Figure 7.1a Schematic Diagram Showing the Axis of Symmetry . .	55

	Page
Figure 7.1b Configuration of Stresses in an Element Compressed by a Plane Shock Wave.	56
Figure 7.2 Graphical Impedance Matching.	58
Figure 7.3 Characteristic Diagram; $V_p < U_{spi}$	62
Figure 7.4 Characteristic Diagram; $V_p > U_{spi}$	63
Figure 7.5 Typical $U_s - U_p$ Shock Hugoniot.	75
Figure 7.6 Configuration of Characteristics for an Attenuating Shock Wave.	76
Figure 7.7 Pressure Profile of a Plane Shock Wave at Two Successive Time Intervals	79
Figure 7.8 Geometry to Determine the Tail of Shock	80
Figure 7.9 Generation of the Tail Behind the Shock Wave.	83
Figure 8.1 Determination of Dynamic Yield Strength.	92
Figure 8.2 Comparison of Theoretical and Experimental Crater Depths	94

NOMENCLATURE

Variable	
A	Area of cross section
A_1	Defined in equation (7.10)
A_3, B_3	Attenuation constants
a_1, b_1, c_1	Constants defined in equation (5.7)
a_2, b_2, c_2	Constants defined in equation (5.8)
B_t	Brinell Hardness of target
C	Function of strain given by equation (5.8)
c	Wave speed
c_r	Speed of rarefaction wave
d_1	Defined in equation (7.10b)
d_2	Defined in equation (7.10c)
d_p	Diameter of projectile
E	Young's Modulus of Elasticity
E_1	Internal energy
E_p	Kinetic energy of the projectile
e	Engineering Strain
F	Strain rate Sensitive function
f	Dynamic yield function
f_o	Quasi-static yield function
J_2'	Second invariant of the stress deviator
J_3'	Third invariant of the stress deviator
k	Defined in equation (7.10f)

K	Bulk Modulus
K_1	Defined in equation (7.10c)
K_2	Constant in the yield criterion
K_4, K_5, K_6	Constants in the penetration Equations
k_s	Slope of the pressure-compression isentrope.
L	Length
\bar{L}	Defined in equation (7.10d)
m	Function of Strain given by equation (5.7)
p	Pressure
P	Load
P_c	Penetration or Crater depth
S_t	Strength of target
t	Time
U_p	Particle velocity
U_s	Speed of shock wave
v	specific volume
v_c	volume of crater
V_p	Velocity of projectile
x, y, z	Rectangular Cartesian coordinates
Y_0	Quasi-static Yield Stress
Z	Distance along the axis of symmetry
Z_0	Defined in equation (7.10g)
β	Defined in equation (7.10a)
γ	Grüneisen ratio

Δ	Small increment or change
δ_{ij}	Kronecker delta
ϵ	Natural Strain
$\bar{\epsilon}$	Principal Strain
ϵ_{ij}	Strain rate tensor
ϵ_{ij}^E	Elastic component of strain rate tensor
ϵ_{ij}^P	Plastic component of strain rate tensor
ϵ'_{ij}	Deviatoric component of strain rate tensor
ϵ''_{ij}	Spherical component of strain rate tensor
ϵ_0	Quasi-static strain rate
μ	Modulus of rigidity
ρ	Density
σ_{ij}	Stress tensor
σ'_{ij}	Deviatoric stress tensor
σ''_{ij}	Spherical stress tensor
$\bar{\sigma}$	Principal stress
σ_0	Quasi-static stress
$\sigma_{\text{dyn-yd}}$	Dynamic Yield Strength
τ	Shearing stress
τ_{oct}	Octahedral shearing stress
τ_{max}	Maximum shearing stress

Subscripts

e	nominal; engineering
H	Hugoniot
i	initial
I	Incident
ij	Second order tensor
o	Quasi-static; undisturbed
p	projectile
R	reflected
s	Shock
S	isentropic; specimen
t	target
T	transmitted

Superscripts

.	differentiation with respect to time
—	Principal value
'	Deviatoric
"	Spherical
E	Elastic
P	Plastic

CHAPTER I

INTRODUCTION

There is considerable interest in, and concern over, the problems of hypervelocity impact, especially in relation to meteoroid hazard to spacecraft. The study of damage that would be inflicted by meteoroid impact requires the simulation of these impacts in the laboratory. Meteoroid shapes vary from highly irregular to nearly spherical. Estimates of the density of meteoroids have ranged from 0.05 to 8 gm/cm³. The expected range of velocities for meteoroids is generally agreed to be from 11 to 72 km/sec, relative to earth. The lower limit corresponds to the velocity that would be attained by a particle when started from rest relative to earth and the upper limit is the maximum relative velocity of collision between earth and a body in the solar system. The speeds of the majority of meteoroids will be in the range of 15 to 28 km/sec. Although laboratory simulation techniques are presently available to only about 21 km/sec; it is believed that these techniques provide true hypervelocity impact, and that the cratering phenomenon observed is the same as that which occurs at higher velocities.

A hypervelocity impact may be defined in the following ways:

- (a) It is defined as the impact in which the initial velocity exceeds that necessary to produce steady-state (i.e., Bernoulli)

The citations on the following pages follow the style of Transactions of the ASME Journal of Applied Mechanics.

pressures greater by at least an order of magnitude than the yield strengths of both the target and the projectile materials; (b) more commonly it is defined as the impact with a velocity which exceeds the sound velocity of the target; (c) sometimes, it is also defined as the impact in which the velocity of the projectile-target interface exceeds the sound velocity of the latter.

During the impact process each element of the projectile and target is first shocked to some pressure, and is then brought back to ambient pressure by rarefaction waves. The initial shocking process is nonisentropic, whereas the release process is isentropic. Thus the entropy of the material has been increased by the impact process, which means the material in its final state will be heated. Shocks of low strength will leave the material heated but in the solid state. As the shock strength is increased, entropy increases rapidly, leading to melting, heating of liquid, vaporization, or superheating of vapor in the final state.

During the initial stages of crater formation, hydrodynamic theory is applicable but during the later stages when the shock pressure decays to magnitudes comparable to the material strength the strength effects have to be considered.

Thus current interest in hypervelocity impact is due largely to the need for information concerning the meteoroid damage to space vehicles. Associated with this problem is the dynamic mechanical response of the materials under extremely high pressure resulting

from hypervelocity impact. A collision or impact with one of the hypervelocity projectiles creates a crater in the target and drives a strong shock wave resulting in considerable plastic deformation in the vicinity of the crater. Depending upon the thickness and orientation of the target as well as the velocity of impact, the damage caused to the target may be a complete perforation, a crater at the impacting end accompanied by spallation at the rear end due to reflected tensile waves, or simply a crater in the case of semi-infinite targets.

Thus the hypervelocity impact problem is associated with a number of complexities. But continued effort is being made by researchers to advance the existing state of knowledge by developing new kinds of experimental facilities to generate higher velocities and to simulate the meteoroid phenomena; and by developing computational facilities and measuring devices to precisely determine the transient phenomena.

CHAPTER II

LITERATURE REVIEW

The high velocity impact was analyzed in terms of four phases; namely, transient, primary, secondary, and recovery phases by Christman et al. [1]. They concluded from their study that only the primary and secondary phases make a significant contribution to the final crater size. Kineki [2] considered the crater formation process in terms of four regimes; namely, transient, steady-state, cavitation, and recovery regimes to analyze crater formation in ductile materials under hypervelocity impact. It has been postulated that in the final stages the compressed shell of material under the crater will undergo recovery resulting in slight diminishing of the crater dimensions. Pond et al. [3] studied the recrystallization of an affected region surrounding the actual crater and reported that the ratio of affected area to actual crater volume increases with increasing energy of the impacting projectile. Rae et al. [4] applied blast wave theory to crater formation studies of semi-infinite targets assuming similarity of flow, global energy and momentum conservation, and the Mie-Grüneisen equation of state. A study of crater formation in solids by impact of ultra-high speed particles was made by Davids et al. [5,6] from the standpoint of radially symmetric advancing shock fronts. Their solution of equations of motion based on progressing waves led to a $2/5$ - power law for penetration - vs. - velocity. The expansion of spherical cavities

in impulsively loaded thick metal spheres was investigated analytically and experimentally for a linear strain-hardening material by Davids et al. [7]. Hwang et al. [8] proposed a graphical method which reduced the complexity of solving wave propagation problem of nonlinear materials. They considered nonlinearities arising out of σ - ϵ relationships, unloading situations, and brittleness of the materials. Kinslow [9] by the use of the digital computer found the characteristics of the forcing functions which will produce the same effects as those caused by hypervelocity projectiles. This permitted the computation of particle velocity, displacement, and principal stresses within the target. Eichelberger et al. [10] studied penetration into semi-infinite targets and perforation of thin sheets and described the fundamental characteristics of crater formation and meteoroid damage to space vehicles in hypervelocity impact. Gehring et al. [11] used the throw-off pellet method to measure maximum shock pressure. They also measured successfully the momentum transferred to semi-infinite aluminum targets in hypervelocity impact and observed three distinct stages of the crater growth process. They also showed that during the hydrodynamic regime the solid state strength effects are unimportant. Bjork [12] analyzed the temperatures produced for four metals as a function of shock pressure. In view of the creation of entropy in the shock front, the target material will be left heated even after expanding back to zero pressure. Based purely on hydrodynamic flow,

he predicted the melted region in the target. Marnell et al. [13] proposed a series solution for the hypervelocity impact problem. Luttrell [14] developed a mathematical method to predict the depth and duration of penetration into thick ductile targets by compact deforming projectiles. Wagner et al. [15] considered impact of a porous aluminum projectile on an aluminum target at 20 and 72 km/sec. The regions of the target melted by the impact were delineated. A more accurate equation of state for aluminum was formulated using the data generated by Russian scientists. Hugoniot, release adiabats and temperatures resulting from shock compression and expansion were calculated. Heyda et al. [16] developed an analytical method based on planar blast wave theory to determine accurately the peak axial pressures generated in semi-infinite targets under hypervelocity impact using the Los Alamos equation of state.

The effects such as electrical, optical, mechanical, and metallurgical were studied by Rice et al. [17] during the compression of solids by strong shock waves. Walsh et al. [18,19] and Doran et al. [20] used an explosive system to drive a strong wave up to 500 kilobars pressure into metal specimens and measured shock and free surface velocities by a photographic technique. The measured velocity pairs were transformed into pressure compression points using the conservation equations. Resulting $p - v_s - \frac{v}{v_0}$ curves were given for twenty-seven metals. The experimental curves, which consist thermodynamically of a known p, v, E_1 locus for each

material and a theoretically estimated Grüneisen ratio, γ , were used to calculate a more complete high pressure equation of state. McQueen et al. [21] determined equations of state for nineteen metals from shock wave measurements up to pressures of two megabars. Al'tshuler et al. [22, 23, 24] determined dynamic compressibility of metals under pressures up to four mega-atmospheres using the Dugdale-MacDonald relation to obtain the Mie-Grüneisen ratio.

Lindholm [25] studied experimentally the deformation of aluminum at strain rates from 10^{-3} sec^{-1} to 10^3 sec^{-1} and temperatures from 300°K to 700°K under a range of stress states including tension, compression, torsion, and combined tension and torsion. Boa-Teh [26] studied response of various material media to high velocity loading. Chiu et al. [27] developed a difference method for wave analysis of the split Hopkinson pressure bar with a visco-elastic specimen. Nevill et al. [28] studied strain rate effects during reversed loading considering the Bauschinger effect. A penetration method for determining impact yield strength was suggested by Davids et al. [29]. Rolsten et al. [30] suggested three different methods; namely, measurement of true tensile strength measurement of hemispherical crater dimensions from a hypervelocity impact with projectiles of known mass and striking velocity, and the measurement of the Hugoniot yield. They emphasized that the initial phases of the motion resulting from a high velocity impact may be adequately described by hydrodynamic principles but the stresses rapidly decay due to geometrical divergence and dissipation to the

point where material strength effects become important. Chou et al. [31] studied the attenuation of a strong plane shock produced in a target by the impact of a thin striker using the numerical method of characteristics. Their results showed that late stage equivalence exists for impacts in aluminum, copper, and ideal gases with various ratios of specific heats. Riney [32] applied a viscoplastic method to hypervelocity impact and showed that strength and strain rate effects predominate during the later stages. Energy scaling for geometrically similar impact situations was predicted. Dunn [33] showed that there exists one well defined material constant, the dynamic yield strength $\sigma_{yD} = \mu/15$ where μ is shear modulus, which can be used in hypervelocity impact calculations. Piacesi et al. [34] have shown through a temperature-mechanical strength correlation that the tensile and compressive yield strengths are effective mechanical strength properties and that the ultimate tensile strength and microhardness are not effective strength properties in determining the final crater dimensions.

Bjork [35] used a purely hydrodynamic approach to study the cratering process that accompanied the impact of a 12,000 ton iron projectile on a semi-infinite half space of soft rock at 30 km/sec. Olshaker et al. [36], and Walsh et al. [37] used hydrodynamic theory and suggested that final damage due to hypervelocity impact can be calculated by a combination of experimental and theoretical results. Rinehart et al. [38] studied the craters produced in plaster of paris targets by steel pellets at 2.5 km/sec. at different angles

of incidence. Wilkins [39], and Wilkins et al. [40] applied hydrodynamic-elastic-plastic approach for the solution of hypervelocity impact problems. Riney [41,42], MacCormack [43], and Kraus [44] studied hypervelocity impact cratering phenomena from the standpoint of hydrodynamic-elastic-viscoplastic considerations. Chou [45] applied viscoplastic flow theory for perforation of plates in hypervelocity impact. Wenzel et al. [46] performed hypervelocity impact studies up to 16.5 km/sec. and their experimental results supported the penetration equation which contains the maximum Brinell hardness of the target as a parameter. They also listed various penetration equations obtained by theoretical and empirical approaches.

Published experimental data on cratering by hypervelocity projectiles in quasi-infinite metallic targets comprising over 1700 data points generated at 15 laboratories were collected and analyzed statistically by Herrmann et al. [47] to obtain empirically fitted expressions for crater depth and volume. They used the static hardness of the target as a parameter in their empirical penetration equation. Engel [48] proposed a crater depth model for the regime of partial fluidity in hypervelocity cratering based on his experiments with copper and aluminum targets. Bruce [49] reviewed various types of penetration and crater volume equations of hypervelocity impact on semi-infinite targets. Sawle [50] studied the effect of material strength in thin sheet perforation and penetration into semi-infinite targets at 15 km/sec. and fitted

empirical equations.

Dynamic behavior of metals was studied by Prager [51], Bodner [52], Davies et al. [53], and Lindholm [54]. Butcher et al. [55], and Marsh et al. [56] investigated the influence of strain rate on work-hardening behavior of steels. Malvern [57] made experimental studies of strain rate effects and plastic wave propagation in annealed aluminum and his results fitted well either with a logarithmic dependence for dynamic over-stress and strain rate or with a power law. Wood et al. [58], and Ripperger [59] studied the dynamic plastic behavior of metals and the constitutive equation fitting their data with that proposed by Malvern. A phenomenological constitutive equation applicable to structural materials at ambient temperatures was proposed by McLellan [60]. Willis [61] derived general thermodynamic constitutive equations applicable to problems of large plastic flow of an elastic-plastic body. Generalizations of the one dimensional constitutive equations for rate sensitive plastic materials were made by Perzyna [62]. He also considered the dynamic yield conditions for elastic-viscoplastic materials. Cristescu [63] summarized and presented a list of semi-linear and quasi-linear differential constitutive equations used in dynamic plasticity. Rosenblatt [64] used rate sensitive three dimensional hydrodynamic-elastic-viscoplastic constitutive relations proposed by Perzyna to predict the penetration depths and ballistic limits in hypervelocity impact. He also studied non-linear size scaling

effects and obtained good agreement with the limited amount of available experimental data.

Pond et al. [3], and Mobley et al. [65] considered the energy balances in hypervelocity impact and indicated that the kinetic energy of the projectile is used for the disintegration of the projectile, crater lip formation, crater formation, development of a high shear strain volume, and development of low shear strain in the rest of the target. Palmer et al. [66] from their impact experiments of steel balls into lead targets reported energy partitioning. They considered the division of energy among target heating, energy of ejected material, and strain and recrystallization. Partitioning changes rapidly with velocity at low velocities, and then only slowly at velocities near 3.4 km/sec. Jean et al. [67] demonstrated that the short duration transient spike observed in hypervelocity impact can be attributed to the presence of a hot, dense plasma at the impact point whereas the slow rising, long duration tail was due to the radiation of a neutral gas expanding from the impact zone.

Davids [68] made a transient analysis of oblique impact on plates and found that the ratio of crater volume to projectile energy was proportional to the cosine of the angle of incidence. Kreyenhagen et al. [69] determined the ballistic limits in impacts on multimaterial laminated targets. McMillan [70], and Nysmith et al. [71] studied the penetration of hypervelocity projectiles into composite laminates.

CHAPTER III

OBJECTIVES

Extensive research has been carried out to analyze and predict the target damage in hypervelocity impact, but information is rather scarce, inconclusive and sometimes conflicting regarding the target strength influence and strain rate effects. This is apparent from the fact that in predicting the penetration depths, some of the penetration equations, such as the first Apollo equations used only static strength or hardness of target, whereas other penetration equations, such as the Manned Spacecraft Center equation and the General Motors equation, use strength or hardness of target measured after impact. Hence in order to study the strength and rate effects in hypervelocity impact, the development of an adequate yield criterion and an appropriate strain rate sensitive constitutive equation are felt to be essential. Therefore the aim of the present dissertation is to study the above effects with the following objectives:

1. To obtain a yield criterion involving, besides the second invariant, J_2' , the third invariant, J_3' , of the deviatoric stress tensor. Appendix A shows the stress deviator and its invariants for the most general case.

2. To develop a strain rate sensitive constitutive equation, i.e. a relation between stress, strain, and strain rate using the

above yield criterion.

3. To determine the strain rates encountered in hypervelocity impact considering the shock wave propagation in the inviscid hydrodynamic and elastic-plastic regimes.

4. To predict the crater or penetration depths using the General Motors penetration equation and the above constitutive equation. The dynamic strength will be used instead of dynamic hardness but it will be related to static strength based on the strain rates determined from the hydrodynamic, elastic-plastic considerations and the constitutive equation.

To achieve the first objective; the results of experiments, performed by various researchers for testing the applicability of the von Mises criterion for two-dimensional and three-dimensional loading situations, will be used. Based on these results, the accuracy of the proposed yield criterion which consists of J_2' , and J_3' will be evaluated.

To accomplish the second objective of developing a constitutive equation, the dynamic experimental data available in the literature for different materials will be utilized to find a relationship among the variables of stress, strain, and strain rate and certain material constants. After establishing the relationship, quasi-static, and dynamic experiments will be performed on 1100 Aluminum, 6061 Aluminum alloy, commercially pure lead, and 1018 Mild Steel to generate the constants involved in the above constitutive equation.

The idea underlying this formulation is to be able to determine the strength associated with any particular strain rate or simply the dynamic strength of the material under study.

The determination of strain rates encountered in hypervelocity impact of a projectile on a semi-infinite target will be achieved by determining the particle velocities along the axis of symmetry of the target based on the attenuation of peak pressure associated with the impact, as the shock wave propagates through the target, considering the rarefaction and the strength effects. Even though the hydrodynamic conditions prevail during the initial stages, the strength effects are important and hence will be considered during the later stages.

The ultimate objective of predicting the crater or penetration depths that result from the impact of a projectile on a semi-infinite target will be achieved by the use of the General Motors penetration equation. Instead of the hardness of the target measured after impact, a dynamic strength term will be adapted into the above equation. The dynamic strength in turn will be obtained from the constitutive equation knowing the equivalent static value and the strain rate. The idea underlying this step is to be able to predetermine the actual penetration that results from a given set of impact conditions without actually damaging the target.

CHAPTER IV

YIELD CRITERION

The state of stress on a body has a profound influence on the determination of the extent of deformation that may be achieved. From the crystallographic studies and dislocation considerations, the basic mechanisms that contribute to plastic deformation were established to be translational gliding and twin gliding which in turn produce shear. Therefore the basic phenomenon underlying plastic deformation is the existence of shearing stresses on any arbitrarily chosen plane. Thus a state of equal triaxial tension or compression will not produce plastic deformation, no matter how high the stresses may be.

The basis for the determination of the initiation of plastic flow under a general state of stress may be defined as the yield criterion. The von Mises yield criterion, which considers only the second invariant of the deviatoric stress tensor, is the most widely used criterion because of its simplicity and accuracy as evidenced by experimental results. A deviatoric stress tensor may be defined as a tensor whose normal components differ from those of the total stress tensor by a hydrostatic component, whereas the shear components correspond exactly to those of the total stress tensor. The stress deviator and its invariants for the general case are developed in Appendix A.

According to von Mises criterion any material under any

kind of loading initiates yielding when the second invariant, J_2' , of the deviatoric stress tensor reaches a critical value. The critical value is most simply determined as the value of J_2' at yield under a uniaxial state of stress. Mathematically this can be expressed as follows:

$$J_2' = J_2' \text{ corresponding to yield in uniaxial loading} \quad (4.1a)$$

$$\text{von Mises criterion is; } J_2' = \frac{Y_0^2}{3} \quad (4.1b)$$

where Y_0 is yield stress in the uniaxial case.

For uniaxial loading, the various stress tensors can be related as follows:

$$\begin{matrix} \text{(Total Stress)} \\ \text{Tensor} \end{matrix} = \begin{matrix} \text{(Deviatoric Stress)} \\ \text{Tensor} \end{matrix} + \begin{matrix} \text{(Hydrostatic or)} \\ \text{Spherical Stress Tensor} \end{matrix} \quad (4.2a)$$

$$\begin{bmatrix} \sigma_{11} & 0 & 0 \\ 0 & 0 & 0 \\ 0 & 0 & 0 \end{bmatrix} = \begin{bmatrix} \frac{2\sigma_{11}}{3} & 0 & 0 \\ 0 & -\frac{\sigma_{11}}{3} & 0 \\ 0 & 0 & -\frac{\sigma_{11}}{3} \end{bmatrix} + \begin{bmatrix} \frac{\sigma_{11}}{3} & 0 & 0 \\ 0 & \frac{\sigma_{11}}{3} & 0 \\ 0 & 0 & \frac{\sigma_{11}}{3} \end{bmatrix}$$

Thus the total deformation of an elemental cube may be expressed as the sum of the change in shape or distortion and the change in volume. The change in shape is due to the deviatoric tensor and the change of volume is due to the hydrostatic tensor. Plastic deformation is associated almost entirely with changes in shape and is considered to be independent of changes in volume. The Hydrostatic tensor does not involve shear terms irrespective of the orientation of the reference axes whereas the deviatoric tensor contains shear

terms depending on the orientation. The change in shape and plastic deformation are thus associated with the presence of shear stresses. Therefore, as far as the yielding and plastic deformation of materials are concerned, the hydrostatic or spherical stress tensor has no influence, and hence the above are totally attributable to the deviatoric stress tensor. Every stress tensor has three invariants associated with it. But in the case of a deviatoric stress tensor, the first invariant, J'_1 , is identically zero for any loading and hence has only two nonvanishing invariants. For the uniaxial case;

$$J'_1 = \sigma'_{ii} = 0 \quad (\text{For any loading including uniaxial case}) \quad (4.3)$$

$$J'_2 = \frac{1}{2} \sigma'_{ij} \sigma'_{ij} = \frac{\sigma_{11}^2}{3} \quad (4.4a)$$

$$J'_2 \text{ yield} = \frac{Y_o^2}{3} \quad (4.4b)$$

$$J'_3 = \frac{1}{3} \sigma'_{ij} \sigma'_{jk} \sigma'_{ki} = \frac{2}{27} \sigma_{11}^3 \quad (4.5a)$$

$$J'_3 \text{ yield} = \frac{2}{27} Y_o^3 \quad (4.5b)$$

Most of the researchers such as Thomsen et al. [72] feel that the third invariant of the deviatoric tensor has some influence on the yielding of metals. Hence it is thought that the slight deviation of the experimental results obtained by researchers to verify the von Mises criterion, might be due to the influence of the third invariant of the deviatoric stress tensor. Anticipating that incorporation of the third invariant, J'_3 , into the yield

criterion of metals might give better results, the following type of relation was proposed. If the influence of the Bauschinger effect is ignored, it can be assumed that metals behave similarly in tension and compression. This points out that only even powers of stresses need be considered. Therefore a 2/3rd power is used for the third invariant as follows:

$$J_2' + K_2 (J_3')^{2/3} = \frac{Y_0^2}{3} + K_2 \left(\frac{2}{27} Y_0^3 \right)^{2/3} \quad (4.6)$$

To determine K_2 , the classical experimental results of Taylor et al. [73] on aluminum and copper tubes were used. Since they used thin walled tubes subjected to torque and axial load, the various stress tensors can be expressed as:

$$\begin{bmatrix} \sigma_{xx} & \tau_{xy} & 0 \\ \tau_{yx} & 0 & 0 \\ 0 & 0 & 0 \end{bmatrix} = \begin{bmatrix} \frac{2}{3}\sigma_{xx} & \tau_{xy} & 0 \\ \tau_{yx} & -\frac{\sigma_{xx}}{3} & 0 \\ 0 & 0 & -\frac{\sigma_{xx}}{3} \end{bmatrix} + \begin{bmatrix} \frac{\sigma_{xx}}{3} & 0 & 0 \\ 0 & \frac{\sigma_{xx}}{3} & 0 \\ 0 & 0 & \frac{\sigma_{xx}}{3} \end{bmatrix} \quad (4.7)$$

The deviatoric stress invariants are;

$$\begin{aligned} J_1' &= 0 \\ J_2' &= \frac{\sigma_{xx}^2}{3} + \tau_{xy}^2 \\ J_3' &= \frac{2}{27} \sigma_{xx}^3 + \frac{1}{3} \sigma_{xx} \tau_{xy}^2 \end{aligned}$$

When these are substituted into equation (4.6), K_2 is given by

$$K_2 = \frac{1 - \left(\frac{\sigma_{xx}}{Y_0}\right)^2 - 3 \left(\frac{\tau_{xy}}{Y_0}\right)^2}{\left[3 \left\{ \frac{2}{27} \left(\frac{\sigma_{xx}}{Y_0}\right)^3 + \frac{1}{3} \left(\frac{\sigma_{xx}}{Y_0}\right) \left(\frac{\tau_{xy}}{Y_0}\right)^2 \right\}^{2/3} - \frac{1}{3} (2)^{2/3}\right]} \quad (4.8a)$$

The determination of K_2 involved the solution of the following equation (4.8b).

$$\begin{aligned} & 27 \left(\frac{\tau_{xy}}{Y_0}\right)^6 + \left(\frac{\tau_{xy}}{Y_0}\right)^4 \left\{ 27 \left(\frac{\sigma_{xx}}{Y_0}\right)^2 + 3 K_2^3 \left(\frac{\sigma_{xx}}{Y_0}\right)^2 - 27 \left(1 + \frac{4}{3} K_2\right) \right\} \\ & + \left(\frac{\tau_{xy}}{Y_0}\right)^2 \left\{ \left(9 + \frac{4}{3} K_2^3\right) \left(\frac{\sigma_{xx}}{Y_0}\right)^4 - 18 \left(1 + \frac{4}{3} K_2\right) \left(\frac{\sigma_{xx}}{Y_0}\right)^2 + 9 \left(1 + \frac{4}{3} K_2\right) \right\} \\ & + \left(\frac{\sigma_{xx}}{Y_0}\right)^6 \left(1 + 4 K_2^3\right) - 3 \left(\frac{\sigma_{xx}}{Y_0}\right)^4 \left(1 + \frac{4}{3} K_2\right) + 3 \left(\frac{\sigma_{xx}}{Y_0}\right)^2 \left(1 + \frac{4}{3} K_2\right) \\ & - \left(1 + \frac{4}{3} K_2\right) = 0. \end{aligned} \quad (4.8b)$$

This sixth degree polynomial in $\frac{\tau_{xy}}{Y_0}$ is solved using a computer for known values of $\frac{\sigma_{xx}}{Y_0}$ and different values of K_2 . The values

of $\frac{\tau_{xy}}{Y_0}$ solved from equation (4.8b) compared favorably with the

experimental results when K_2 was -0.13.

∴ The yield criterion can be expressed as;

$$J_2' - 0.13 (J_3')^{2/3} = \frac{Y_0^2}{3} - 0.13 \left(\frac{2Y_0^3}{27} \right)^{2/3} \quad (4.9)$$

This yield criterion was compared with two-dimensional results of Naghdi et al. [74] on 24S-T-4 aluminum alloy and three-dimensional results of Osgood on 24S-T aluminum alloy [75]. The formulation of J_2' and J_3' still holds for the experiments of Naghdi et al. as they also used similar kinds of loadings as Taylor et al. Figure 4.1 shows the experimental results of Taylor et al. and Naghdi et al. and the von Mises criterion ($K_2=0$) and the present yield criterion with $K_2 = -0.13$. It may be noted that the experimental results are close to equation (4.9).

Osgood subjected 24S-T Aluminum alloy tubes to internal pressure and axial load which thus produced σ_r , σ_t , and σ_a the radial, hoop, and axial stresses respectively. He presented his results in the form of octahedral and maximum shearing stresses. The various stress tensors can be written as follows:

$$\begin{bmatrix} \sigma_t & 0 & 0 \\ 0 & \sigma_a & 0 \\ 0 & 0 & \sigma_r \end{bmatrix} = \begin{bmatrix} \frac{2\sigma_t - \sigma_a - \sigma_r}{3} & 0 & 0 \\ 0 & \frac{2\sigma_a - \sigma_t - \sigma_r}{3} & 0 \\ 0 & 0 & \frac{2\sigma_r - \sigma_t - \sigma_a}{3} \end{bmatrix} + \begin{bmatrix} \frac{\sigma_t + \sigma_a + \sigma_r}{3} & 0 & 0 \\ 0 & \frac{\sigma_t + \sigma_a + \sigma_r}{3} & 0 \\ 0 & 0 & \frac{\sigma_t + \sigma_a + \sigma_r}{3} \end{bmatrix} \quad (4.10)$$

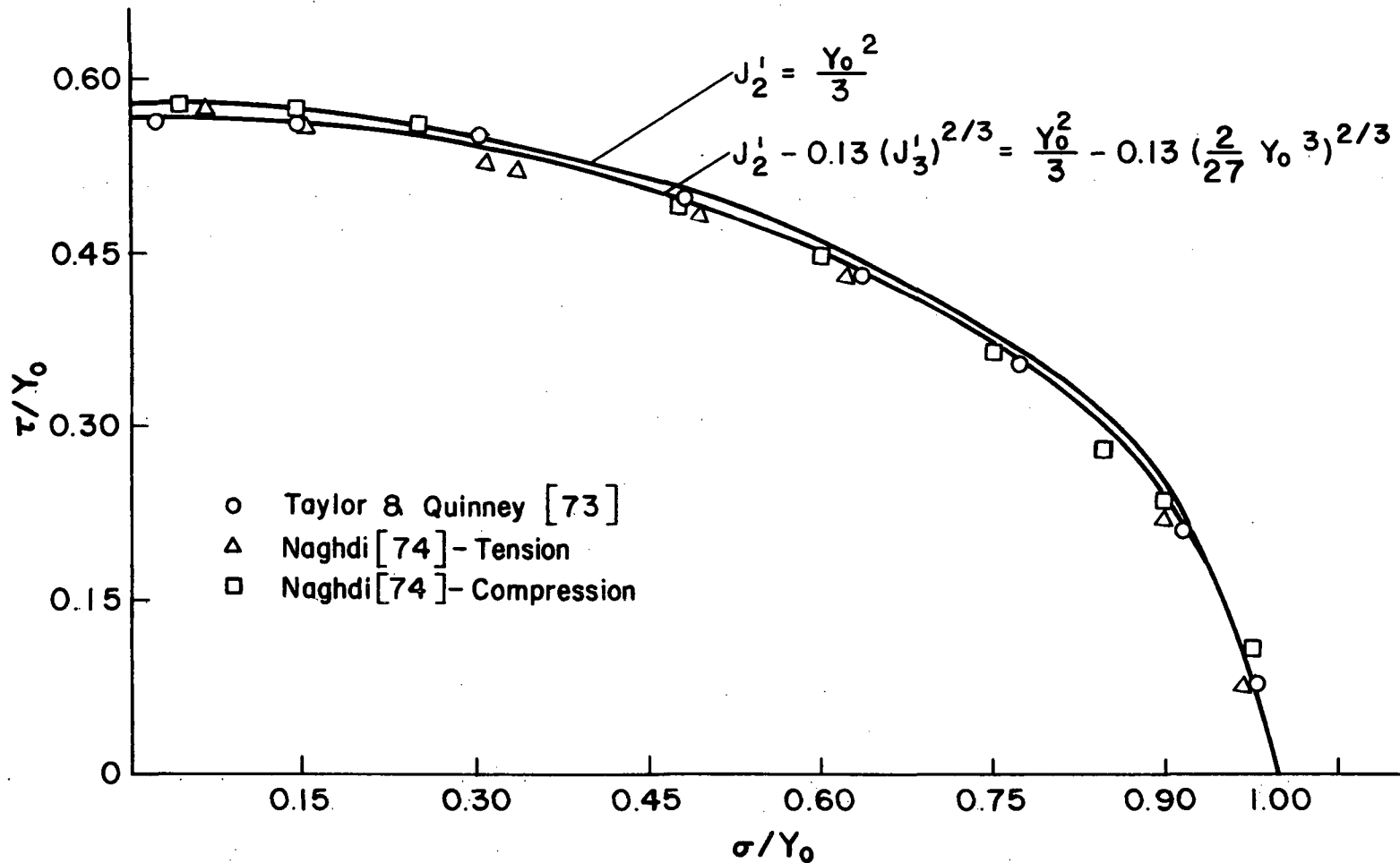


Fig. 4-1. Verification of the Proposed Yield Criterion for 2 Dimensional Loading

$$J_2' = \frac{1}{2} \left\{ \left(\frac{2\sigma_t - \sigma_a - \sigma_r}{3} \right)^2 + \left(\frac{2\sigma_a - \sigma_t - \sigma_r}{3} \right)^2 + \left(\frac{2\sigma_r - \sigma_t - \sigma_a}{3} \right)^2 \right\}$$

$$J_2' = \frac{1}{6} \{ (\sigma_t - \sigma_a)^2 + (\sigma_a - \sigma_r)^2 + (\sigma_r - \sigma_t)^2 \}$$

$$\tau_{oct}' = \frac{1}{9} \{ (\sigma_t - \sigma_a)^2 + (\sigma_a - \sigma_r)^2 + (\sigma_r - \sigma_t)^2 \}$$

$$J_2' = \frac{3}{2} \tau_{oct}'^2 \quad (4.11)$$

$$J_3' = \frac{1}{27} (2\sigma_t - \sigma_a - \sigma_r) (2\sigma_a - \sigma_r - \sigma_t) (2\sigma_r - \sigma_a - \sigma_t) \quad (4.12)$$

The experimental results of Osgood were presented by Drucker [76] on a magnified scale and the values of τ_{oct} and τ_{max} at the

yield point were taken for different combinations of the ratio

$$r = \frac{\sigma_t}{\sigma_a}$$

$$\tau_{max} = \frac{\sigma_t - \sigma_r}{2}, \text{ or } \frac{\sigma_a - \sigma_r}{2} \quad (4.13)$$

depending on whether r is greater or less than unity.

Knowing τ_{max} and τ_{oct} at the yield point and r , the values of σ_t , σ_a and σ_r can be found and hence J_2' and J_3' can be computed using equations (4.11) and (4.12). These values were substituted into the yield criterion as given by equation (4.9) and the results are presented in Table 4.1. The results in column 9 are due to equation (4.9) and those in column 7 correspond to the von Mises criterion. It can be seen that the von Mises criterion predicts a constant value of $J_2' 469.935 \times 10^6 \frac{\text{lb}^2}{\text{in}^4}$ at yield for this material whereas

Table 4.1 Verification of the Proposed Yield Criterion for 3 Dimensional Loading.

r	$\tau_{\text{oct-yield}}$	$\tau_{\text{max-yield}}$ psi	σ_t	σ_a	σ_r	$J_2' \times 10^{-6}$ (psi) ²	% deviation from von-Mises criterion	$[J_2' - 0.13(J_3')^{2/3}] \times 10^{-6}$ (psi) ²	% deviation from the proposed criterion
0	17,700	18,750	0	37,500	0	469.935	0	437.691	0
0.5	17,380	21,000	14,980	29,960	-12,040	453.097	3.59	434.192	0.80
1.0	17,800	18,900	.	.	.	475.200	1.12	442.115	1.01
2.0	17,200	21,050	39,313	19,656	- 2,787	443.760	5.57	436.642	0.24
∞	17,500	17,250	33,500	0	- 1,000	459.375	2.25	432.912	1.09

the present criterion predicts $437.691 \times 10^6 \frac{\text{lb}^2}{\text{in}^4}$ at yield. The results in column 9 of Table 4.1 are closer to 437.691×10^6 . The percentage deviations as referred to a uniaxial state of stress for both the yield criteria, i.e. $K_2 = 0$ and $K_2 = -0.13$ are also presented in Table 4.1.

From Figure 4.1, it can be noted that the proposed criterion with $K_2 = -0.13$ lies below von Mises criterion with $K_2 = 0$. It can also be observed that the effect of J_3' is more pronounced with loading combinations of larger shear stress and smaller normal stresses.

Even though the proposed criterion does not differ very much from the von Mises criterion for the loading situations considered, further investigation, as a search for combinations of loadings where the effect of J_3' is much more pronounced, is needed. Thus yielding, being considered as the initiation of plastic deformation and hence influenced solely by the stress deviator, may be described by the nonvanishing invariants, namely J_2' and J_3' , of the stress deviator. Hence equation (4.9) which takes into account J_2' and J_3' may be considered as an adequate yield criterion based on two-dimensional and even three-dimensional experimental data for the materials considered.

CHAPTER V

STRAIN RATE SENSITIVE CONSTITUTIVE EQUATION

For the solution of practical problems, a constitutive equation, which characterizes the particular mechanical properties of the continuum under study, is imperative. The concept of a continuum may be explained as follows. Even though the molecular nature of the structure of matter and the presence of dislocations are well established rather qualitatively, in numerous practical and quantitative investigations of material behavior, the individual molecule is of no concern, and only the behavior of the material as a whole is deemed important. Thus the observed macroscopic behavior is usually explained by disregarding molecular considerations and, by assuming instead the matter to be continuously distributed throughout its volume and to completely fill the space it occupies. The constitutive equation, through which the role of the material and its properties come into the picture, is probably the weakest link in the continuum theories. This is due to the inability to describe adequately the entire regime of the material behavior.

To understand the mechanical response of the structural material under study and to be able to make a reasonably precise estimate of the behavior of the material at strain rates presently inaccessible for laboratory testing, a constitutive equation developed from theoretical and experimental considerations is

necessary. Currently no experimental apparatus is available to obtain dynamic properties of materials beyond strain rates of the order of 10^4 sec.^{-1} . Associated with the dynamic nature of the hypervelocity impact problem, the underlying need for a constitutive equation of the rate sensitive type is apparent.

Attempts to derive stress-strain relations made by Hencky, Prandtl and Reuss, Levy and Mises, and others were reported by Johnson et al. [77]. Hencky's equations are seemingly an attempt to extend the total strain theory of elasticity to plasticity. They state that the components of the total plastic strain are instantaneously proportional to deviatoric stress components. But it appears that only over the past two decades has it become generally recognized that plasticity problems are incremental or rate type in nature. Prandtl-Reuss equations treat components of plastic strain increments to be proportional to stress deviator components. Levy-Mises equations are a special case of the Prandtl-Reuss equations and treat components of total strain increment to be proportional to components of the stress deviator and hence are applicable to cases where elastic strains are negligible as compared to plastic strains. Thus, once again, the importance of the rate or incremental nature of the problems may be realized, and this coupled with the dynamic nature of the hypervelocity impact problems points out the necessity for developing a strain rate sensitive constitutive equation.

Several researchers like Malvern [78], Lindholm [25], and Perzyna [62] directed their efforts to obtain a generalized constitutive equation. The difficulties encountered in such an attempt are due to uncertainties and disparities involved in obtaining the dynamic material properties. Rand et al. [79] have analyzed the various types of approximations involved in obtaining split Hopkinson pressure bar data. He also developed a code based on the method of characteristics to analyze the results. The split Hopkinson bar is a widely used experimental technique to obtain dynamic stress-strain curves. The device uses strain gages mounted on elastic incident and transmitter bars. Results are based on the study of one-dimensional wave propagation. Bell [80] used a diffraction grating technique to determine the strains of the specimen associated with the split Hopkinson pressure bar apparatus. A large difference in strain was observed between the direct measurement and that inferred from pressure bar measurements. Subsequently it was reported that the radical departure of the diffraction grating measurement at approximately 4% strain was due to an experimental difficulty resulting from a change in reflectivity of the surface of the specimen.

The following formulation is essentially governed by the generalized hydrodynamic, elastic-viscoplastic approach of Perzyna [62]. The various strain rate tensors may be expressed as follows:

$$\dot{\epsilon}_{ij} = \dot{\epsilon}_{ij}^E + \dot{\epsilon}_{ij}^P \quad (5.1)$$

$$\dot{\epsilon}_{ij}^E = \dot{\epsilon}_{ij}^{E'} + \dot{\epsilon}_{ij}^{E''}$$

$$\dot{\epsilon}_{ij}^P = \dot{\epsilon}_{ij}^{P'} + \dot{\epsilon}_{ij}^{P''}$$

$$\dot{\epsilon}_{ij}^{E'} = \frac{1}{2\mu} \dot{\sigma}_{ij}'$$

$$\dot{\epsilon}_{ij}^{E''} = \frac{1}{3K} \dot{\sigma}_{ij}''$$

$$\dot{\epsilon}_{ij}^{P''} = 0 \quad (\because \text{i.e. no volume change in plastic deformation})$$

$$\dot{\epsilon}_{ij}^{P'} = \dot{\epsilon}_{ij}^P \quad (5.2)$$

where a dot denotes total differentiation with respect to time. Lower superscripts E and P denote the elastic and the plastic portions whereas the upper superscripts ', and '' denote the deviatoric and the hydrodynamic parts. Subscript ij refers to a second order tensor; σ and ϵ respectively denote stress and strain; μ , and K denote modulus of rigidity and bulk modulus respectively.

Empirical, semi-empirical, and theoretical approaches have been made by several researchers, such as Malvern [78], and Lindholm [25] to relate the plastic strain rate to stress and strain, with only partial success. For example, Rosenblatt had to use an exponential relation between the ratio of dynamic over-stress to static stress, and strain rate for some strain rates and a linear relation between

the same variables for higher strain rates in order to describe the hypervelocity impact process. Thus a constitutive equation, which is good for the entire regime of strain rates, is not available. In order to obtain a constitutive equation which will be good at least for the majority of strain rates, the following attempt has been made.

Defining a strain rate sensitive parameter, F as:

$$F = \frac{f(J_2', J_3')}{f_0(J_2', J_3')} - 1 \quad (5.3)$$

where f is a function similar to the yield criterion, consisting of the second, and third invariants of the stress deviator under dynamic conditions and f_0 is the same function under quasi-static conditions. Thus F will be identically zero for the quasi-static case. Consider a function F , such as

$$F = \frac{\sqrt{J_2' - 0.13 (J_3')^{2/3}}}{\sqrt{J_{2_0}' - 0.13 (J_{3_0}')^{2/3}}} - 1 \quad (5.4)$$

where the lower subscript 'o' refers to the quasi-static conditions.

For a perfectly plastic material under quasi-static conditions, $f_0(J_2', J_3')$ is a constant equivalent to the value at yield but for a work hardening type material, f_0 is a function of strain. In the

present formulation, the latter case is considered.

Since most of the dynamic properties are available under a uniaxial state of stress, F for such a case can be evaluated as follows:

$$F = \frac{\sqrt{\frac{\sigma^2}{3} - 0.13 \left(\frac{2}{27} \sigma^3\right)^{2/3}}}{\sqrt{\frac{\sigma_0^2}{3} - 0.13 \left(\frac{2}{27} \sigma_0^3\right)^{2/3}}} - 1$$

$$F = \frac{\sigma(\epsilon)}{\sigma_0(\epsilon)} - 1 \quad (5.5)$$

where $\sigma(\epsilon)$, and $\sigma_0(\epsilon)$ represent the dynamic and quasi-static stresses as functions of strain.

To find a relationship between $\dot{\epsilon}_{ij}^P$ and F , the experimental results of Rand et al. [79], Lindholm [25], Maiden et al. [81], Hauser et al. [82], and Karnes et al. [83] were used. Several combinations of $\dot{\epsilon}_{ij}^P$ and F were tried, but it was found that the plot of $\ln(e^F - 1)$ - vs - $\ln\left(\frac{\dot{\epsilon}}{\dot{\epsilon}_0}\right)$ with strain as a parameter to be nearly linear as shown in Figure 5.1. Thus the constitutive equation can be represented as;

$$\ln(e^F - 1) = m \left(\ln \frac{\dot{\epsilon}}{\dot{\epsilon}_0}\right) + C \quad (5.6)$$

where m , and C are functions of strain. To determine the functions m and C they were plotted against strain, ϵ , and the typical plots

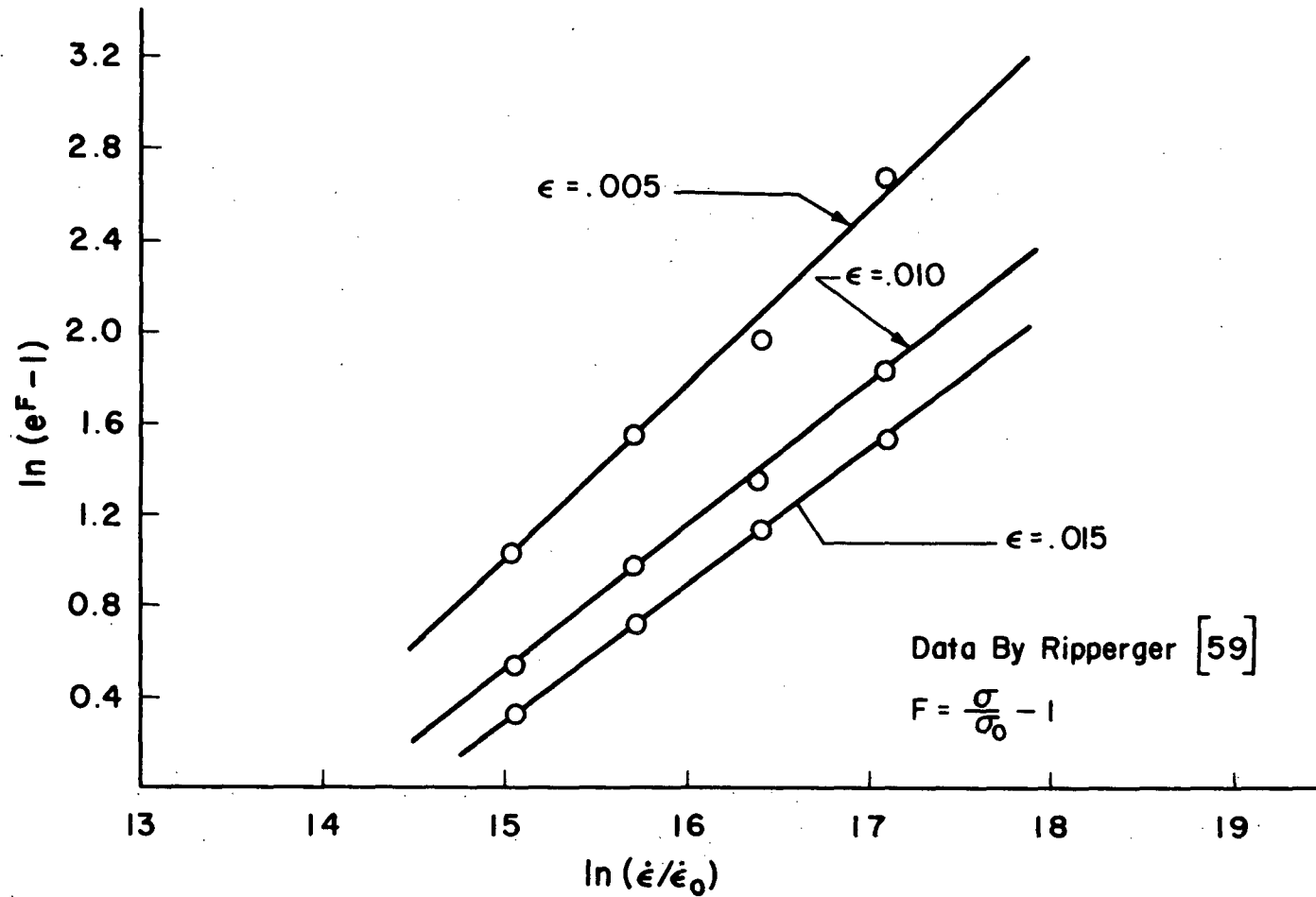


Fig. 5-1 Plot of $\ln(\exp F - 1)$ - vs - $\ln(\dot{\epsilon}/\dot{\epsilon}_0)$ for Annealed Aluminum

are shown in Figure 5.2. Thus m and C exhibited a quadratic dependence on strain, which can be represented as follows:

$$m = a_1 \epsilon^2 + b_1 \epsilon + c_1 \quad (5.7)$$

$$C = a_2 \epsilon^2 + b_2 \epsilon + c_2 \quad (5.8)$$

Thus the constitutive equation can be written as;

$$\ln(e^F - 1) = (a_1 \epsilon^2 + b_1 \epsilon + c_1) \left[\ln \left(\frac{\dot{\epsilon}}{\dot{\epsilon}_0} \right) \right] + (a_2 \epsilon^2 + b_2 \epsilon + c_2) \quad (5.9)$$

where the six constants a_1 , b_1 , c_1 , and a_2 , b_2 , c_2 characterizing the material are to be determined from the experimental data. The stress-strain curves at different strain rates obtained by evaluating equation (5.9) are shown in Figure 5.3 for high purity aluminum which is typical of the materials that were examined. The agreement between the theory and the experiment can be noted. Stress-strain curves for strain rates not obtainable in laboratory are predicted assuming equation (5.9) to be applicable.

Even though equation (5.9) was found to be applicable over a wide range of strain rates, difficulty arose when quasi-static conditions are approached. This is due to the asymptotic behavior of a logarithmic function in the vicinity of zero. A small error as shown in Figure 5.3 seemed to exist at quasi-static conditions and an expression for such an error can be developed as follows:

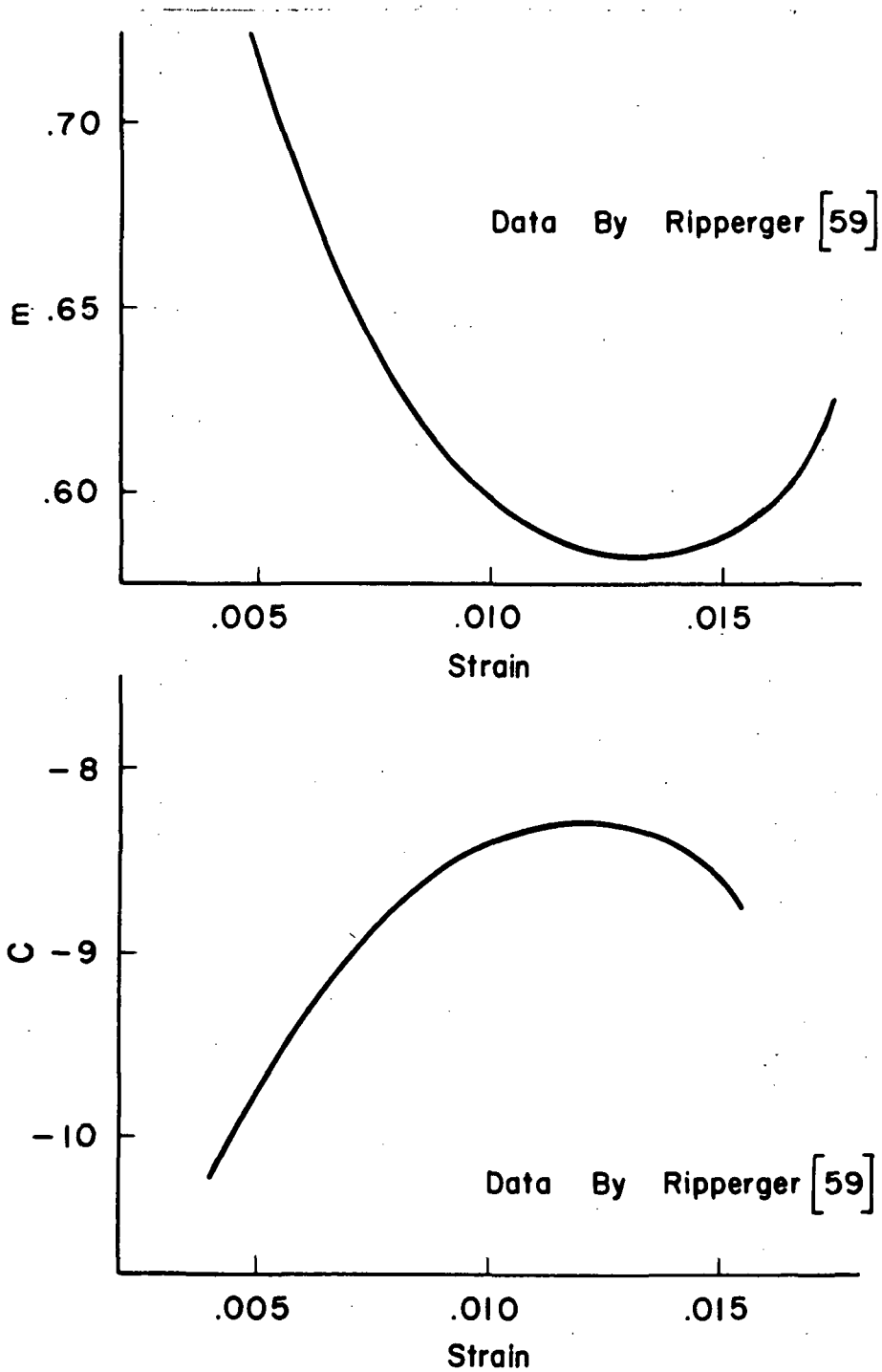


Fig. 5-2 Functional Relationship of m and C with Respect to Strain for Annealed Aluminum, $\ln(\exp F - 1) = m\{\ln(\dot{\epsilon}/\dot{\epsilon}_0)\} + C$

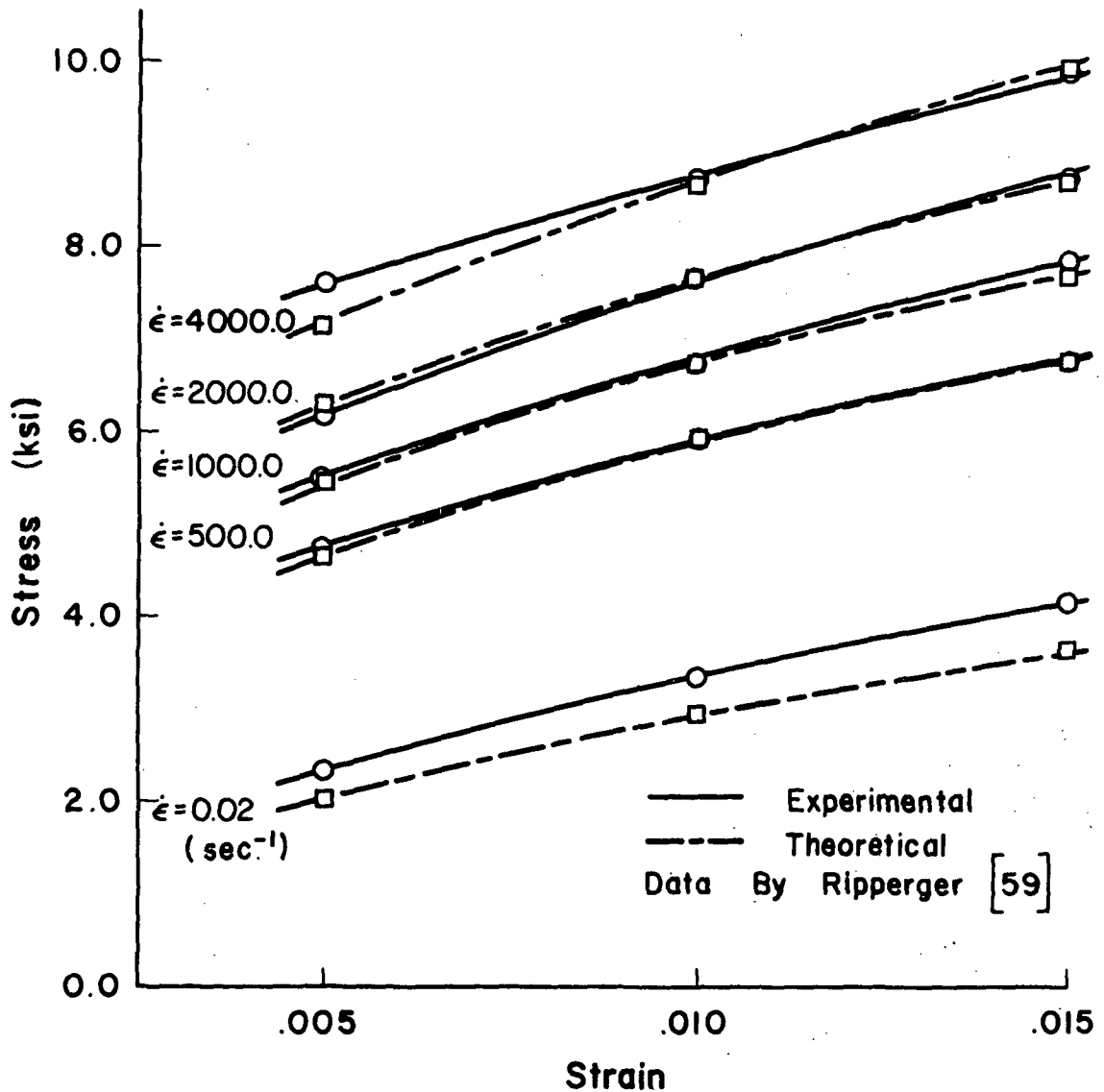


Fig. 5-3 Experimental and Theoretical Rate Sensitivity for Annealed Aluminum (99.995 % Pure)

when $\dot{\epsilon} = \dot{\epsilon}_0$; equation (5.9) leads to

$$\ln (e^F - 1) = C$$

$$e^F - 1 = e^C$$

$$\frac{\sigma}{\sigma_0} - 1 = \ln (e^C + 1)$$

$$\sigma - \sigma_0 = \sigma_0 \{ \ln (e^C + 1) \} \quad (5.10)$$

C was found to be a negative number for all the materials resulting in a small error. In the case of annealed aluminum, this error was 7.78% at a strain of 0.01. Thus the development of a constitutive equation was not met with full success, but a reasonably close agreement with experimental results in the regions of interest encouraged its adaptation into the penetration equations.

CHAPTER VI

EXPERIMENTAL PROCEDURE

Need For Experimentation

The reasons for planning this experimental program were threefold.

1. To assess the properties of the materials that were actually used. Especially with reference to pure aluminums, the properties differ very significantly with the purity content and the amount of heat treatment. Also the dynamic properties reported by different researchers apparently for the same material varied significantly. This is due to the minor variations in strain history and testing procedure.
2. To obtain the dynamic experimental data for steel, as scarcity existed in such data. Also to see whether the yield phenomenon that occurs with heat treated mild steels under quasi-static conditions will also occur under dynamic conditions.
3. To obtain static and dynamic properties which will be more representative of the materials used by conducting experiments on pieces of material from the same stock that was used in hyper-velocity impact experiments. This consequently minimizes the possible sources of variation that might result when data from other investigators are used. Thus influence of the purity content

and heat treatment on the properties of the materials and in some cases scarcity of the available experimental data and the motive of increasing the representativeness of the data are the reasons for conducting the quasi-static and dynamic testing of the materials. The hypervelocity impact experiments were planned to verify the theory developed.

The materials chosen for experimentation have a particular characteristic associated with each of them in regard to their plastic deformation thus encompassing different kinds of materials that are of theoretical and practical importance. Commercially pure 1100 aluminum is strain rate sensitive whereas the 6061-T6 aluminum alloy is reportedly insensitive to strain rate. Commercially pure lead is soft and almost non strain hardening whereas SAE 1018 plain carbon steel is strain hardening and exhibits a well defined yield point under quasi-static conditions.

The actual experimental procedure consists of the following three phases:

1. To determine the quasi-static properties of the target materials.
2. To determine the dynamic properties of the target materials.
3. To subject semi-infinite targets of the four materials to hypervelocity impact.

A semi-infinite target of a homogeneous material may be defined as a target with such a thickness that the rear free surface has

negligible influence on impact damage for a given set of impact conditions.

The target materials were prepared in the following manner: 1100 aluminum and 6061 aluminum alloy were used in the as received condition whereas lead was cast into nominal 4 in. x 4 in. x 1.25 in. plates. Mild steel was heat treated to accentuate the sharply defined yield stress. 4 in. x 4 in. x 1.25 in. mild steel plates were packed in boxes with cast iron chips and were kept in a muffle furnace for 2 hours at 1660°F and then furnace cooled to room temperature. Then they were kept at 400°F for 10 hours and furnace cooled again to room temperature.

Quasi-Static Tests

The specimens for the quasi-static tests were machined from the same stock of materials which were used for the hypervelocity impact experiments. These specimens were used to assess the properties of the materials along the direction of thickness. They were machined into cylindrical plugs with a nominal length to diameter ratio (l/d) of 1.25 for all the materials. Shallow circular grooves were machined on both the ends of the cylindrical specimens to hold the lubricant during testing and consequently minimize the barreling effects.

The quasi-static compression tests were carried out on the cylindrical specimens along the lines suggested by Loizou et al. [84].

These tests were carried out on a Baldwin Universal testing machine to determine the quasi-static properties of the target materials along the direction of impact. The quasi-static strain rates ranged from 0.000129 to 0.000837 sec.⁻¹. Both the end faces of the uniaxial compression test specimens were lubricated with an oil mixed with graphite powder to avoid barreling and the accompanying three-dimensional stress distribution effects. The true stress-logarithmic strain diagrams of the four materials, calculated as follows, are shown in Figures 6.1 to 6.4. Assuming the volume to be constant during plastic deformation, the following expressions can be written for the stress and strain.

Considering compressive stress and strain as positive quantities;

$$\text{Nominal stress} = \frac{\text{Load}}{\text{Original area of cross section}}$$

$$\sigma_e = \frac{P}{A_o} \quad (6.1)$$

$$\text{Nominal or Engineering Strain} = \frac{\text{Change in length}}{\text{Original Length}}$$

$$\epsilon_e = \frac{\Delta L}{L_o} = \frac{L_o - L}{L_o} \quad (6.2)$$

From the constant volume condition, we have:

$$A_o L_o = AL \quad (6.3)$$

$$\text{True Stress} = \frac{\text{Load}}{\text{Actual instantaneous area of cross section}}$$

$$\sigma = P/A \quad (6.4)$$

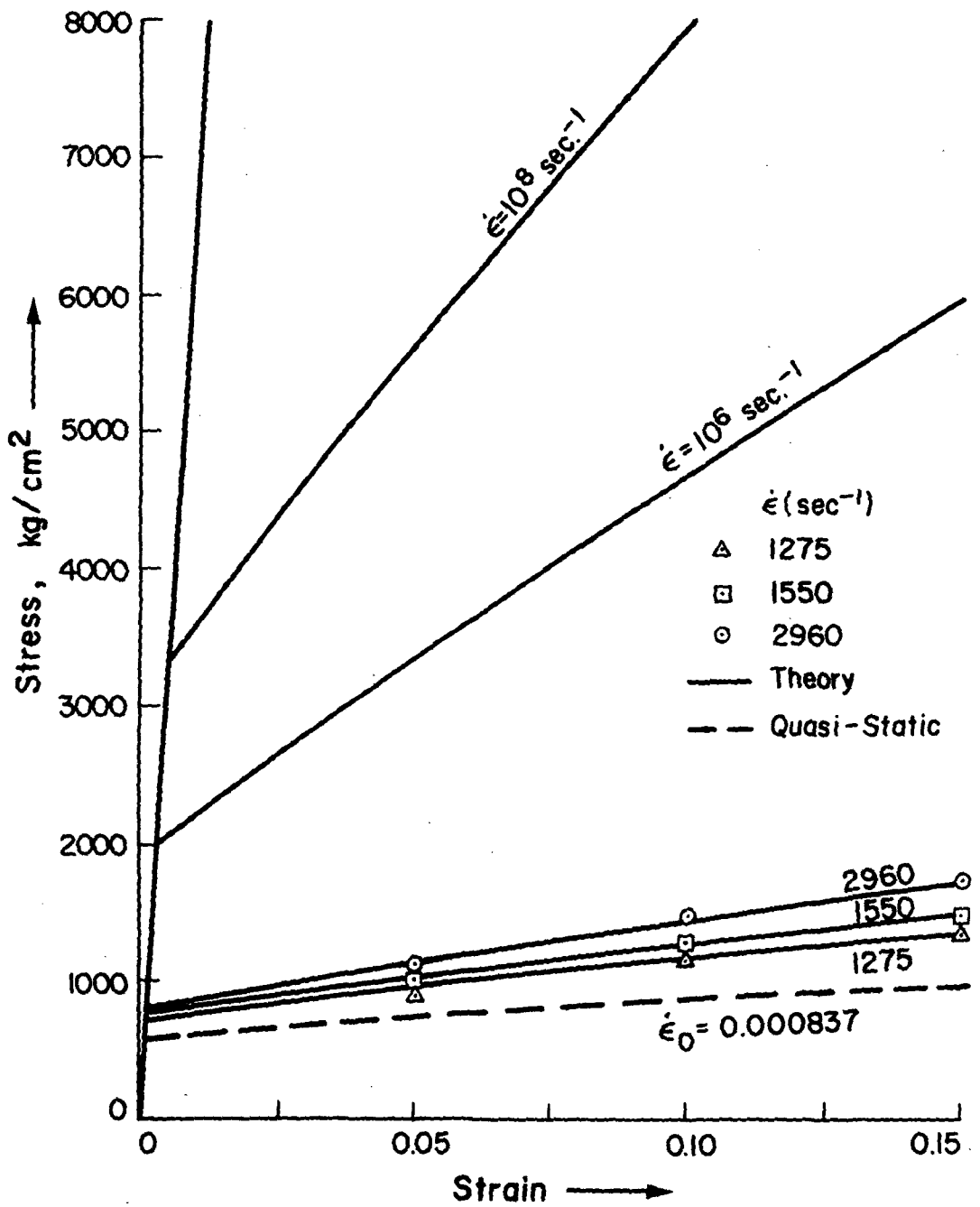


Fig. 6-1 Quasi-Static and Dynamic Response of 1100 Aluminum

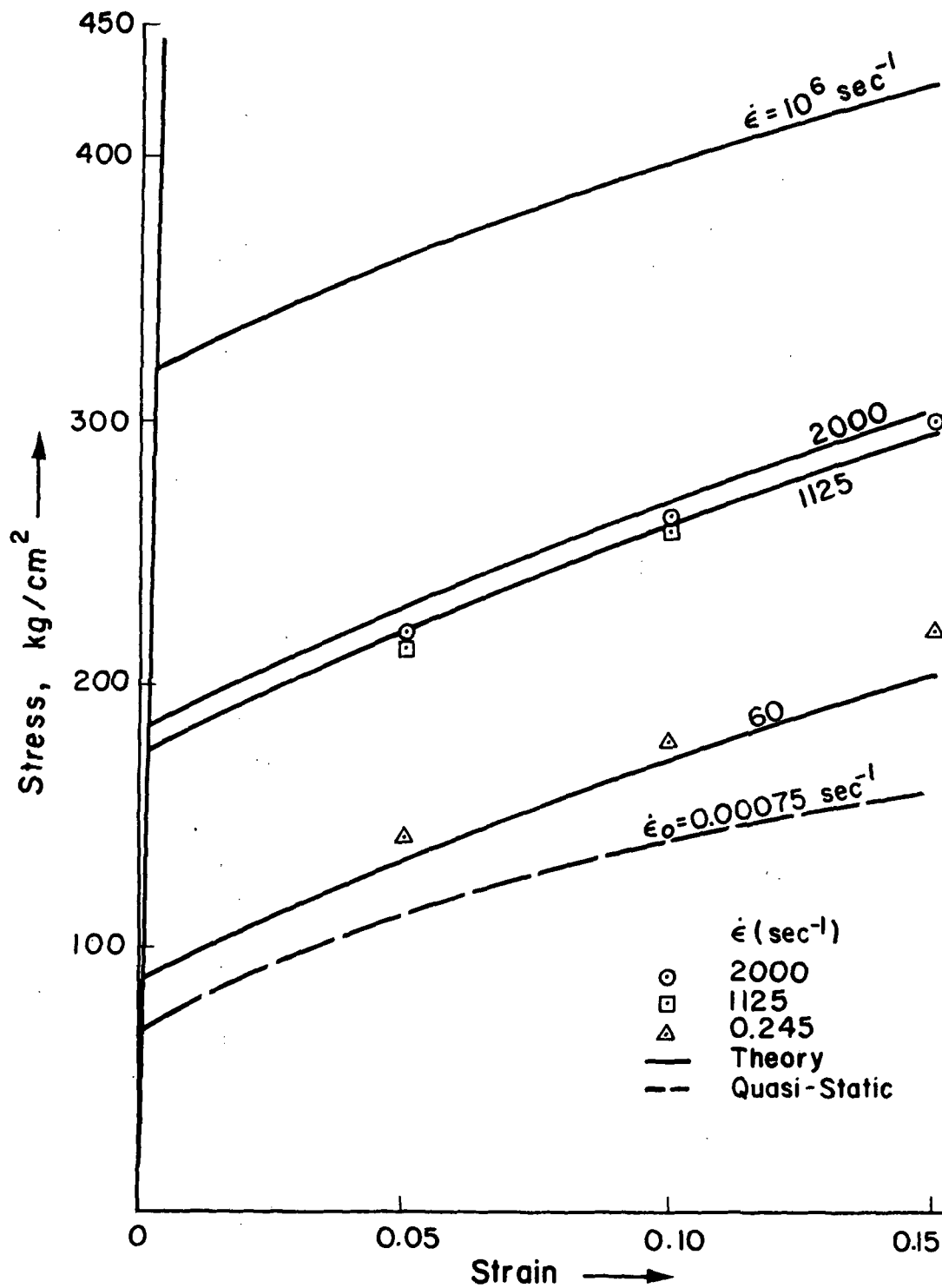


Fig. 6-2 Quasi-Static and Dynamic Response of Commercially Pure Lead

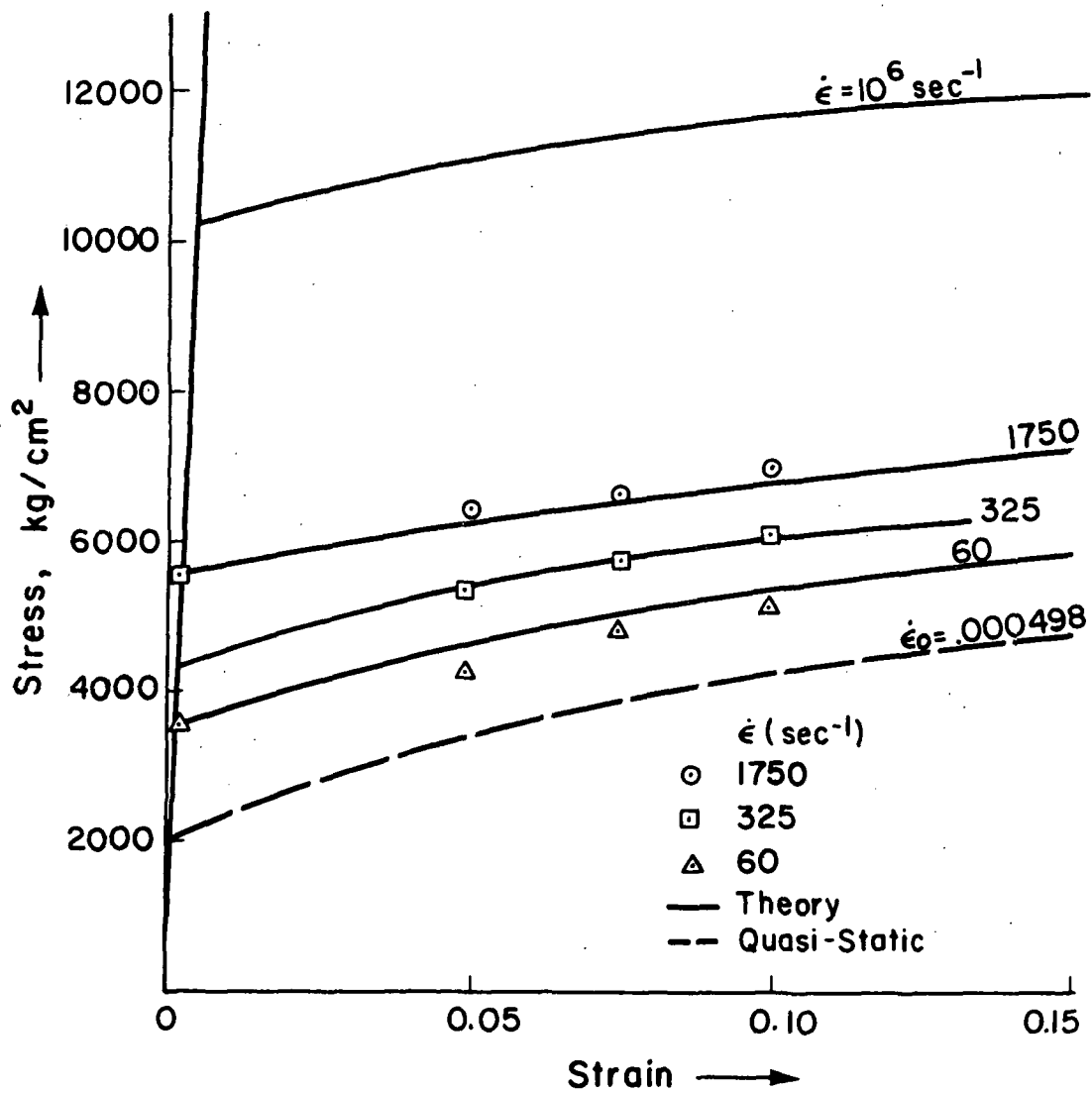


Fig. 6.3 Quasi-Static and Dynamic Response of Mild Steel

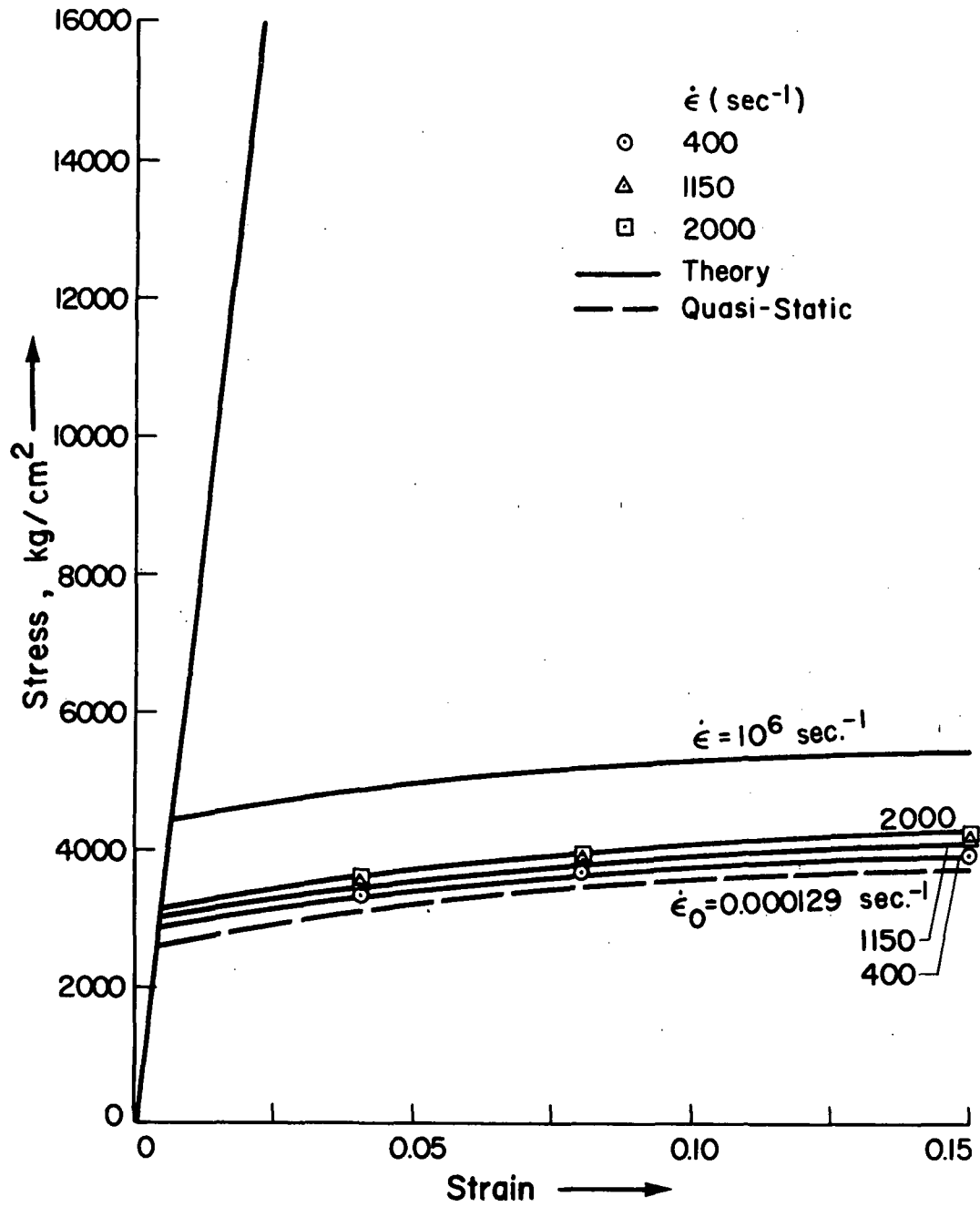


Fig. 6-4 Quasi-Static and Dynamic Response of 6061 Aluminum Alloy

$$\text{From (6.3), } A = A_0 \frac{L_0}{L}$$

$$\therefore \sigma = \frac{P}{A_0} \frac{L}{L_0} \quad (6.5)$$

Thus the absolute value of the true compressive stress is always less than the engineering compressive stress. True or logarithmic strain = $\ln \left(\frac{\text{Instantaneous Length}}{\text{Original Length}} \right)$.

$$\epsilon = \ln \left(\frac{L}{L_0} \right) = \ln \left(\frac{A_0}{A} \right) \quad (6.6)$$

$$\epsilon = \ln \left(1 - \frac{\Delta L}{L_0} \right)$$

Thus the absolute value of true strain is always greater than the engineering strain.

The static hardness of target samples before impact was also tested on a Rockwell Hardness Tester. Table 6.1 shows the Rockwell hardness numbers.

Dynamic Testing

To obtain the dynamic properties of the four experimental materials, a split Hopkinson pressure bar apparatus was used. Nominal 5/16 in. diameter specimens having length to diameter ratios of 1, 1.5, and 2 were used to generate stress-strain curves at various strain rates. The split Hopkinson pressure bar apparatus consists of a small bore air gun to launch a projectile, an incident pressure bar with strain gages to trigger the recording

Table 6.1 Initial Rockwell Hardness of Target Samples.

Material	Load in kg.	Diameter of Ball, inches	Rockwell Hardness Numbers	Average Rockwell Hardness Number
Mild Steel	100	1/16	52.1,52,55,53,51.2,50	B 52.2
"	100	1/8	83.2,83.6,82,84.6	E 83.3
6061 Al.alloy	100	1/16	53.7,55.6,55.2,54.1	B 54.6
"	100	1/8	89.6,95,92.5,91.1	E 92.0
1100 Al.	100	1/16	40,40.6,41.2	B 40.6
"	100	1/8	58.5,63.1,60.8,65.1,54.5	E 60.4
Lead	160	1/4	33.7,35.1,32.3,33.7	L 33.7

equipment and to measure the incident and reflected strains in the incident pressure bar, and a transmitter pressure bar with strain gages to measure the transmitted strain. The specimen is held in between the incident and transmitter pressure bars by friction. The incident, reflected, and transmitted pulses recorded as strains in the pressure bars - vs - time were used to determine the stress, strain, and strain rate acting on the specimen.

Using the condition for conservation of momentum which always holds in the elastic pressure bars;

$$\sigma = \rho c U_p \quad (6.7)$$

$$\sigma = E\epsilon$$

$$U_p = \frac{dx}{dt}$$

where E , σ , ϵ , ρ , c , x , and U_p denote respectively the modulus of elasticity, stress, strain, density, velocity of sound, particle displacement and particle velocity of the pressure bars. The split

$$\dot{x}_1 = \frac{E}{\rho c} (\vec{\epsilon}_I - \vec{\epsilon}_R)$$

$$\therefore \dot{x}_1 = \frac{E}{\rho c} (\vec{\epsilon}_I + \vec{\epsilon}_R)$$

$$\dot{x}_2 = \frac{E}{\rho c} \vec{\epsilon}_T$$

Hopkinson pressure bar apparatus is shown in Figure 6.5.

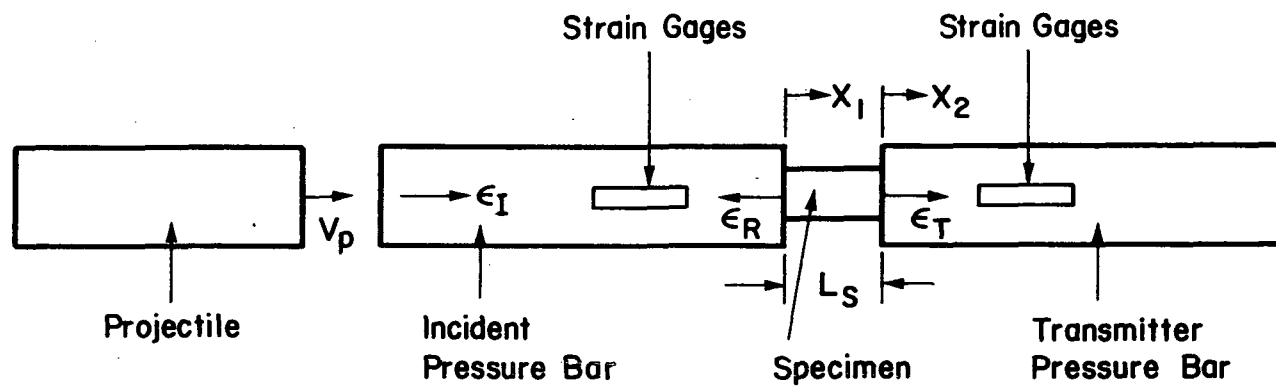


Fig. 6.5 Split Hopkinson Pressure Bar Apparatus

The average strain rate, $\dot{\epsilon}_{ave}$, over a specimen of length, L_s is;

$$\dot{\epsilon}_{ave} = \frac{(\dot{x}_2 - \dot{x}_1)}{L_s}$$

$$\dot{\epsilon}_{ave} = \frac{E}{cL_s} (|\epsilon_I| + |\epsilon_R| - |\epsilon_T|) \quad (6.8)$$

and the average strain, ϵ_{ave} , at any instant, t , and the average stress, σ_{ave} , are given by:

$$\epsilon_{ave} = \frac{E}{\rho c L_s} \int_0^t (|\epsilon_I| + |\epsilon_R| - |\epsilon_T|) dt \quad (6.9)$$

$$\sigma_{ave} = E \left\{ (|\epsilon_I| - |\epsilon_R|) \left(\frac{d_I}{d_s}\right)^2 + (|\epsilon_T|) \left(\frac{d_T}{d_s}\right)^2 \right\} \quad (6.10)$$

where d_I , d_T , and d_s are the diameters of the incident and transmitter pressure bars, and the specimen respectively.

The reduction of the split Hopkinson bar data, to determine the stress, strain, and strain rate in the specimen according to equations (6.7), (6.6), and (6.5), was accomplished with the aid of a computer. The dynamic stress-strain curves with strain rate as parameter were shown in Figures 6.1 to 6.4 (p. 40-43). The dynamic stress-strain curves of the heat treated mild steel still exhibited the yield phenomenon. The resulting dynamic stress-strain curves coupled with the quasi-static stress-strain curves

were used to obtain the 6 constants in the constitutive equation (5.9) characterizing each of the four materials. These constants are shown in Table 6.2.

Hypervelocity Impact Experiments

After the targets have been prepared and the quasi-static and dynamic properties were determined, the third phase of the experimentation was conducted at the Manned Spacecraft Center, Houston. Spherically shaped pyrex projectiles of different diameters launched from a two stage light gas gun and accelerated to different velocities were allowed to impact normally on semi-infinite targets of the four materials. The general configuration is shown in Figure 6.6. Determination of the velocity of the impacting projectile consisted of photographing the path of projectile between two stations of known spacing located close to the target and finding the time of travel between those stations. A depth gage was used to measure the penetration depths from the original target surface. The resulting penetration depths, P_c , are recorded in Table 6.3. Subsequently these penetration depths obtained experimentally will be compared with the predicted values. Thus the experimental part of the work concludes with hypervelocity impact experimentation.

Table 6.2 Constants in Constitutive Equation

$$\ln(e^F - 1) = (a_1 \epsilon^2 + b_1 \epsilon + c_1) \ln(\dot{\epsilon}/\dot{\epsilon}_0) + a_2 \epsilon^2 + b_2 \epsilon + c_2$$

Material	a_1	b_1	c_1	a_2	b_2	c_2
6061 Al. alloy	-1.1466	0.2751	0.2705	43.3327	-11.4625	-6.3232
Lead	3.9805	-1.4344	0.3008	5.5755	4.6074	-3.0165
Mild Steel	0.5676	-0.6796	0.3242	108.0222	-17.0876	-3.5176
1100 Al.	-7.7878	3.5890	0.5135	125.8566	-49.7586	-8.3318

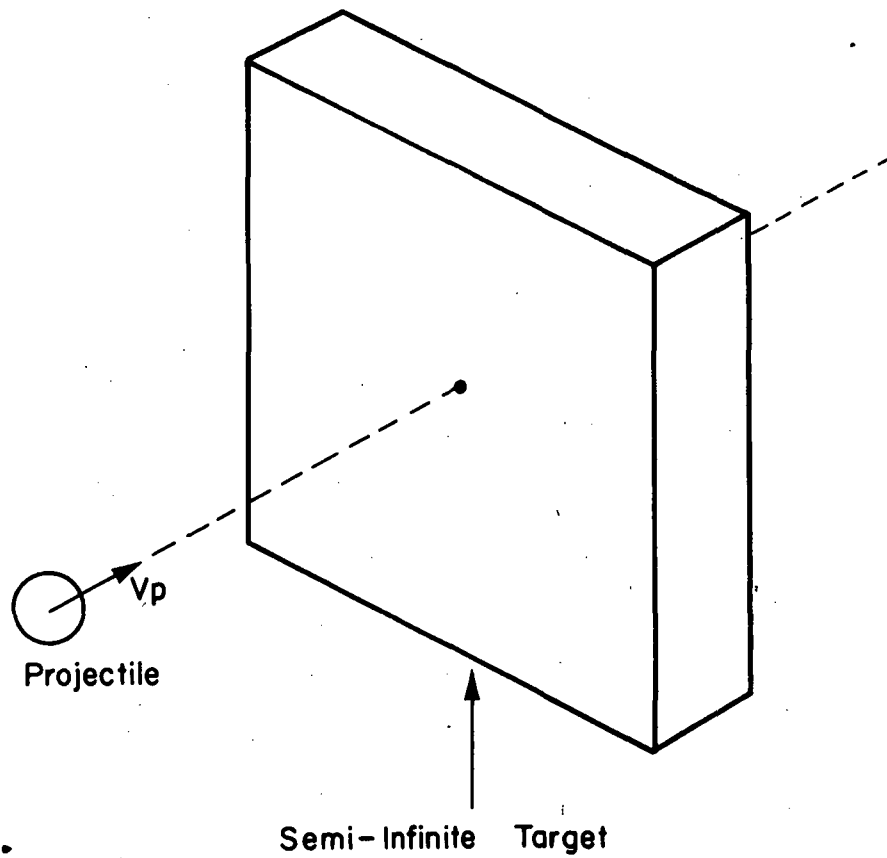


Fig. 6.6 Hypervelocity Impact Test Configuration

Table 6.3 Penetration Depths

Target Number	Target Material	Projectile		Penetration depth P_c , cm.
		Diameter d_p , cm.	Velocity v_p , km./sec.	
6-106	1100 Aluminum	0.159	5.580	0.3937
6-117	"	0.100	5.520	0.2400
6-161	"	0.159	8.330	0.4440
6-162	"	0.159	8.300	0.4430
6-108	6061 Al. alloy	0.159	5.600	0.2870
6-124	"	0.100	6.140	0.2004
6-147	"	0.040	6.030	0.0685
6-111	Mild Steel	0.159	5.620	0.1640
6-146	"	0.100	6.130	0.1102
6-109	Lead	0.159	5.270	0.3914
6-127	"	0.100	6.120	0.2590

Projectile material: Pyrex

CHAPTER VII

DETERMINATION OF STRAIN RATES IN HYPERVELOCITY IMPACT

General Discussion of the Problem

In spite of the complexities involved with the hypervelocity impact process, certain simplified but reasonable assumptions can be made to theoretically analyze the problems. The determination of strain rates based on rarefaction and strength effects as the shock wave propagates through the target is essential to evaluate the dynamic strength of the target. The impact of a hypervelocity projectile results in strong shock waves which originate from the projectile-target interface and propagate into the projectile and target materials. The principal achievement by researchers to this stage is the application of the hydrodynamic theory to initial stages of the cratering process with an extraordinary success. But the consideration of strength effects that come into play during the later stages appeared to be least attempted till now.

Since the present work limits its consideration to semi-infinite targets, the effects of rear free surface and the consequent rarefactions are neglected. Even though the aim of the present work is to predict the final damage caused to the target, it is just not possible to give consideration only to the final stages and avoid giving consideration to the initial hydrodynamic stages. The

reason for this is that one has to know the entire history of the propagating shock wave. It is assumed that the shock wave in the target is a plane wave. As the rarefaction wave from the projectile catches up with the advancing shock wave in the target, attenuation of the peak pressure and the changes in shape of shock wave are caused. But when one limits consideration to the vicinity of axis of symmetry (Figure 7.1a), it is still reasonable to assume a plane wave. The justification for this assumption is based on several of the field plots, displaying particle velocity and principal stress distributions in a target during the hypervelocity cratering process as derived by various researchers such as Rosenblatt [64]. The particle velocity plots show a one-dimensional nature along the axis of symmetry. Considering the wave to be a plane uniform compressional shock wave, any element $cd'fg$ will be compressed to $c'd'fg$ as shown in Figure 7.1b. Because the wave is plane and compressive, no macroscopic lateral motion of the material can occur, and any slip must be on a microscopic scale.

Determination of the Initial Pressure and Shock Wave Speeds Generated due to Impact

The determination of the initial pressure, projectile-target interface velocity, the speeds of the shock waves that originate from the interface and propagate into the projectile and target are based on the Hugoniot properties of the projectile and target materials. Los Alamos Scientific Laboratory has been devoting a

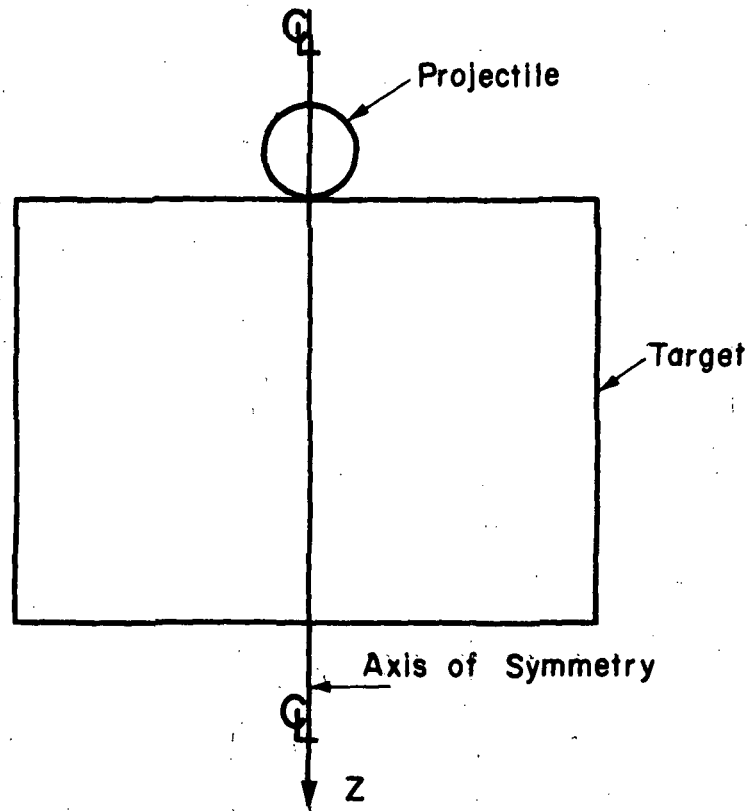


Fig. 7-1a Schematic Diagram Showing the Axis of Symmetry

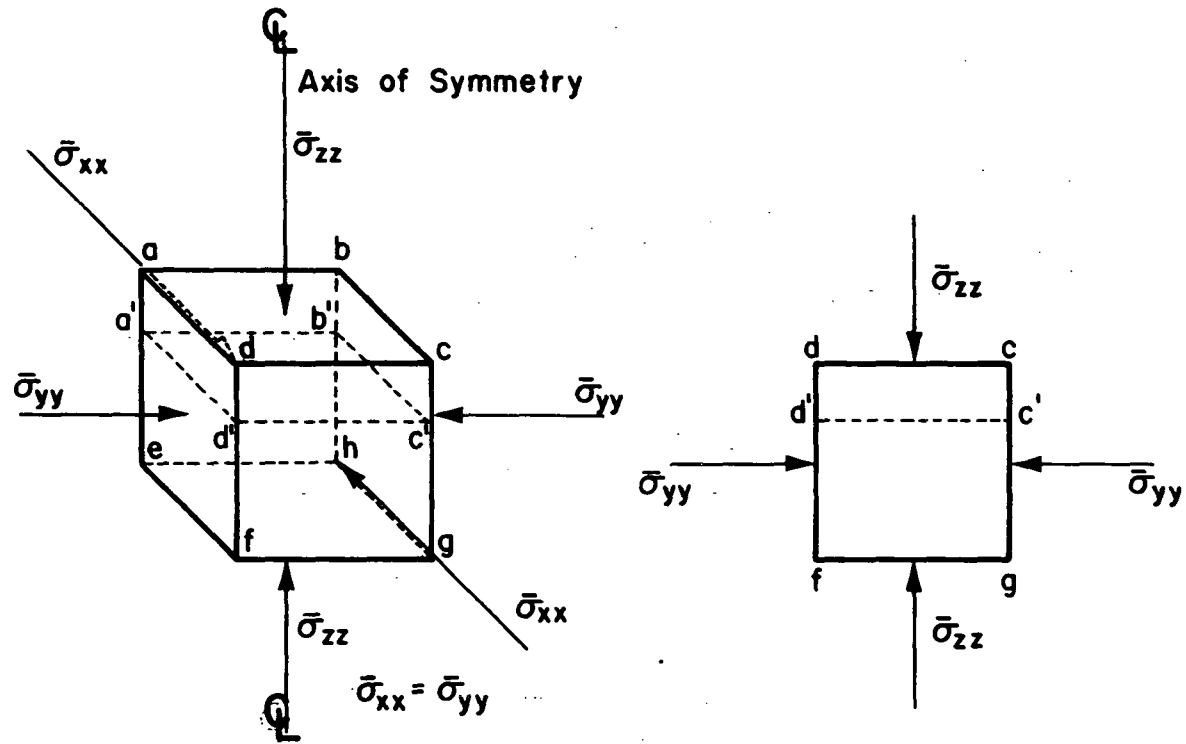


Fig. 7-1b Configuration of Stresses in an Element Compressed by a Plane Shock Wave

continuing effort to measure the equations of state and the Hugoniot properties of solids by shock wave techniques. The Hugoniot properties as reported by Rice et al. [17], Walsh et al. [18, 19], McQueen et al. [21, 85] and Al'tshuler et al. [22, 23, 24] were used. A graphical impedance matching technique was employed to solve for the initial pressure p_i , and the interface velocity U_{pti} . This technique states that the sum of the particle velocities U_{pti} and U_{ppi} of the target and projectile at the interface must equal to the impact velocity of the projectile, V_p .

$$V_p = U_{pti} + U_{ppi} \quad (7.1)$$

The application of this technique consists of plotting the direct pressure-particle velocity (p-vs-Up) shock Hugoniot of the target material and the reflected p-vs-Up shock Hugoniot of the projectile material corresponding to the projectile velocity. The point of intersection of these two Hugoniots determines the initial pressure, p_i , and particle velocities of the projectile and target materials, namely U_{ppi} and U_{pti} . This method was applied to all the targets and is illustrated in Figure 7.2 for a lead target. The resulting values are tabulated in Table 7.1. To determine the initial shock speeds U_{sti} and U_{spi} in the target and projectile, the Rankine-Hugoniot relations for the conservation of mass and momentum across the shock

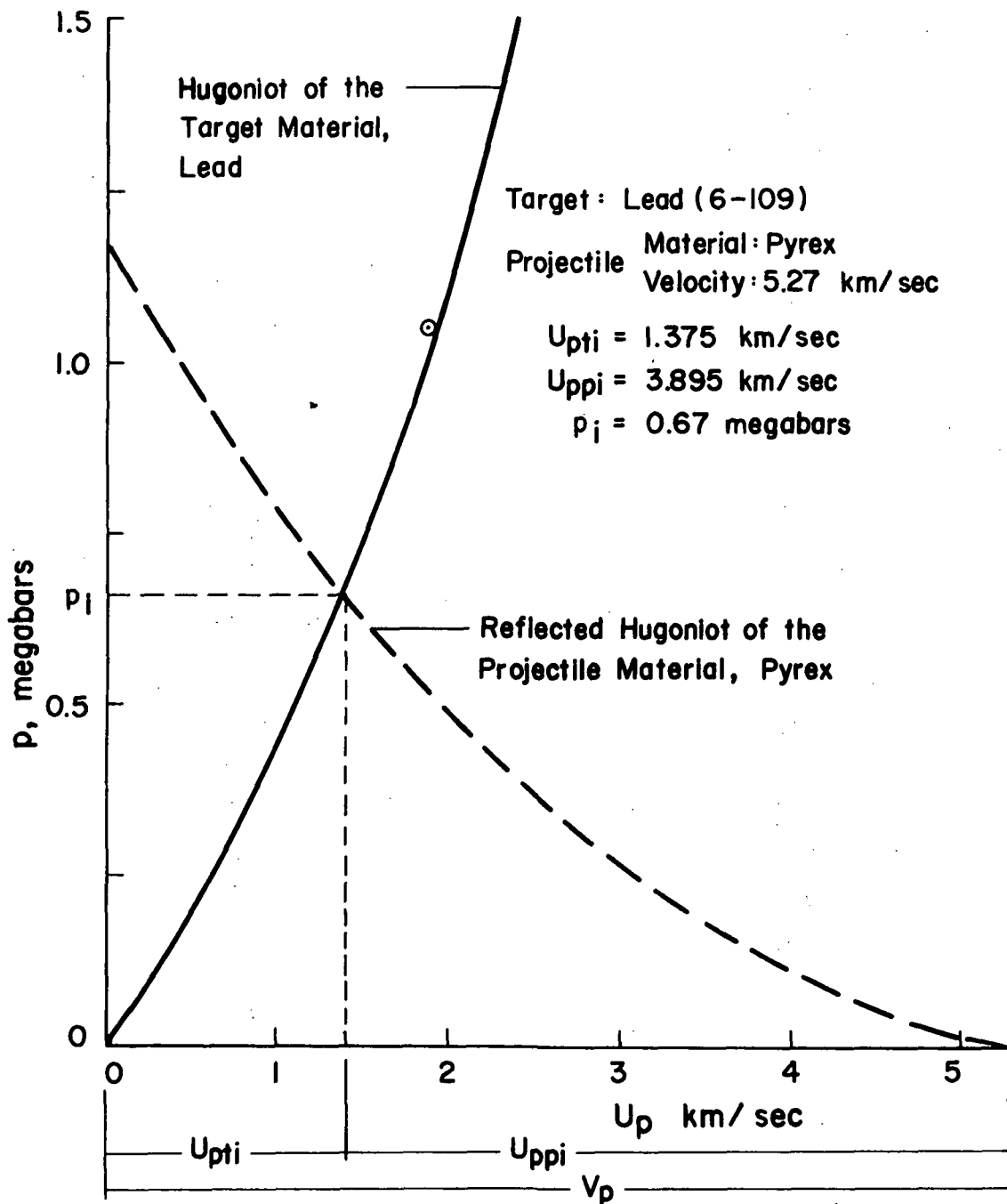


Fig.7-2 Graphical Impedance Matching

Table 7.1 Impact Hugoniot Values

Shot Number	Target Material	Projectile diameter d_p , cm	Projectile Velocity V_p , km/sec.	P_i megabars	U_{pti} km/sec.	U_{sti} km/sec.	U_{ppi} km/sec.	U_{spi} km/sec.	Z_1 cm	t_1 μ sec.
6-106	1100 Al.	0.159	5.580	0.513	2.213	8.300	3.368	6.902	0.635	0.765
6-117	"	0.100	5.590	0.523	2.240	8.310	3.350	6.975	0.396	0.476
6-161	"	0.159	8.330	0.968	3.515	9.988	4.815	9.900	0.457	0.457
6-162	"	0.159	8.300	0.963	3.500	9.972	4.800	9.880	0.458	0.459
6-108	5061 Al. alloy	0.159	5.600	0.523	2.240	8.337	3.360	6.979	0.826	0.991
6-124	"	0.100	6.140	0.620	2.500	8.736	3.640	7.471	0.708	0.811
6-147	"	0.040	6.030	0.579	2.435	8.572	3.595	7.219	0.153	0.178
6-111	Mild Steel	0.159	5.620	0.728	1.525	6.267	4.095	8.133	0.419	0.668
6-146	"	0.100	6.130	0.850	1.700	6.555	4.430	9.100	0.216	0.330
6-109	Lead	0.159	5.270	0.670	1.375	4.100	3.895	7.776	0.245	0.597
6-127	"	0.100	6.120	0.850	1.650	4.543	4.470	9.100	0.143	0.314

Projectile material: Pyrex

can be used. These initial shock speeds

$$\rho_o U_s = \rho (U_s - U_p)$$

$$p = \rho_o U_s U_p$$

$$U_s = \sqrt{\frac{p}{\rho_o} \frac{\rho}{(\rho - \rho_o)}} \quad (7.2)$$

were computed and included directly into Hugoniot properties of the materials. Those values were also shown in Table 7.1. These initial impact Hugoniot values are thus dependent only on the projectile and target materials and projectile velocity and independent of the projectile diameter. The pressures generated are of the order of one megabar and hence the applicability of the hydrodynamic theory is evident.

Calculation of the Steady State Regime

For a short time t_1 after impact the peak pressure of the pulse propagating into the target will remain undisturbed at the impact Hugoniot value P_i . The speed of propagation U_{sti} of the shock wave in the target will also be undisturbed. After a time period t_1 corresponding to an axial distance Z_1 , the rarefaction front originating at the rear surface of the projectile catches up with the advancing shock front in the target and attenuates its peak pressure. The rarefaction wave can catch up with the

advancing shock front in the target because it travels through the shock processed projectile and part of the target materials. The shocking process is nonisentropic and hence is to be based on the Hugoniot properties of the materials whereas the release process due to rarefaction waves is to be based on isentropic properties of the materials. With these considerations in mind, the expressions for the distance Z_1 below the original target surface and the time t_1 corresponding to the region of unattenuated peak pressure in the target may be derived as follows. The characteristic diagrams for the cases when the projectile velocity V_p is less than the shock speed in the projectile U_{sp} and when V_p is greater than U_{sp} are shown in Figure 7.3 and 7.4.

From the characteristic diagram (Fig. 7.3), it can be noted that

$$V_p = \frac{Z_c}{t_a}$$

$$U_{sp} = \frac{Z_e}{t_a} = \frac{d_p - Z_c}{t_a} = \frac{d_p - V_p t_a}{t_a}$$

$$t_a = \frac{d_p}{U_{sp} + V_p}$$

$$c_r = \left(\frac{\partial p}{\partial \rho_s} \right)$$

$$U_{pti} + c_{rp} = \frac{Z_a + Z_e}{t_a + t_b}$$

$$U_{pti} = \frac{Z_a}{t_a + t_b} ; \frac{Z_e}{t_a} = U_{spi}$$

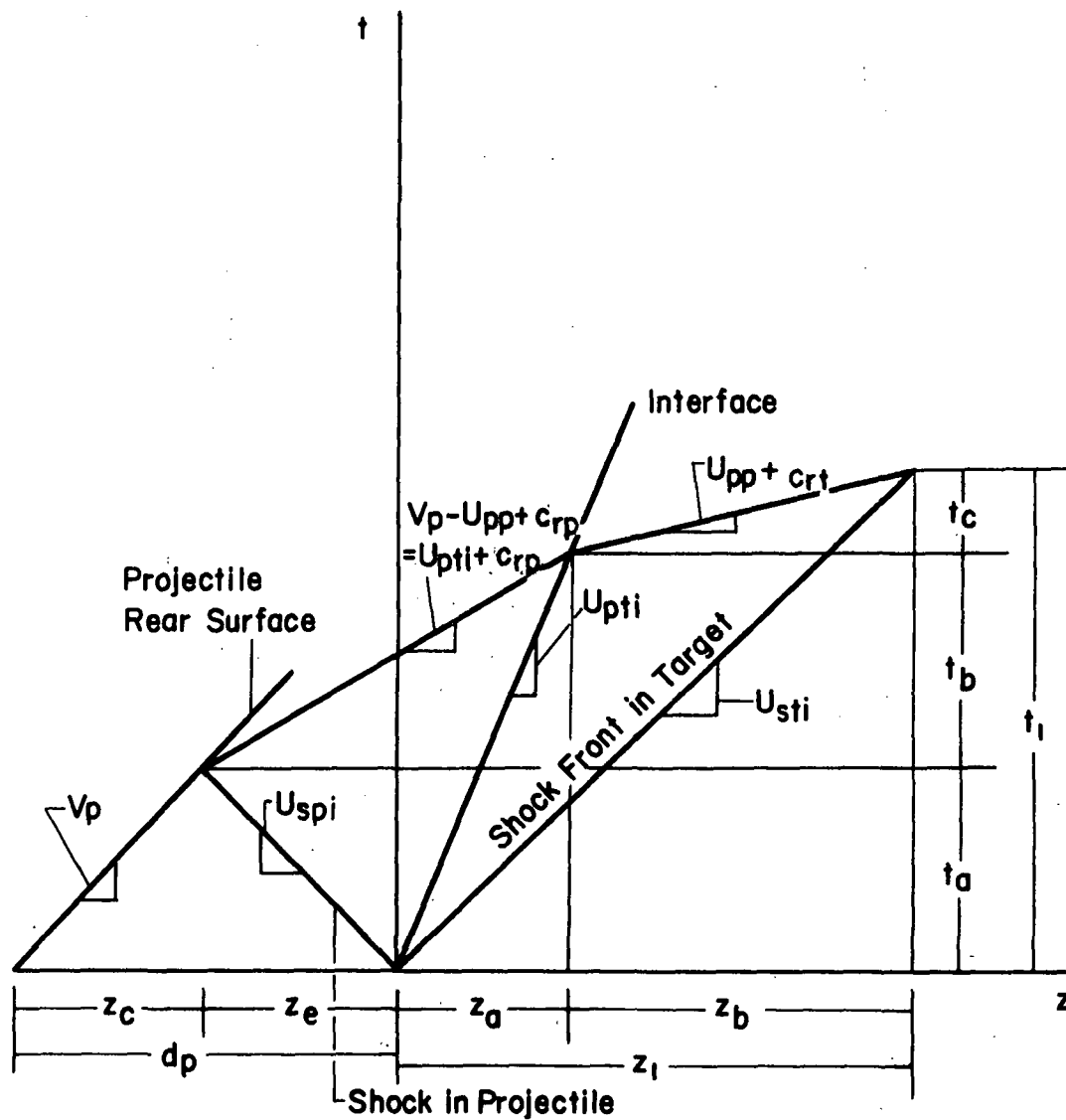


Fig. 7.3 Characteristic Diagram $v_p < U_{spi}$

Eliminating, Z_a & Z_e , we have

$$t_b = \frac{U_{pti} + U_{spi}}{c_{rp}} t_a$$

$$U_{pti} + c_{rt} = \frac{Z_b}{t_c}$$

$$U_{sti} = \frac{Z_a + Z_b}{t_a + t_b + t_c}$$

$$t_c = \frac{U_{sti} - U_{pti}}{U_{pti} + c_{rt} - U_{sti}} (t_a + t_b) \quad (7.4)$$

$$t_1 = t_a + t_b + t_c$$

$$t_1 = \frac{c_{rt}}{U_{ppi} + c_{rt} - U_{sti}} \frac{U_{ppi} + U_{spi} + c_{rp}}{c_{rp}} \frac{d_p}{U_{spi} + V_p}$$

$$\text{(when } V_p < U_{spi}\text{)} \quad (7.5)$$

$$Z_1 = U_{sti} t_1 \text{ (when } V_p < U_{spi}\text{)} \quad (7.6)$$

The characteristic diagram for the case when $V_p > U_{spi}$ was shown in Figure 7.4. The expression for Z_1 and t_1 may be derived as follows:

$$V_p = \frac{d_p + Z_c}{t_a}$$

$$U_{spi} = \frac{Z_c}{t_a}$$

$$U_{pti} + c_{rp} = \frac{Z_a}{t_b}$$

$$U_{pti} = \frac{Z_a + Z_c}{t_a + t_b}$$

$$U_{pti} + c_{rt} = \frac{Z_b}{t_c}$$

$$U_{sti} = \frac{Z_a + Z_b + Z_c}{t_a + t_b + t_c}$$

$$t_1 = t_a + t_b + t_c$$

$$t_1 = \left[\frac{U_{pti} - U_{spi} + c_{rp}}{U_{pti} - U_{sti} + c_{rt}} \right] \left[\frac{d_p}{V_p - U_{spi}} \right] \frac{c_{rt}}{c_{rp}} \quad (7.7)$$

(when $V_p > U_{spi}$)

$$Z_1 = U_{sti} t_1 \quad (\text{when } V_p > U_{spi}) \quad (7.8)$$

V_p was found to be less than U_{spi} with all of the targets that were tested. Consequently the equations (7.5) and (7.6) were used to compute Z_1 and t_1 . These values were listed in Table 7.1. It can be noted that the initial impact Hugoniot values for a given projectile-target combination are functions of only the projectile

velocity whereas the values of Z_1 and t_1 characterizing the steady state regime are functions of both the projectile diameter and velocity. Increasing the velocity of projectile or decreasing its diameter has the same effect of decreasing Z_1 and t_1 and vice versa.

Attenuation of the Peak Pressure

After the values of Z_1 and t_1 characterizing the steady state regime have been determined, consideration must be directed toward finding the attenuation of the peak pressure associated with the advancing shock front in the target as affected by the rarefactions that caught up with this shock wave. This is an extremely difficult task without a computer code. Such a computer code is not only time consuming but also expensive. Hence, the analytical expressions derived by Heyda et al. [86] from their computer code PICWICK were used. No exact theoretical relationship giving axial shock wave propagation speed as a function of position is known at this time. The approach adopted by Heyda and Riney was based on the following heuristic considerations. When the rarefaction fronts reach the axial position Z_1 there is an intense energy release along the axial direction which occurs in a very short time interval and approximates a line blast. The shock front advancing as a planar front for $Z < Z_1$, is assumed to have, subsequent to the energy release, a speed equal to that of a planar blast wave. This assumption is made in order to

account for the strong axial gradient in the energy dissipation along the axis. Based on the blast wave considerations and computer solutions, their results may be expressed in the following form.

$$U_{st} = \left[\frac{4 A_1 k}{\sqrt{z - z_0}} - \frac{4 A_1 k^2}{(z - z_0)} \right]; \quad z \geq z_1 \quad (7.9)$$

where

$$A_1 = U_{st1} \left[\frac{51 - 44\beta + 8\beta^2 - 3\sqrt{33 - 8\beta}}{8(1 - \beta)(4 - \beta)} \right] \quad (7.10)$$

$$\beta = 4 d_1 \left(1 - \frac{d_1}{d_2} \right) \quad (7.10a)$$

$$d_1 = \frac{p_i}{p_i + \left(1 - \frac{\rho_{ot}}{\rho_t} \right) p_i'} \quad (7.10b)$$

$$d_2 = \frac{2 p_i'}{\left(1 - \frac{\rho_{ot}}{\rho_t} \right) p_i''} \quad (7.10c)$$

$$p_i' = \left[\frac{\partial p_H}{\partial \left(\frac{\rho_{ot}}{\rho_t} \right)} \right] \quad \text{at } p = p_i$$

$$p_i'' = \left[\frac{\partial p_i'}{\partial \left(\frac{\rho_{ot}}{\rho_t} \right)} \right] \quad \text{at } p = p_i$$

p_i' and p_i'' are the first and second derivatives of the p -vs- ρ_{ot}/ρ_t Hugoniot of the target material. Suffix t refers to the target

and ρ refers to the undisturbed condition.

$$\bar{L} = \frac{d_p}{2} (2)^{1/3}$$

$$K_1 = 0.368 \left[1 + 0.15 \left(1 - \frac{\rho_{op}}{\rho_{ot}} \right) \right] \left\{ \frac{v_p}{c_{oh}} \right\}^{1/3} \quad (7.10e)$$

$$k = K_1 \sqrt{\bar{L}} \quad (7.10f)$$

$$Z_o = Z_1 - \left[\frac{2 K_1^2}{1 - \sqrt{1 - \frac{U_{sti}}{A_1}}} \right]^2 \bar{L} \quad (7.10g)$$

where ρ_{op} , ρ_{ot} and c_{oh} are the undisturbed projectile target densities and the U_s -vs- U_p Hugoniot intercept on the U_s axis.

The time of arrival t at an axial location Z of the peak of the pressure pulse propagating in the axial direction in the target can be written as

$$\frac{t}{\bar{L}} = \frac{Z_1}{\bar{L} U_{sti}} + \frac{1}{2 A_1 K_1} \sum_{j=0}^2 \frac{K_1^j}{3-j} \left(\frac{Z - Z_o}{\bar{L}} \right)^{\frac{3-j}{2}} + K_1^3 \ln \left(\frac{Z - Z_o}{\bar{L}} - K_1 \right) - K_1^3 \left(\ln K_1 + \frac{20}{3} \right) \quad (7.11)$$

Using the above equations and the Hugoniot properties of the materials the particle velocities corresponding to various locations along the axis of symmetry were calculated and are shown in Appendix B. The peak pressure, shock speed, and the particle velocity

decrease as the shock front advances along the axis of symmetry. To find the strain rates the finite difference approximation which holds for small incremental distances, was used.

$$\begin{aligned}\dot{\epsilon} &= \frac{d\epsilon}{dt} \\ \dot{\epsilon} &= \frac{dU_P}{dZ} \\ \dot{\epsilon} &\approx \frac{\Delta U_P}{\Delta Z}\end{aligned}\tag{7.12}$$

Consideration of Strength Effects

In the previous sections hydrodynamic theory was applied to determine the initial impact Hugoniot values and effects of rarefaction, ignoring the effect of material strength. But when the peak pressure associated with the advancing shock front dropped down considerably, neglecting the strength effects is no longer justified. The effect of material strength is to attenuate the shock pressure more rapidly than a hydrodynamic analysis would predict. Riney et al. [87] suggested that the limit of validity of the hydrodynamic model lies between 0.04 and 0.3 megabars of shock pressure. Hence the strength effects are considered from the point where the peak pressure of the shock has decayed to 0.05, 0.10, 0.18, and 0.2 megabars in the lead, 1100 aluminum, 6061 aluminum alloy and mild steel targets respectively. The reason for this arrangement is based on the order of their strengths.

To consider the strength effects, the approach of Lee et al. [88] was adapted into the analysis. The attenuation of a shock wave due to unloading stresses behind it is governed by material characteristics prescribing the response to reduction of the compressive stress normal to the wave front following a large impulsive increase in that stress component. Plasticity theory determines an elastic unloading region during which the shear stresses are reversed in sign followed by plastic flow in recovery with strain increments opposite in sign to those generated in the shock wave. Considering the deformation to be the combination of isotropic compression due to the average hydrostatic pressure, and elastic-plastic distortion due to the stress deviator or shear stress influence, the compressive principal stresses by symmetry are $\bar{\sigma}_{zz}$, $\bar{\sigma}_{xx}$, $\bar{\sigma}_{yy}$. Z is the cartesian coordinate normal to the plane wave surface as shown in Figure 7.1b. Since no lateral motion occurs, the principal engineering strain components are; \bar{e}_{zz} , 0, 0.

$$\bar{e}_{zz} = \frac{v_0 - v}{v_0}$$

$$\bar{e}_{zz} = 1 - (\rho_0/\rho) \quad (7.13)$$

where v and ρ refer to specific volume and density and suffix 0 refers to undeformed state.

For stress and strain increments $\Delta \bar{\sigma}_{zz}$ and $\Delta \bar{e}_{zz}$ following

the passage of the shock wave, the compressibility relation governing the averaged normal stress and dilatation takes the form

$$(\Delta \bar{\sigma}_{zz} + 2 \Delta \bar{\sigma}_{yy}) = 3k_s \Delta \bar{e}_{zz} \quad (7.14)$$

where k_s is the gradient of the pressure-compression isentrope.

Since the hydrostatic part of the stress tensor is dominating and assuming this to have minor influence on the deviator stress-strain relations governed by the elastic-plastic laws, we shall assume elastic-ideally plastic behavior, with the yield stress Y_0 in simple tension. The stress tensors are:

$$\begin{bmatrix} \bar{\sigma}_{yy} & 0 & 0 \\ 0 & \bar{\sigma}_{yy} & 0 \\ 0 & 0 & \bar{\sigma}_{zz} \end{bmatrix} = \begin{bmatrix} \frac{\bar{\sigma}_{yy} - \bar{\sigma}_{zz}}{3} & 0 & 0 \\ 0 & \frac{\bar{\sigma}_{yy} - \bar{\sigma}_{zz}}{3} & 0 \\ 0 & 0 & \frac{2(\bar{\sigma}_{zz} - \bar{\sigma}_{yy})}{3} \end{bmatrix} + \begin{bmatrix} \frac{2\bar{\sigma}_{yy} + \bar{\sigma}_{zz}}{3} & 0 & 0 \\ 0 & \frac{2\bar{\sigma}_{yy} + \bar{\sigma}_{zz}}{3} & 0 \\ 0 & 0 & \frac{2\bar{\sigma}_{yy} + \bar{\sigma}_{zz}}{3} \end{bmatrix}$$

From the results of Appendix A, J_2' and J_3' can be written as;

$$J_2' = \frac{1}{3} (\bar{\sigma}_{yy}^2 + \bar{\sigma}_{zz}^2) - \frac{2}{3} (\bar{\sigma}_{yy} \bar{\sigma}_{zz})$$

$$J_3' = \frac{2}{27} (\bar{\sigma}_{zz}^3 - \bar{\sigma}_{yy}^3 + 3 \bar{\sigma}_{yy}^2 \bar{\sigma}_{zz} - 3 \bar{\sigma}_{yy} \bar{\sigma}_{zz}^2)$$

Applying the proposed yield criterion as given by equation (4.9),

one gets;

$$\frac{1}{3} (\bar{\sigma}_{yy}^2 + \bar{\sigma}_{zz}^2) - \frac{2}{3} (\bar{\sigma}_{yy} \bar{\sigma}_{zz}) - 0.13 \left\{ \frac{2}{27} (\bar{\sigma}_{zz}^3 - \bar{\sigma}_{yy}^3 + 3 \bar{\sigma}_{yy}^2 \bar{\sigma}_{zz} - 3 \bar{\sigma}_{yy} \bar{\sigma}_{zz}^2) \right\}^{2/3} = \frac{Y_o^2}{3} - 0.13 \left(\frac{2}{27} Y_o^3 \right)^{2/3}$$

$$\frac{1}{3} (\bar{\sigma}_{yy} - \bar{\sigma}_{zz})^2 - 0.13 \left\{ \frac{2}{27} (\bar{\sigma}_{zz} - \bar{\sigma}_{yy})^3 \right\}^{2/3} = \frac{Y_o^2}{3} - 0.13 \left(\frac{2}{27} Y_o^3 \right)^{2/3}$$

$$(\bar{\sigma}_{yy} - \bar{\sigma}_{zz})^2 \left\{ \frac{1}{3} - 0.13 \left(\frac{2}{27} \right)^{2/3} \right\} = Y_o^2 \left\{ \frac{1}{3} - 0.13 \left(\frac{2}{27} \right)^{2/3} \right\}$$

$$|\bar{\sigma}_{yy} - \bar{\sigma}_{zz}| = Y_o \quad (7.15)$$

$$3p = (\bar{\sigma}_{zz} + 2 \bar{\sigma}_{yy})$$

$$\bar{\sigma}_{zz} = p + \frac{2}{3} Y_o$$

if plastic flow is occurring in loading or unloading respectively.

Principal values of increment of natural strains are; $\frac{\Delta \bar{e}_{zz}}{(1-\bar{e}_{zz})}$, 0, 0.

For elastic unloading, incremental deviatoric stress and strain tensors are;

$$\begin{bmatrix} \frac{1}{3} (\bar{\sigma}_{yy} - \bar{\sigma}_{zz}) & 0 & 0 \\ 0 & \frac{1}{3} (\bar{\sigma}_{yy} - \bar{\sigma}_{zz}) & 0 \\ 0 & 0 & \frac{2}{3} (\bar{\sigma}_{zz} - \bar{\sigma}_{yy}) \end{bmatrix} = 2 \mu \begin{bmatrix} -\frac{1}{3} \frac{\Delta \bar{e}_{zz}}{(1-\bar{e}_{zz})} & 0 & 0 \\ 0 & -\frac{1}{3} \frac{\Delta \bar{e}_{zz}}{(1-\bar{e}_{zz})} & 0 \\ 0 & 0 & \frac{2}{3} \frac{\Delta \bar{e}_{zz}}{(1-\bar{e}_{zz})} \end{bmatrix}$$

$$\frac{2}{3} (\bar{\sigma}_{zz} - \bar{\sigma}_{yy}) = 2 \mu \left\{ \frac{2}{3(1-\bar{e}_{zz})} \frac{\Delta \bar{e}_{zz}}{(1-\bar{e}_{zz})} \right\}$$

$$(\bar{\sigma}_{zz} - \bar{\sigma}_{yy}) = 2 \mu \frac{\Delta \bar{e}_{zz}}{(1 - \bar{e}_{zz})} \quad (7.16)$$

From equations (7.14) and (7.16) it follows that

$$\frac{\Delta \bar{\sigma}_{zz}}{\Delta \bar{e}_{zz}} = k_s + \frac{4}{3} \frac{\mu}{(1 - \bar{e}_{zz})} \quad (7.17)$$

Equations (7.15) and (7.16) show that $\Delta \bar{e}_{zz} = -\frac{Y_o}{\mu} (1 - \bar{e}_{zz})$ to be the change from plastic flow in loading to plastic flow in unloading.

The corresponding stress reduction as given by equation (7.17) is

$$\Delta \bar{\sigma}_{zz} = -Y_o \left[\frac{4}{3} + \frac{k_s}{\mu} (1 - \bar{e}_{zz}) \right] \quad (7.18)$$

After the peak pressure of the shock wave has decayed to the value indicated earlier, the shock wave begins to enter into the region where the material strength effects need to be considered. Such a situation may be considered as the problem of a body with a plane surface subjected to a suddenly applied uniform pressure, monotonically decreasing in magnitude after the initial discontinuous rise. This in turn may be considered as a shock wave propagating into the body followed by a tail of continuously decreasing stress. This tail causes the shock wave to be attenuated because unloading waves from the tail overtake the shock and interact with it. With the appropriate modification of the initial conditions to the conditions prevailing at the point where strength effects are to be considered, the approach of Lee and Liu was utilized. It was

assumed that the shock wave velocity U_{st} remains almost constant.

The justification for this assumption may be noted from the

U_s -vs- U_p shock Hugoniot depicted in Figure 7.5. For small particle

velocities, the shock speed U_s approaches c_{oh} and the variation in

U_s itself is small. Letting t_m to be the time corresponding to the

initiation of the material strength effects, the characteristic

diagram for an attenuating shock wave is shown in Figure 7.6.

$$\text{Gradient of the elastic unloading line} = c_o = \sqrt{\left[k_s + \frac{4}{3} \frac{\mu}{(1-e_{zz})} \right] \frac{1}{\rho}} \quad (7.19)$$

Gradient of the characteristics for

$$\text{unloading in the compressible fluid case} = c_1 = \sqrt{\frac{k_s}{\rho}} \quad (7.20)$$

$$\text{Gradient of the chord of } p - U_p \text{ Hugoniot} = c_2 = \frac{p_m}{U_{pm}} \cdot \frac{1}{\rho} \quad (7.21)$$

Gradient of the elastic-plastic boundary $Bc = c_3$ is given by

$$c_1 - c_3 = \frac{(c_o - c_2)}{c_o^2 c_2} \frac{(c_o + c_3)}{(c_1 + c_3)} \frac{c_1^2 c_3}{1} \quad (7.22)$$

Shock speed U_{st} at t_m be equal to c_2'

To the surface $Z = Z_m$ a linearly decaying stress $\bar{\sigma}_t = A_3 - B_3 (t-t_m)$

is applied at $t = t_m$. At B the stress has fallen sufficiently to

initiate plastic flow in unloading, and the boundary BC separates

the elastic and plastic regions.

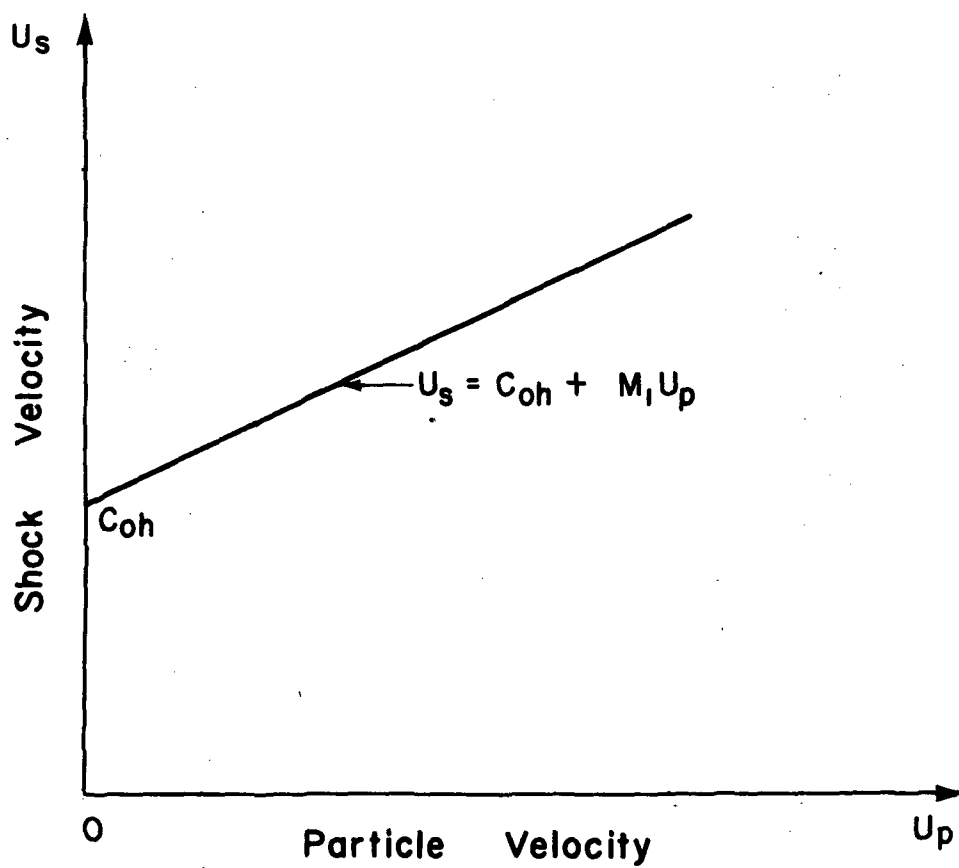


Fig. 7.5 Typical $U_s - U_p$ Shock Hugoniot

$$\bar{\sigma}_t = A_3 - B_3 (t - t_m) \quad (7.23)$$

The stresses at point on OA and BC in Figure 7.6 for the same position coordinate Z are related by

$$\bar{\sigma}_{OA} - \bar{\sigma}_{BC} = Y_o \left[\frac{4}{3} + k_s (1 - \bar{e}_{zz}) \frac{1}{\mu} \right] = 2Y \quad (7.24)$$

Where Y is dynamic stress under high pressure compression for a plate with lateral expansion prevented. Lee and Liu derived the following expressions for the stress immediately behind the shock front.

$$\bar{\sigma}_{zz}(t) = A_3 - B_3 \left(\frac{c_o^2 - c_2^2}{c_o} \right) \left(\frac{c_2'}{c_2 + c_2'} \right) (t - t_m) \quad (7.25)$$

$$\begin{aligned} \bar{\sigma}_{zz}(t) = A_3 - 2Y \left\{ \frac{c_2'(c_o + c_2)}{c_o(c_2 + c_2')} \right. \\ \left. - \frac{c_2'(c_o - c_2) [2c_2'c_3(c_o + c_2) + c_2(c_o - c_2')(c_o + c_3)]}{c_o c_2 (c_o - c_3) (c_o + c_2') (c_2 + c_2')} \right\} \\ - B_3 \frac{c_2'(c_o - c_2)^2 [2c_2'c_3(c_o + c_2) + c_2(c_o - c_2')c_o + c_3]}{c_o^2 c_2 (c_o - c_3) (c_o + c_2') (c_2 + c_2')} (t - t_m) \end{aligned} \quad (7.26)$$

Equation (7.25) is applicable for the attenuation of shock strength over the range OE, and thereafter the influence of plastic unloading will make itself felt and the equation (7.26) is applicable.

Tail of the Shock Wave

To determine the attenuation constants A_3 and B_3 in equation (7.23) one has to know the tail behind the shock wave at any instant of time. At the wave front the pressure increases sharply to its peak value and then decreases toward zero behind the shock front. The following notation refers to Figure 7.7.

Z = Distance normal to front relative to the shock front;

s is increasing in the negative Z direction.

c = sound velocity in the shocked state

c_0 = sound velocity in the initial state.

At $t = t_m$ the shock wave is OGF with its peak at position $Z = Z_m$. The shock front travels a distance ΔZ in time Δt and a point A which is at a pressure Δp below the peak and at a distance Δs behind the front travels a distance $\Delta s + \Delta Z$ in the same time. Thus the wave profile at time $t_m + \Delta t$ is QTR. Thus

$$\frac{\Delta Z}{U_s} = \frac{\Delta s + \Delta Z}{(U_p + c)} \quad (7.27)$$

The pressure gradient $\frac{\Delta p}{\Delta s}$ behind the shock front can be directly related to the rate of decay of the peak shock pressure $\frac{\Delta p}{\Delta Z}$ with travel distance as follows.

From the similar triangles OAS, and QB'W, we have from Figure 7.8;

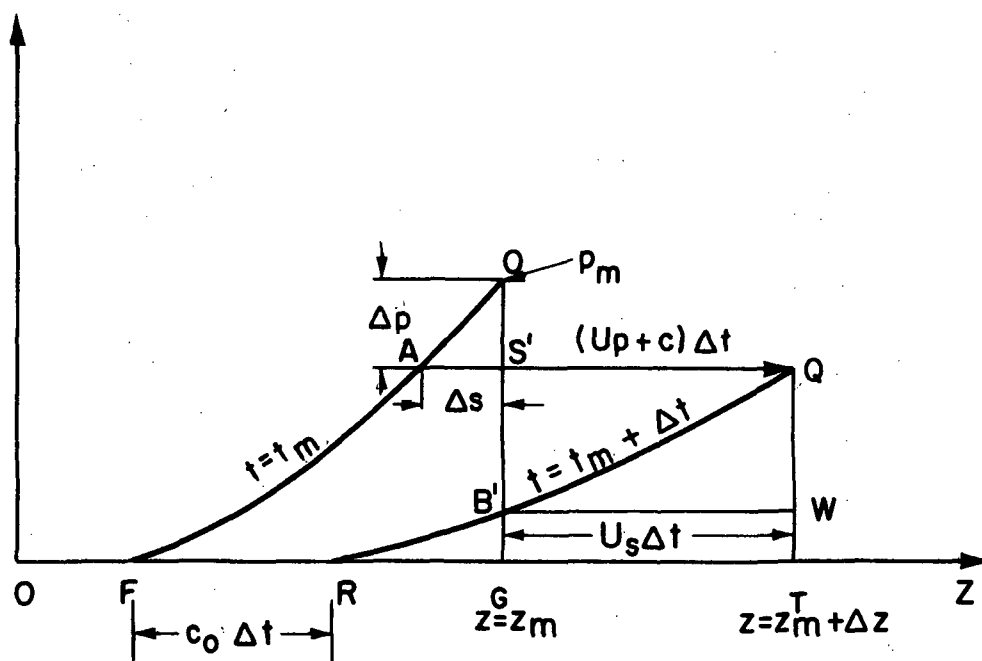


Fig. 7.7 Pressure Profile of a Plane Shock Wave at Two Successive Time Intervals

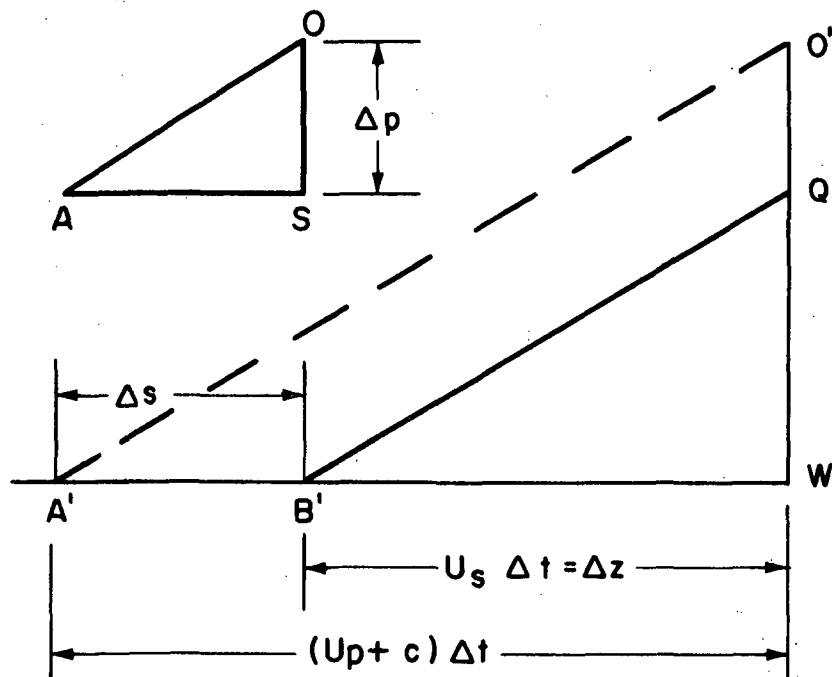


Fig. 7-8 Geometry to Determine the Tail of Shock

$$\frac{OS}{AS} = \frac{QW}{B'W}$$

$$QW = \frac{\Delta p}{\Delta s} U_s \Delta t \quad (7.28)$$

From the similar triangles O'A'W and OAS,

$$\frac{O'W}{A'W} = \frac{OS}{AS}$$

$$\frac{\Delta p + QW}{(U_p + c)\Delta t} = \frac{\Delta p}{\Delta s} \quad (7.29)$$

Substitution of QW from equation (7.28) into equation (7.29)

$$\frac{\Delta p + \frac{\Delta p}{\Delta s} U_s \Delta t}{(U_p + c)\Delta t} = \frac{\Delta p}{\Delta s} \quad (7.30)$$

$$\Delta s + \Delta Z = (U_p + c)\Delta t$$

$$\Delta Z = U_s \Delta t$$

$$\Delta s = (U_p + c) - U_s \Delta t$$

Equation (7.30) can be rewritten as;

$$\frac{\frac{\Delta p}{\Delta Z} U_s \Delta t + \frac{\Delta p}{\Delta s} U_s \Delta t}{(U_p + c)\Delta t} = \frac{\Delta p}{\Delta s}$$

$$\frac{\Delta p}{\Delta Z} + \frac{\Delta p}{\Delta s} \frac{U_s}{U_p + c} = \frac{\Delta p}{\Delta s}$$

$$\frac{\Delta p}{\Delta s} \left[1 - \frac{U_s}{(U_p + c)} \right] = \frac{\Delta p}{\Delta Z} \frac{U_s}{(U_p + c)}$$

$$\frac{\Delta p}{\Delta s} = \frac{\frac{\Delta p}{\Delta Z}}{\frac{(U + c)}{p} - 1} - 1 \quad (7.31)$$

$$\Delta s = \Delta Z \frac{(U + c)}{p} - 1 \quad (7.32)$$

Thus to generate the tail associated with a shock wave of a certain peak p located at position Z , different Δs were found corresponding to different travel distances ΔZ . That is the peak p_1 at position $Z + \Delta Z$ and the corresponding Δs_1 and the peak p_2 at position $Z + 2\Delta Z$ and the corresponding Δs_2 and so on. Then corresponding to $\Delta s_1, \Delta s_2, \dots$ measured backwards from position Z , the values p_1, p_2, \dots were plotted. In this way the tail associated with any shock wave of certain peak can be generated as shown in Figure 7.9. Thus the most obvious changes that occur in a shock wave with the passage of time are the decay in peak pressure and spread of the tail.

Determination of the Attenuation Constants

The determination of the constants A_3 and B_3 in equation (7.23) is essential to determine the stress as given by equations (7.25 and 7.26) immediately behind the shock wave as it propagates through the regions where strength effects predominate. The stress $\bar{\sigma}_{zz}$ and the pressure p are related as follows.

$$\bar{\sigma}_{zz} = p - \frac{2}{3}Y ; A_3 = p_m - \frac{2}{3}Y \quad (7.33)$$

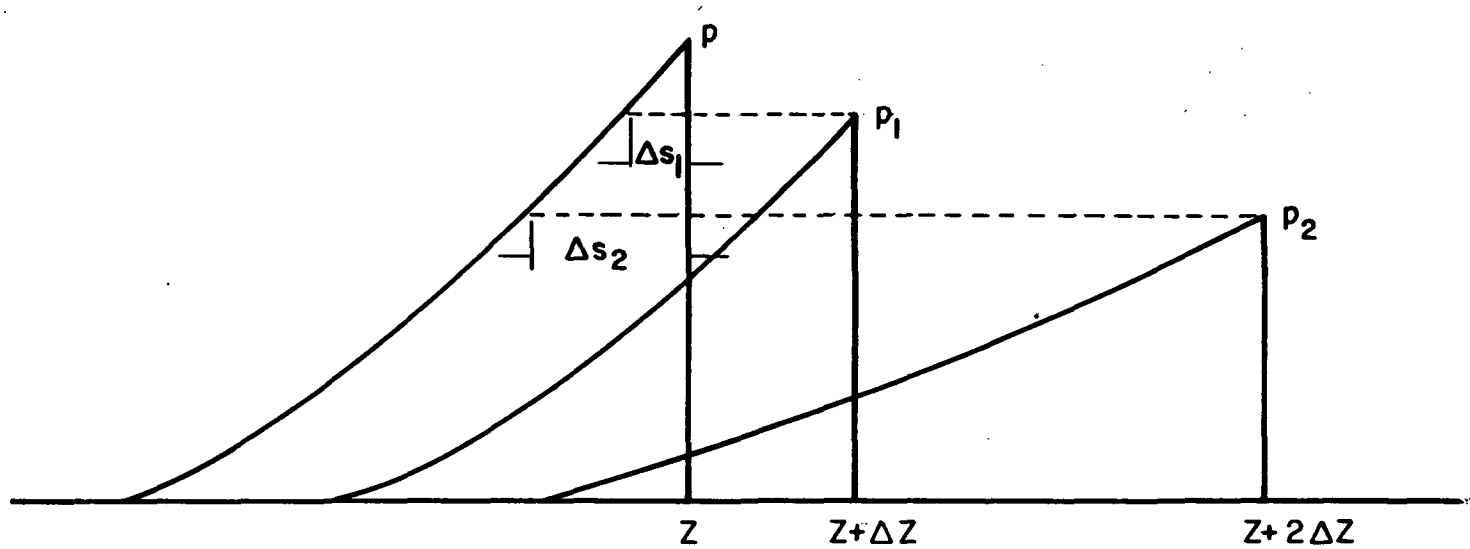


Fig. 7-9 Generation of the Tail behind the Shock Wave

To determine B_3 one has to know the stress corresponding to point B' at position $Z = Z_m$ as shown in Figure 7.7. In other words, the tail of the shock wave corresponding to time $t = t_m + \Delta t$ is to be generated. In Figure 7.6, the stress at O and stress at B differ by $2Y$. For an intermediate point such as B', the stress as obtained by determining the tail of the shock wave corresponding to $t = t_m + \Delta t$ can be found. Thus attenuation constant B_3 is given by

$$B_3 = \frac{\bar{\sigma}_O - \bar{\sigma}_{B'}}{\Delta t} \quad (7.34)$$

Strain Rates

The attenuation constants A_3 and B_3 being determined, the computation of strain rates in the region where material strength plays role may be done as follows. Now the particle velocity U_p cannot be taken from the Hugoniot properties. On the other hand it is computed as follows.

$$U_p = \frac{\bar{\sigma}_{zz}}{\rho U_{st}} = \frac{\bar{\sigma}_{zz}}{\rho c_2'} \quad (7.35)$$

$\bar{\sigma}_{zz}$ is determined from equations (7.25) or (7.26) for different time increments.

$$\Delta Z = c_2' \Delta t \quad (7.36)$$

$$\dot{\epsilon} = \frac{\Delta U_p}{\Delta Z} \quad (7.37)$$

The strain rates determined this way as well as from equation (7.12) are tabulated in Appendix B for all the targets.

Discussion on Strain Rates

These calculations as outlined in the above sections were performed on each of the targets to obtain the initial Hugoniot values, strain rates in the region affected by rarefactions from the periphery of the projectile calculated from hydrodynamic considerations, and strain rates during the late stages when the material strength effects come into play. These strain rates along the axis of symmetry are listed in Appendix B. Appendix B also shows a sample calculation for determining the strain rates. Representative values of strain rates for the various target-projectile combinations are shown in Table 7.2.

From the results of Appendix B it may be observed that for any given impact case the strain rates decrease in the regions affected by rarefaction with an abrupt rise where strength effects are introduced and increase from there on. The abrupt rise is due to the introduction of a new effect. The later increase in strain rates is due to the more rapid attenuation of the shock pressure caused by material strength effects. This also reflects in particle velocity. For a given target-projectile material combination, the effects of projectile size and velocity on strain rates are the same in hydrodynamic as well as material strength dominant region. That is a projectile of smaller size or of a higher velocity produces a higher strain rate. A faster projectile causes a larger rate of deformation and hence a higher strain rate.

Table 7.2 Representative Values of Strain Rates
Along the Axis of Symmetry

Shot Number	Target Material	Projectile		Strain rate $\dot{\epsilon} \times 10^{-6} \text{ sec.}^{-1}$	
		d_p cm.	V_p Km/sec.	Hydrodynamic regime	Material Strength regime
6-106	1100 Al.	0.159	5.58	1.13	1.48
6-117	"	0.100	5.59	1.79	1.58
6-161	"	0.159	8.30	2.00	5.09
6-162	"	0.159	8.33	2.01	5.11
6-108	6061 Al. alloy	0.159	5.60	1.37	1.96
6-124	"	0.100	6.14	1.89	2.11
6-147	"	0.040	6.03	4.48	4.02
6-111	Mild steel	0.159	5.62	0.57	0.36
6-146	"	0.100	6.13	1.40	0.68
6-109	Lead	0.159	5.27	0.81	0.28
6-127	"	0.100	6.12	1.52	1.65

A smaller projectile producing a higher strain rate than a larger projectile at the same velocity may be noted for example by comparing targets 6-106 and 6-117 of Table 7.2. In other words for the same time increment, the change in strain is more with a

$$\text{Ratio of projectile diameters} = \frac{dp_1}{dp_2} = \frac{0.15875}{0.1} = 1.5875$$

$$\text{Ratio of strain rates} = \frac{\dot{\epsilon}_2}{\dot{\epsilon}_1} = \frac{1.58 \times 10^6}{1.48 \times 10^6} = 1.07$$

smaller projectile. Similar kinds of nonlinear scaling effects were also observed by other workers with reference to crater depth and front surface ejecta momentum.

Thus the determination of strain rates and the development of the strain rate sensitive constitutive equation will enable one to obtain dynamic strength. This strength can be used in the penetration equations to predict the target damage.

CHAPTER VIII

PREDICTION OF CRATER DEPTHS

Derivation of Penetration Equation

Spacecraft are normally designed to withstand the hazards of the meteoroid environment which exists in space. The design of appropriate shielding is based on penetration equations developed from observed cratering phenomena in semi-infinite targets. Thus an appropriate penetration equation which includes the essential features of the problem is needed for predicting the crater depths produced by projectiles impacting at hypervelocities. Several types of penetration equations developed from partly theoretical and partly practical considerations were listed by Cour-Palais [89], and Wenzel et al. [46]. In the present consideration the General Motors penetration equation was used. This penetration equation with slight modification may be developed as follows. It was generally observed from the impact of hypervelocity projectiles that the volume of crater v_c is directly proportional to the density ρ_{op} and the kinetic energy E_p of the impacting projectile and inversely proportional to the density ρ_{ot} and some kind of strength S_t of the target material.

$$v_c \propto \frac{\rho_{op}}{\rho_{ot}} \frac{E_p}{S_t}$$

But

$$E_p = \frac{1}{2} \left[\rho_{op} \frac{4}{3} \pi \left(\frac{dp}{2} \right)^3 \right] v_p^2$$

$$E_p \propto \rho_{op} v_p^2 d_p^3$$

$$v_c \propto \frac{\rho_{op}^2}{\rho_{ot}} \frac{v_p^2}{S_t} d_p^3 \quad (8.1)$$

Now, the crater depth P_c is given by

$$P_c \propto v_c^{1/3}$$

$$P_c = K_6 d_p^{2/3} \rho_{op}^{-1/3} \rho_{ot}^{2/3} v_p^{2/3} S_t^{-1/3} \quad (8.2)$$

where K_6 is a constant.

Wenzel et al. found that the hardness of the target measured after impact or the dynamic hardness to be a better correlating parameter and specified the General Motors penetration equation as follows:

$$P_c = K_5 d_p^{2/3} \rho_{op}^{-1/3} \rho_{ot}^{2/3} v_p^{2/3} B_{t \max}^{-1/3}$$

Even though this equation gives crater depths very close to the experimental values, the use of this equation for prediction purposes is limited because the target hardness in the above equation can only be obtained after actually damaging the target.

Also it has been apparent for some time that hand book values of yield stress or ultimate stress are inappropriate since they are obtained at relatively low rates of strain. Hence it is felt that the dynamic strength of the target, obtained from theoretical considerations for any particular impact case, may be used in the penetration equations for prediction purposes. Then the question arises immediately as to strength corresponding to what strain and strain rate should be used. Placesi et al. [34], based on their impact experiments on targets of different materials and at different temperatures, concluded that the tensile and compressive yield strength are effective mechanical strength properties and that the ultimate tensile strength and microhardness are not effective properties in determining the final crater dimensions. Guided by this conclusion and feeling that it is reasonable to use the strain rates in the region where material strength effects come into play, the corresponding dynamic yield strength was used as a parameter in the penetration equation as follows:

$$P_c = K_4 d_p \rho_{op}^{2/3} \rho_{ot}^{-1/3} V_p^{2/3} (\sigma_{dyn-yd})^{-1/3} \quad (8.3)$$

Determination of Dynamic Yield Strength

One of the significant variables which must thus be known in order to predict the size of the crater formed is the dynamic yield strength of the target material. The following procedure was

adopted to determine $\sigma_{\text{dyn-yd}}$ associated with equation (8.3). From the quasi-static and dynamic response of the materials used in the hypervelocity experimentation and from the constitutive equation developed in the earlier chapter and given by equation (5.9), the stress-strain curves for the plastic portion corresponding to strain rates in the region where material strength effects come into play can be obtained. Then the elastic modulus line was extended to intersect the above stress strain curve thus locating the dynamic yield strength of the material (Figure 8.1). This yield strength was used in the penetration equation (8.3).

Prediction of Crater Depths

Equation (8.3) with the appropriate units may be rewritten as follows:

$$P_c = K_4 d_p \rho_{op}^{2/3} \rho_{ot}^{-1/3} v_p^{2/3} (\sigma_{\text{dyn-yd}})^{-1/3}$$

where

P_c = Crater depth in cms.

K_4 = a constant

ρ_{op} = Undisturbed density of the projectile in gms/cm^3 .

ρ_{ot} = Undisturbed density of the target in gms/cm^3 .

v_p = Velocity of the projectile in km/sec.

$\sigma_{\text{dyn-yd}}$ = Dynamic yield strength of the target material in kg/cm^2 .

To determine that constant K_4 a log-log plot of $\sigma_{\text{dyn-yd}}$ as

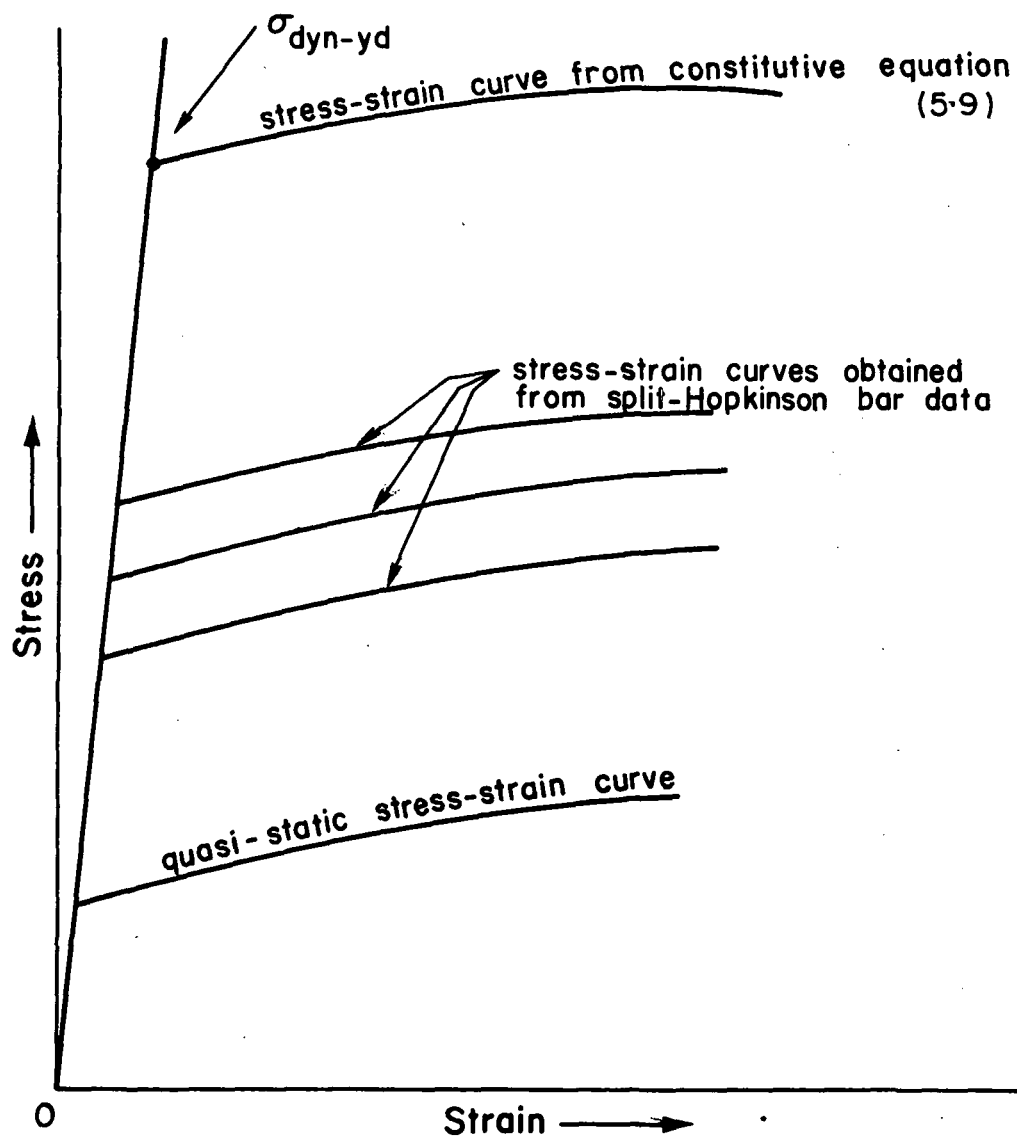


Fig. 8-1 Determination of Dynamic Yield Strength

abscissa and $P_c d_p \rho_{op}^{2/3} \rho_{ot}^{-1/3} V_p^{2/3}$ as ordinate was drawn as shown in Figure 8.2. A straight line with negative one third slope and K_4 as 7.992 fitted the experimental data when the above units are used for the variables.

The experimental and predicted crater depths and the percentage errors are listed in Table 8.1. The quasi-static and dynamic response of the materials were shown in Figures 6.1 to 6.4. (p. 40-43)

Discussion of Results

Figure 8.2 shows the comparison between the experimental and predicted crater depths. The log-log plot as shown in this figure also indicates a negative one third power for the dynamic yield strength as used in the penetration equation (8.3). The disposition of the experimental points as compared with the theoretically estimated crater depths may be noted. The deviation of lead targets from the theory may also be observed in the above figure.

It may be noted from Table 8.1 and Figure 8.2 that good agreement exists between the theory and experiment. The error is within 5% for 1100 aluminum, 6061 aluminum alloy, and mild steel targets. However the magnitude of error was about 14% in the case of lead targets. Such errors may be attributed to some of the uncertainties and approximations involved in deriving the stress strain curves at strain rates of at least two orders of magnitude

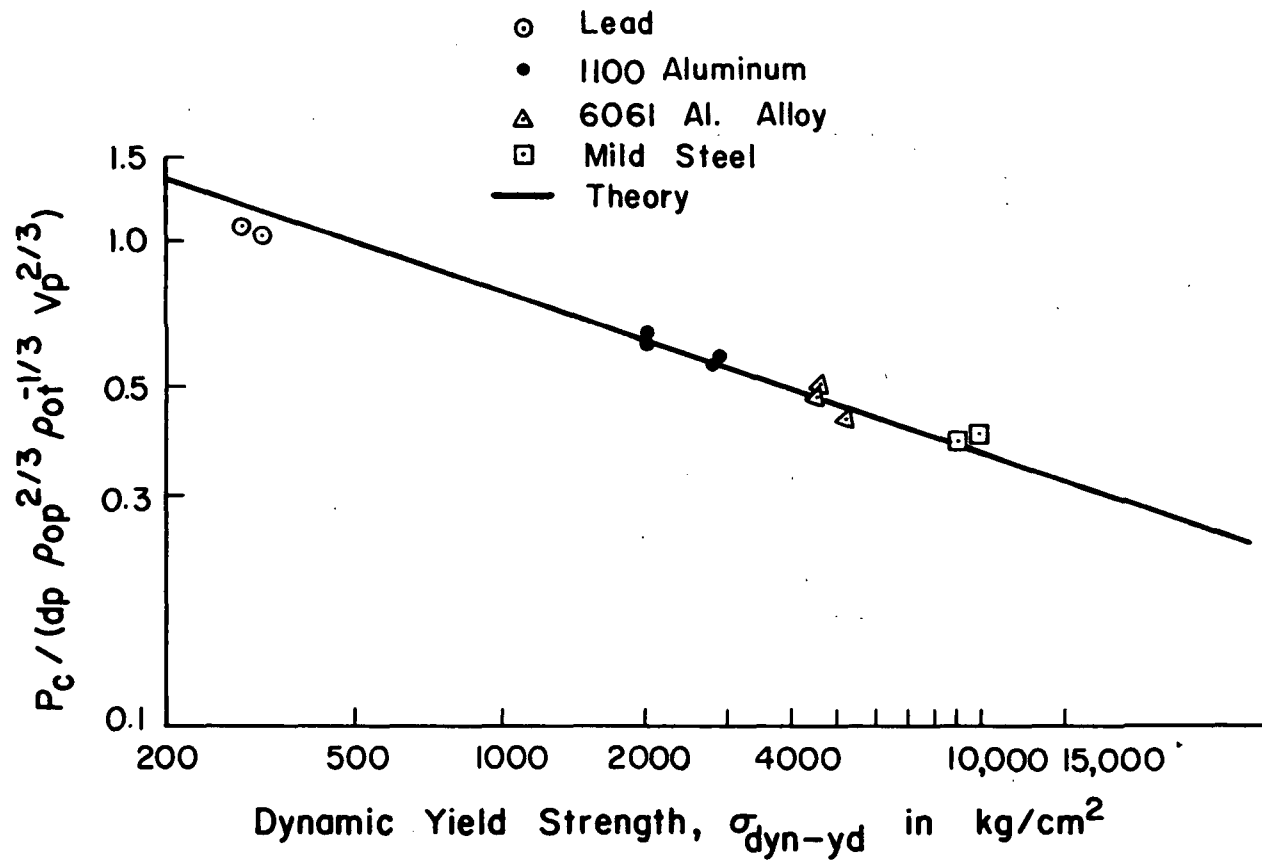


Fig. 8.2 Comparison of Theoretical and Experimental Crater Depths

Table 8.1 Theoretical and Experimental Crater Depths

$$P_c = 7.992 d_p^{2/3} \rho_{op}^{-1/3} V_p^{2/3} (\sigma_{dyn-yd})^{-1/3} ; \text{Projectile Material: Pyrex Density: } 2.23 \text{ gm/cm}^3$$

Shot Number	Material	Density ρ_{ot} , gm/cm ³	Target	Diameter d_p , cm	Velocity V_p , km/sec	Crater Depth, P_c	Theoretical Crater Depth, P_c	Error %
6-106	1100 Al.	2.785		0.15875	5.58	0.3937	0.3818	3.02
6-117	"	"		0.10000	5.59	0.2400	0.2400	0.00
6-161	"	"		0.15875	8.33	0.4440	0.4480	0.89
6-162	"	"		0.15875	8.30	0.4430	0.4477	1.06
6-108	6061 Al. alloy	2.785		0.15875	5.60	0.2890	0.2898	0.27
6-124	"	"		0.10000	6.14	0.2004	0.1930	3.69
6-147	"	"		0.03969	6.03	0.0695	0.0729	4.94
6-111	Mild steel	7.850		0.15875	5.62	0.1640	0.1641	0.05
6-146	"	"		0.10000	6.13	0.1102	0.1065	3.33
*	"	"		0.31750	30.00	*	0.9404	*
*	"	"		0.03969	30.00	*	0.1136	*
6-109	Lead	11.340		0.15875	5.27	0.3914	0.4449	13.66
6-127	"	"		0.10000	6.12	0.2590	0.2947	13.79

* Experiments were not performed on these targets.

higher than those attainable by any present day laboratory testing devices. For example there are uncertainties associated with the gage factor under dynamic conditions of the strain gages used in the split Hopkinson pressure bar apparatus. Also certain approximations are involved with the averaging technique employed while reducing the split Hopkinson bar data. Consequently these affect the constants characterizing the material and hence the constitutive equation. It may also be noted at this stage that the response of lead was fairly complex in quasi-static as well as in dynamic tests because of its soft nature. The deformation of the specimen was irregular resulting in loss of symmetry. Also the specimen was extremely hot immediately after dynamic testing. Phenomena such as heat conduction and other thermal effects due to material heating, liquefaction and vaporization were not considered in the present work and they further compound the complexity of the hypervelocity impact problem.

In spite of the above uncertainties and approximations, equation (8.3) may be used for prediction purposes without actually damaging the target once the dynamic yield strength for any particular impact case is determined. From practical considerations the error resulting from the application of equation (8.3) is tolerable. The evaluation of dynamic yield strength consists of the calculation of strain rates encountered in the particular impact case and the use of a constitutive equation.

CHAPTER IX

SUMMARY AND CONCLUSIONS

The third invariant of the stress deviator was incorporated into the quasi-static yield criterion and its validity was tested with reference to the available two and three dimensional experimental data. Using this yield criterion, a strain rate sensitive constitutive equation was developed. The six constants which characterize the material and which are associated with the constitutive equation were determined from the quasi-static and dynamic response of the material. Certain simplifying assumptions were made in regard to the plane nature of the advancing shock front in a semi-infinite target impacted by a spherically shaped and normally incident pyrex projectile at hypervelocities. This enabled the determination of strain rates associated with such impacts. The initial hydrodynamic regime and the subsequent material strength affected regime were taken into account for such a computation. The consideration was limited to the vicinity of the axis of symmetry. Corresponding to the strain rates prevailing in the material strength affected regime of any particular impact case, the dynamic yield strength of the target material was estimated utilizing the constitutive equation. This dynamic yield strength was adapted into the General Motors penetration equation and the crater depths were predicted. Based on this study, the following

conclusions were drawn.

1. Incorporation of the third invariant of the deviatoric stress tensor into the yield criterion, though not differing very significantly from the widely used von Mises criterion, developed a trend which brought the theory closer to the experimental results.
2. The applicability of the developed strain rate sensitive constitutive equation was verified by hypervelocity impact experiments.
3. The dynamic yield strength of the target material was found to be an important correlating parameter in predicting the crater depths.
4. The crater depths that result from the hypervelocity impact of spherically shaped and normally incident projectiles on semi-infinite metal targets were predicted using the General Motors penetration equation with an appropriate modification in regard to the hardness of target after impact. Good agreement with an error of less than 5% except in the case of lead targets was found to be existing between the theory and experiment.

From the study reported in this work, it is felt that further investigation needs to be pursued in the following directions for the analysis of the problem. The thermal effects and three dimensional considerations need to be included into the problem. Even though this study streamlined a procedure to determine the

strain rates and established the importance of the dynamic yield strength, there exists some kind of uncertainty in regard to the exact place where material strength effects are to be introduced. Even though it is known that the material strength effects come into play when the peak pressure of the advancing shock front is 0.04 to 0.3 megabars, such a range might be a function of the projectile velocity besides the nature of the target material. This needs a much more elaborate theoretical and experimental investigation.

REFERENCES

- 1 Christman, D. R., and Gehring, J. W., "Analysis of High-Velocity Projectile Penetration Mechanics," J. Appl. Phys., Vol. 37, No. 4, 1966, pp. 1579-1587.
- 2 Kineke, J. H., Jr., "Observations of Crater Formation in Ductile Materials," Proc. of the 5th Symp. on Hypervelocity Impact, Vol. 1, Part 2, 1962, pp. 339-370.
- 3 Pond, R. B., Mobley, C., and Glass, C. M., "Energy Balances in Hypervelocity Penetration," Proc. of the 6th Symp. on Hypervelocity Impact, Vol. 2, Part 2, 1963, pp. 401-417.
- 4 Rae, W. J., and Kirchner, H. P., "A Blast Wave Theory of Crater Formation in Semi-infinite Targets," Proc. of the 6th Symp. on Hypervelocity Impact, Vol. 2, Part 1, 1963, pp. 163-227.
- 5 Davids, N., and Calvit, H. H., "Some Dynamical Applications of Shock Wave Propagation in Solids," Stress Waves in Anelastic Solids, Ed. Kolsky, H., and Prager, W., IUTAM Symposium, Springer-Verlag, 1964, pp. 1-19.
- 6 Davids, N., and Hwang, Y. K., "Shock Waves in Solid Craters," J. Aerosp. Sci., Vol. 29, No. 5, 1962, pp. 550-557.
- 7 Davids, N., and Mehta, P. K., "Spherical Elasto-Plastic Waves in Materials," Behavior of Materials Under Dynamic Loading, Ed. Huffington, N. J., Jr., ASME, N. Y., 1965, pp. 125-137.
- 8 Hwang, S. Y., and Davids, N., "Graphical Analysis of the Formation of Shock Fronts in Materials," J. Mech. Phys. Solids, Vol. 8, No. 1, 1960, pp. 52-65.
- 9 Kinslow, R., "Properties of Spherical Shock Waves Produced by Hypervelocity Impact," Proc. of the 6th Symp. on Hypervelocity Impact, Vol. 2, Part 1, 1963, pp. 273-320.
- 10 Eichelberger, R. J., and Gehring, J. W., "Effects of Meteoroid Impacts on Space Vehicles," American Rocket Society Journal, Vol. 32, No. 10, 1962, pp. 1583-1591.

- 11 Gehring, J. W., Meyers, C. L., and Charest, J. A., "Experimental Studies of Impact Phenomena and Correlation With Theoretical Models," Proc. of the 7th Hypervelocity Impact Symp., Vol. 5, 1965, pp. 161-211.
- 12 Bjork, R. L., "Review of Physical Processes in Hypervelocity Impact and Penetration," Proc. of the 6th Symp. on Hypervelocity Impact, Vol. 2, Part 1, 1963, pp. 1-58.
- 13 Marnell, P., Soifer, M., and Zaid, M., "Hypervelocity Impact - A Series Solution," Proc of the 7th Hypervelocity Impact Symp., Vol. 3, 1965, pp. 151-213.
- 14 Luttrell, J. L., "A Hypervelocity Impact Model for Completely Deforming Projectiles," Proc. of the 6th Symp. on Hypervelocity Impact, Vol. 2, Part 1, 1963, pp. 157-161.
- 15 Wagner, M. H., Brooks, N. B., and Bjork, R. L., "Impact of a Porous Aluminum Projectile on Aluminum at 20 and 72 km/sec.," Proc. of the 7th Hypervelocity Impact Symp., Vol. 3, 1965, pp. 1-54.
- 16 Heyda, J. F., and Riney, T. D., "Peak Axial Pressures in Semi-infinite Media Under Hypervelocity Impact," Proc. of the 7th Hypervelocity Impact Symp., Vol. 3, 1965, pp. 75-122.
- 17 Rice, M. H., McQueen, R. G., and Walsh, J. M., "Compression of Solids by Strong Shock Waves," Solid State Physics, Vol. 6, 1958, pp. 1-63.
- 18 Walsh, J. M., and Christian, R. H., "Equation of State of Metals From Shock Wave Measurements," Physical Review, Vol. 97, No. 6, 1955, pp. 1544-1556.
- 19 Walsh, J. M., Rice, M. H., McQueen, R. G., and Yarger, F. L., "Shock-Wave Compressions of Twenty-Seven Metals, Equations of State of Metals," Physical Review, Vol. 108, No. 2, 1957, pp. 196-216.
- 20 Doran, D. G., and Linde, R. K., "Shock Effects in Solids," Solid State Physics, Vol. 19, 1966, pp. 229-290.
- 21 McQueen, R. G., and Marsh, S. P., "Equations of State for Nineteen Metallic Elements from Shock Wave Measurements to Two Megabars," J. Appl. Phys., Vol. 31, No. 7, 1960, pp. 1253-1269.

- 22 Al'tshuler, L. V., Krupnikov, K. K., and Brazhnik, M. I., "Dynamic Compressibility of Metals Under Pressures from 400,000 to 4,000,000 Atmospheres," Soviet Physics JETP (English Transl.), Vol. 7, No. 4, 1958, pp. 614-619.
- 23 Al'tshuler, L. V., Kormer, S. B., Bakanova, A. A., and Trunin, R. F., "Equations of State for Aluminum, Copper, and Lead in the High Pressure Region," Soviet Physics JETP (English Transl.), Vol. 11, No. 3, 1960, pp. 573-579.
- 24 Al'tshuler, L. V., Kormer, S. B., Brazhnik, M. I., Vladimirov, L. A., and Sperskaya, M. P., "The Isentropic Compressibility of Aluminium, Copper, Lead, and Iron at High Pressures," Soviet Physics JETP (English Transl.), Vol. 11, No. 4, 1960, pp. 766-775.
- 25 Lindholm, U. S., "Some Experiments in Dynamic Plasticity Under Combined Stress," Mechanical Behavior of Materials Under Dynamic Loads, Ed. Lindholm, U. S., Springer-Verlag, New York Inc., 1968, pp. 77-95.
- 26 Boa-Teh, C., "Response of Various Material Media to High-Velocity Loading," J. Mech. Phys. Solids, Vol. 13, No. 3, 1965, pp. 165-187.
- 27 Chiu, S. S., and Neubert, V. H., "Difference Method for Wave Analysis of the Split Hopkinson Pressure Bar With a Viscoelastic Specimen," J. Mech. Phys. Solids, Vol. 15, No. 3, 1967, pp. 177-193.
- 28 Nevill, G. E., Jr., and Myers, C. D., "Strain-Rate Effects During Reversed Loading," J. Mech. Phys. Solids, Vol. 16, No. 3, 1968, pp. 187-194.
- 29 Davids, N., Minnich, R., and Sliney, J., "A Penetration Method for Determining Impact Yield Strength," Proc. of the 7th Hypervelocity Impact Symp., Vol. 3, 1965, pp. 261-297.
- 30 Rolsten, R. F., and Hunt, H. H., "Dynamic Stress at Hypervelocity Impact and True Tensile Strength," Canadian Aeronautics and Space Journal, Vol., 13, No. 6, 1967, pp. 269-272.
- 31 Chou, P. C., and Burns, B. P., "Late-Stage Equivalence in One-Dimensional Impacts," J. Appl. Phys., Vol. 38, No. 2, 1967, pp. 553-560.
- 32 Riney, T. D., "Visco-Plastic Solution of Hypervelocity Impact Cratering Phenomenon," Proc. of the 6th Symp. on Hypervelocity Impact, Vol. 2, Part 1, 1963, pp. 105-161.

- 33 Dunn, W. P., "On Material Strengths of the Hypervelocity Impact Problem," AIAA Journal, Vol. 5, No. 3, 1966, pp. 535-536.
- 34 Placesi, R., Waser, R. H., and Dawson, V. C. D., "Determination of Yield Strength as an Effective Mechanical Strength Property in the Cratering Process of Hypervelocity Impact," Proc. of the 7th Hypervelocity Impact Symp., Vol. 5, 1965, pp. 259-272.
- 35 Bjork, R. L., "Analysis of the Formation of Meteor Crater, Arizona," Journal of Geophysical Research, Vol. 66, No. 10, 1961, pp. 3379-3387.
- 36 Olshaker, A. E., and Bjork, R. L., "Hydrodynamics Applied to Hypervelocity Impact," Proc. of the 5th Symp. on Hypervelocity Impact, Vol. 1, Part 1, 1962, pp. 185-240.
- 37 Walsh, J. M., and Tillotson, J. H., "Hydrodynamics of Hypervelocity Impact," Proc. of the 6th Symp. on Hypervelocity Impact, Vol. 2, Part 1, 1963, pp. 59-104.
- 38 Rinehart, J. S., and White, W. C., "Shapes of Craters Formed in Plaster of Paris by Ultra Speed Pellets," American Journal of Physics, Vol. 20, No. 1, 1952, pp. 14-18.
- 39 Wilkins, M. L., "Calculation of Elastic-Plastic Flow," Methods of Computational Physics, Ed. Alder, B., Fernbach, S., and Rotenberg, M., Academic Press, New York, Vol. 3, 1964, pp. 211-263.
- 40 Wilkins, M. L., and Giroux, R., "The Calculation of Stress Waves in Solids," Proc. of the 6th Symp. on Hypervelocity Impact, Vol. 2, Part 1, 1963, pp. 141-155.
- 41 Riney, T. D., "Behavior of Metals During Hypervelocity Impact Cratering," Proc. of the 8th Midwestern Mechanics Conference, Vol. 2, Part 2, 1963, pp. 419-445.
- 42 Riney, T. D., "Depth of Penetration of Hypervelocity Projectiles," AIAA Journal, Vol. 3, No. 1, 1965, pp. 52-60.
- 43 MacCormack, R. W., "The Effect of Viscosity in Hypervelocity Impact Cratering," AIAA Hypervelocity Impact Conference, AIAA Paper No. 69-354, 1969.
- 44 Kraus, H., "Two-Dimensional Analysis of a Hypervelocity Impact Upon a Visco-Plastic Plate," Proc. of the 6th Symp. on Hypervelocity Impact, Vol. 3, 1963, pp. 13-40.

- 45 Chou, P. C., "Visco-Plastic Flow Theory in Hypervelocity Perforation of Plates," Proc. of the 5th Symp. on Hypervelocity Impact, Vol. 1, Part 1, 1962, pp. 307-328.
- 46 Wenzel, A. B., and Gehring, J. W., "Hypervelocity Impact Studies Against Apollo-Type Structures Up to 16.5 km/sec.," Final Report to North American Aviation on M4S8 x A - 4060333, TR 65-56, July 1965.
- 47 Herrmann, W., and Jones, A. H., "Correlation of Hypervelocity Impact Data," Proc. of the 5th Symp. on Hypervelocity Impact, Vol. 1, Part 2, 1962, pp. 389-438.
- 48 Engel, O. G., "Hypervelocity Cratering Data and a Crater-Depth Model for the Regime of Partial Fluidity," Proc. of the 6th Symp. on Hypervelocity Impact, Vol. 2, Part 2, 1963, pp. 337-366.
- 49 Bruce, E. P., "Review and Analysis of High Velocity Impact Data," Proc. of the 5th Symp. on Hypervelocity Impact, Vol. 1, Part 2, 1962, pp. 439-473.
- 50 Sawle, D. R., "Hypervelocity Impact in Thin Sheets and Semi-infinite Targets at 15 km/sec.," AIAA Journal, Vol. 8, No. 7, 1970, oo. 1240-1244.
- 51 Prager, W., "On Higher Rates of Stress and Deformation," J. Mech. Phys. Solids, Vol. 10, 1962, pp. 133-138.
- 52 Bodner, S. R., "Strain-Rate Effects in Dynamic Loading of Structures," Behavior of Materials Under Dynamic Loading, Ed. Huffington, N. J., Jr., ASME, N. Y., 1965, pp. 93-105.
- 53 Davies, E. D. H., and Hunter, S. C., "The Dynamic Compression Testing of Solids by the Method of the Split Hopkinson Pressure Bar," J. Mech. Phys. Solids, Vol. 11, No. 3, 1963, pp. 155-179.
- 54 Lindholm, U. S., "Dynamic Deformation of Metals," Behavior of Materials Under Dynamic Loading, Ed. Huffington, N. J., Jr., ASME, N. Y., 1965, pp. 42-61.
- 55 Butcher, B. M., and Canon, J. R., "Influence of Work-Hardening on the Dynamic Stress-Strain Curves of 4340 Steel," AIAA Journal, Vol. 2, No. 12, 1964, pp. 2174-2179.
- 56 Marsh, K. J., and Campbell, J. D., "The Effect of Strain-rate on the Post-Yield Flow of Mild Steel," J. Mech. Phys. Solids, Vol. 11, No. 1, 1963, pp. 49-63.

- 57 Malvern, L. E., "Experimental Studies of Strain-Rate Effects and Plastic Wave Propagation in Annealed Aluminum," Behavior of Materials Under Dynamic Loading, Ed. Huffington, N. J., Jr., ASME, N. Y., 1965, pp. 81-92.
- 58 Wood, E. R., and Philips, A., "On the Theory of Plastic Wave Propagation in a Bar," J. Mech. Phys. Solids, Vol. 15, No. 4, 1967, pp. 241-254.
- 59 Ripperger, E. A., "Dynamic Plastic Behavior of Al, Cu, and Fe," Behavior Materials Under Dynamic Loading, Ed. Huffington, N. J., Jr., ASME, N. Y., 1965, pp. 62-80.
- 60 McLellan, D. L., "Constitutive Equations for Mechanical Properties of Structural Materials," AIAA Journal, Vol. 5, No. 3, 1967, pp. 446-450.
- 61 Willis, J. R., "Some Constitutive Equations Applicable to Problems of Large Dynamic Plastic Deformation," J. Mech. Phys. Solids, Vol. 17, No. 5, 1969, pp. 359-369.
- 62 Perzyna, P., "The Constitutive Equations for Rate Sensitive Plastic Materials," Quarterly of Applied Mathematics, Vol. 20, No. 4, 1963, pp. 321-332.
- 63 Cristescu, N., Dynamic Plasticity, North Holland Publishing Company, Amsterdam, 1967, pp. 614.
- 64 Rosenblatt, M., "Analytical Study of Strain-Rate Effects in Hypervelocity Impacts," NASA CR-61323, Jan. 1970.
- 65 Mobley, C. E., Jr., and Pond, R. B., "Energy Balances for Hypervelocity Targets," Proc. of the 7th Hypervelocity Impact Symp., Vol. 5, 1965, pp. 73-104.
- 66 Palmer, E. P., and Turner, G. H., "Energy Partitioning in High Velocity Impact Cratering in Lead," Proc. of the 7th Hypervelocity Impact Symp., Vol. 5, 1965, pp. 13-50.
- 67 Jean, B., and Rollins, T. L., "Radiation from Hypervelocity Impact Generated Plasma," AIAA Journal, Vol. 8, No. 10, 1970, pp. 1742-1747.
- 68 Davids, N., "Transient Analysis of Oblique Impact on Plates," J. Mech. Phys. Solids, Vol. 13, No. 4, 1965, pp. 199-212.

69 Kreyenhagen, K. K., Wagner, M. H., Piechock, J. J., and Bjork, R. L., "Ballistic Limit Determination in Impact on Multimaterial Laminated Targets," AIAA Journal, Vol. 8, No. 12, 1970, pp. 2147-2151.

70 McMillan, A. R., "An Investigation of the Penetration of Hypervelocity Projectiles Into Composite Laminates," Proc. of the 6th Symp. on Hypervelocity Impact, Vol. 3, 1963, pp. 309-356.

71 Nysmith, C. R., and Summers, J. L., "Preliminary Investigation of Impact on Multiple Sheet Structures and an Evaluation of the Meteoroid Hazard to Space Vehicles," NASA TN-D-1039, Sept. 1961.

72 Thomsen, E. G., Yang, C. T., and Kobayashi, S., Mechanics of Plastic Deformation in Metal Processing, The Macmillan Company, N. Y., 1965, pp. 486.

73 Taylor, G. I., and Quinney, H., "The Plastic Distortion of Metals," Philosophical Transactions of the Royal Society of London, Series A, Vol. 230, 1931, pp. 323-362.

74 Naghdi, P. M., Essenburg, F., and Koff, W., "An Experimental Study of Initial and Subsequent Yield Surfaces in Plasticity," Trans. of ASME, J. Appl. Mech., Vol. 25, No. 2, 1958, pp. 201-209.

75 Osgood, W. R., "Combined Stress Tests on 24S-T Aluminum Alloy Tubes," Trans. of ASME, J. Appl. Mech., Vol. 14, No. 2, 1947, pp. A-147-A-153.

76 Drucker, D. C., "Relation of Experiments to Mathematical Theories of Plasticity," Trans. of ASME, J. Appl. Mech., Vol. 16, No. 4, 1949, pp. 349-357.

77 Johnson, W., and Mellor, P. B., Plasticity for Mechanical Engineers, Van Nostrand Company, 1966, pp. 412.

78 Malvern, L. E., "The Propagation of Longitudinal Waves of Plastic Deformation in a Bar of Material Exhibiting a Strain-Rate Effect," Trans. of ASME, J. Appl. Mech., Vol. 18, 1951, pp. 203-208.

79 Rand, J. L., and Jackson, J. W., "The Split Hopkinson Pressure Bar," Behavior of Defense Media Under High Dynamic Pressures, IUTAM Symp. Gordon and Breach Company, N. Y., 1968, pp. 305-312.

80 Bell, J. F., "An Experimental Diffraction Grating Study of the Quasi-Static Hypothesis of the Split Hopkinson Bar Experiment," J. Mech. Phys. Solids, Vol. 14, No. 6, 1966, pp. 309-327.

81 Maiden, C. J., and Green, S. J., "Compressive Strain-Rate Tests on Six Selected Materials at Strain-Rates from 10^{-3} to 10^4 in/in/sec.," Trans. of ASME, J. Appl. Mech., Vol. 33, No. 3, 1966, pp. 496-504.

82 Hauser, F. E., Simmons, J. A., and Dorn, J. E., "Strain-Rate Effects in Plastic Wave Propagation," Response of Metals to High Velocity Deformation, Metallurgical Society Conferences, Vol. 9, Ed. Shewman, P. G., and Zackay, V. E., Interscience Publishers, N. Y., and London, 1960, pp. 93-114.

83 Karnes, C. H., and Ripperger, E. A., "Strain-Rate Effects in Cold Worked High Purity Aluminum," J. Mech. Phys. Solids, Vol. 14, 1966, pp. 75-88.

84 Loizou, N., and Sims, R. B., "The Yield Stress of Pure Lead in Compression," J. Mech. Phys. Solids, Vol. 1, 1953, pp. 234-243.

85 McQueen, R. G., Marsh, S. P., Taylor, J. W., Fritz, J. N., and Carter, W. J., "The Equations of State of Solids From Shock Wave Studies," High-Velocity Impact Phenomena, Ed. Kinslow, R., Academic Press, New York and London, 1970, pp. 293-417, 515-568.

86 Heyda, J. F., and Riney, T. D., "Peak Pressures in Thick Targets Generated by Reduced Density Projectiles," NASA CR-609.

87 Riney, T. D., and Heyda, J. F., "Hypervelocity Impact Calculations," Proc. of the 7th Hypervelocity Impact Symp., Vol. 2, 1965, pp. 77-185.

88 Lee, E. H., and Liu, D. T., "An Example of the Influence of Yield on High Pressure Wave Propagation," Stress Waves in Anelastic Solids, Ed. Kolsky, H., and Prager, W., IUTAM Symp., Springer-Verlag, 1964, pp. 239-254.

89 Cour-Palais, B. G., "Empirical Hypervelocity Equations developed for project Appolo," OART Meteoroid and Penetration Workshop, Manned Spacecraft Center, 1968, pp. 565-601.

APPENDIX A

STRESS DEVIATOR

In this Appendix, the stress deviator and its invariants are considered. Expressions for the second and third invariants of the deviatoric stress tensor for a general case can be derived as follows. When external forces are applied, a body deforms. The deformation of an elemental cube of such a body may be expressed as the sum total of the distortion or the change in shape and the volumetric deformation or the change in volume. The distortional part of the deformation can be attributed to the spherical or hydrostatic components of the stress tensor. In the following formulation symmetry of the various stress tensors is assumed. Unlike the strain tensor which is always symmetric, the stress tensor is not. But from practical considerations, the existence of body and surface couples is questionable. Thus in the nonpolar case, the symmetry of stress tensor is justified.

Deformation of an Elemental Cube. = Change in Shape or Distortion. + Change in Volume. (A.1)

Total Stress Tensor = Deviatoric Stress Tensor. + Hydrostatic or Spherical Stress Tensor. (A.2a)

$$\sigma_{ij} = \sigma'_{ij} + \sigma''_{ij}$$

$$\begin{bmatrix} \sigma_{11} & \sigma_{12} & \sigma_{13} \\ \sigma_{21} & \sigma_{22} & \sigma_{23} \\ \sigma_{31} & \sigma_{32} & \sigma_{33} \end{bmatrix} = \begin{bmatrix} \sigma_{11} - p & \sigma_{12} & \sigma_{13} \\ \sigma_{21} & \sigma_{22} - p & \sigma_{23} \\ \sigma_{31} & \sigma_{32} & \sigma_{33} - p \end{bmatrix} + \begin{bmatrix} p & 0 & 0 \\ 0 & p & 0 \\ 0 & 0 & p \end{bmatrix}$$

$$\text{where } p = \frac{\sigma_{11} + \sigma_{22} + \sigma_{33}}{3}$$

Letting J'_1 , J'_2 , and J'_3 to be the invariants of the deviatoric stress tensor, it follows that;

$$\begin{aligned} J'_1 &= \sigma'_{ii} = \sigma'_{11} + \sigma'_{22} + \sigma'_{33} \\ &= \sigma_{11} + \sigma_{22} + \sigma_{33} - 3p \end{aligned}$$

$$J'_1 = 0 \quad (A.3)$$

$$\begin{aligned} J'_2 &= \frac{1}{2} \sigma'_{ij} \sigma'_{ij} \\ &= \frac{1}{2} \{ (\sigma_{11} - p)^2 + \sigma_{12} \sigma_{21} + \sigma_{13} \sigma_{31} + \sigma_{21} \sigma_{12} + (\sigma_{22} - p)^2 \\ &\quad + \sigma_{22} \sigma_{32} + \sigma_{31} \sigma_{13} + \sigma_{32} \sigma_{23} + (\sigma_{33} - p)^2 \} \end{aligned}$$

$$\begin{aligned} J'_2 &= \frac{1}{3} (\sigma_{11}^2 + \sigma_{22}^2 + \sigma_{33}^2) - \frac{1}{3} (\sigma_{11} \sigma_{22} + \sigma_{22} \sigma_{33} + \sigma_{33} \sigma_{11}) \\ &\quad + (\sigma_{12}^2 + \sigma_{23}^2 + \sigma_{13}^2) \end{aligned} \quad (A.4a)$$

For the uniaxial state of stress J'_2 is therefore given by;

$$J_2' = \frac{\sigma_{11}^2}{3} \quad (\text{A.4b})$$

$$J_3' = \frac{1}{3} \sigma_{ij}' \sigma_{jk}' \sigma_{ki}' \quad (\text{A.5})$$

On simplification, equation (A.5) yields;

$$\begin{aligned} J_3' = & \frac{2}{27} (\sigma_{11}^3 + \sigma_{22}^3 + \sigma_{33}^3) - \frac{1}{9} (\sigma_{11}^2 \sigma_{22} + \sigma_{11} \sigma_{22}^2 + \sigma_{33}^2 \sigma_{11} + \sigma_{33} \sigma_{11}^2 \\ & + \sigma_{22}^2 \sigma_{33} + \sigma_{22} \sigma_{33}^2) + \frac{4}{9} \sigma_{11} \sigma_{22} \sigma_{33} + \frac{\sigma_{11}}{3} (\sigma_{12}^2 - 2 \sigma_{23}^2 + \sigma_{13}^2) \\ & + 2 \sigma_{12} \sigma_{23} \sigma_{13} + \frac{1}{3} \sigma_{22} (\sigma_{12}^2 - 2 \sigma_{13}^2 + \sigma_{23}^2) \\ & + \frac{\sigma_{33}}{3} (\sigma_{13}^2 - 2 \sigma_{12}^2 + \sigma_{23}^2) \end{aligned} \quad (\text{A.5b})$$

For the uniaxial state of stress, J_3' is therefore given by;

$$J_3' = \frac{2}{27} \sigma_{11}^3 \quad (\text{A.5c})$$

If the tensor components are expressed in terms of principal stresses, then equation (a.2) can be written as follows;

$$\begin{bmatrix} \overline{\sigma}_{11} & 0 & 0 \\ 0 & \overline{\sigma}_{22} & 0 \\ 0 & 0 & \overline{\sigma}_{33} \end{bmatrix} = \begin{bmatrix} \overline{\sigma}_{11} - p & 0 & 0 \\ 0 & \overline{\sigma}_{22} - p & 0 \\ 0 & 0 & \overline{\sigma}_{33} - p \end{bmatrix} + \begin{bmatrix} p & 0 & 0 \\ 0 & p & 0 \\ 0 & 0 & p \end{bmatrix} \quad (\text{A.6})$$

Once again letting J_1' , J_2' , and J_3' to be the invariants of the deviatoric stress tensor, it follows that;

$$J'_1 = \sigma'_{ii} = 0 \quad (\text{A.7})$$

$$J'_2 = \frac{1}{2} \sigma'_{ij} \sigma'_{ji}$$

$$J'_2 = \frac{1}{3} (\overline{\sigma_{11}^2} + \overline{\sigma_{22}^2} + \overline{\sigma_{33}^2}) - \frac{1}{3} (\overline{\sigma_{11} \sigma_{22}} + \overline{\sigma_{22} \sigma_{33}} + \overline{\sigma_{33} \sigma_{11}}) \quad (\text{A.8})$$

$$J'_3 = \frac{2}{27} (\overline{\sigma_{11}^3} + \overline{\sigma_{22}^3} + \overline{\sigma_{33}^3}) - \frac{1}{9} (\overline{\sigma_{11}^2 \sigma_{22}} + \overline{\sigma_{11} \sigma_{22}^2} + \overline{\sigma_{33}^2 \sigma_{11}} + \overline{\sigma_{33} \sigma_{11}^2} + \overline{\sigma_{22}^2 \sigma_{33}} + \overline{\sigma_{22} \sigma_{33}^2}) + \frac{4}{9} \overline{\sigma_{11} \sigma_{22} \sigma_{33}} \quad (\text{A.9})$$

For elastic deformations, the stress and strain tensors are related in terms of modulus of rigidity μ measuring the change in shape, and bulk modulus K measuring the change of volume as follows;

$$\sigma_{ij} = \sigma'_{ij} + \sigma''_{ij}$$

$$\epsilon_{ij} = \epsilon'_{ij} + \epsilon''_{ij}$$

$$\sigma_{ij} = 2 \mu \epsilon_{ij} + (K - \frac{2}{3} \mu) \epsilon_{ii} \delta_{ij}$$

$$\sigma'_{ij} = 2 \mu \epsilon'_{ij}$$

$$\sigma''_{ij} = 3 K \epsilon''_{ij} \quad \text{or} \quad \sigma''_{ii} = 3 K \epsilon''_{ii}$$

APPENDIX B

CALCULATION OF STRAIN RATES

Outline of the Procedure

A sample calculation for determining the strain rates is shown here for target number 6-147. This is a 6061 Al. alloy target impacted with a pyrex sphere of 0.04 cm. diameter at 6.03 km/sec. The initial impact Hugoniot values of the peak pressure and the particle velocity were determined by the graphical impedance matching technique. Then the distance along the axis of symmetry and the corresponding time for the steady state regime were calculated. The attenuation of the peak pressure of the advancing shock front based on hydrodynamic considerations was then calculated. This hydrodynamic analysis was terminated for 6061 Al. alloy targets when the peak pressure of the advancing shock front had decayed to 0.18 megabars. At this stage the material strength effects were introduced. The tail associated with a shock front was then computed. Assuming a linearly decaying stress before plastic unloading initiates at the position where material strength effects are introduced, the stress and particle velocity immediately behind the advancing shock wave were calculated which permitted the determination of strain rates.

Target number: 6-147

Target material: 6061 Al. alloy

Projectile material: Pyrex

Projectile diameter: 0.040 cm.

Projectile velocity: 6.03 km/sec.

Initial Impact Hugoniot values

From the graphical impedance matching technique which consisted of drawing p-vs- U_p shock Hugoniot of the target material and the reflected p-vs- U_p Shock Hugoniot of the projectile material, the following initial impact Hugoniot values were obtained from Figure B.1. By referring to the Hugoniot properties of the materials, the following shock speeds were obtained;

$$V_p = U_{pti} + U_{ppi}$$

$$p_i = 0.579 \text{ megabars}$$

$$U_{pti} = 2.435 \text{ km/sec.}$$

$$U_{ppi} = 3.595 \text{ km/sec.}$$

$$U_{Sti} = 8.572 \text{ km/sec.}$$

$$U_{Spi} = 7.219 \text{ km/sec.}$$

These initial values remain undisturbed until rarefactions from the rear periphery of the projectile catch up with the advancing shock front in the target.

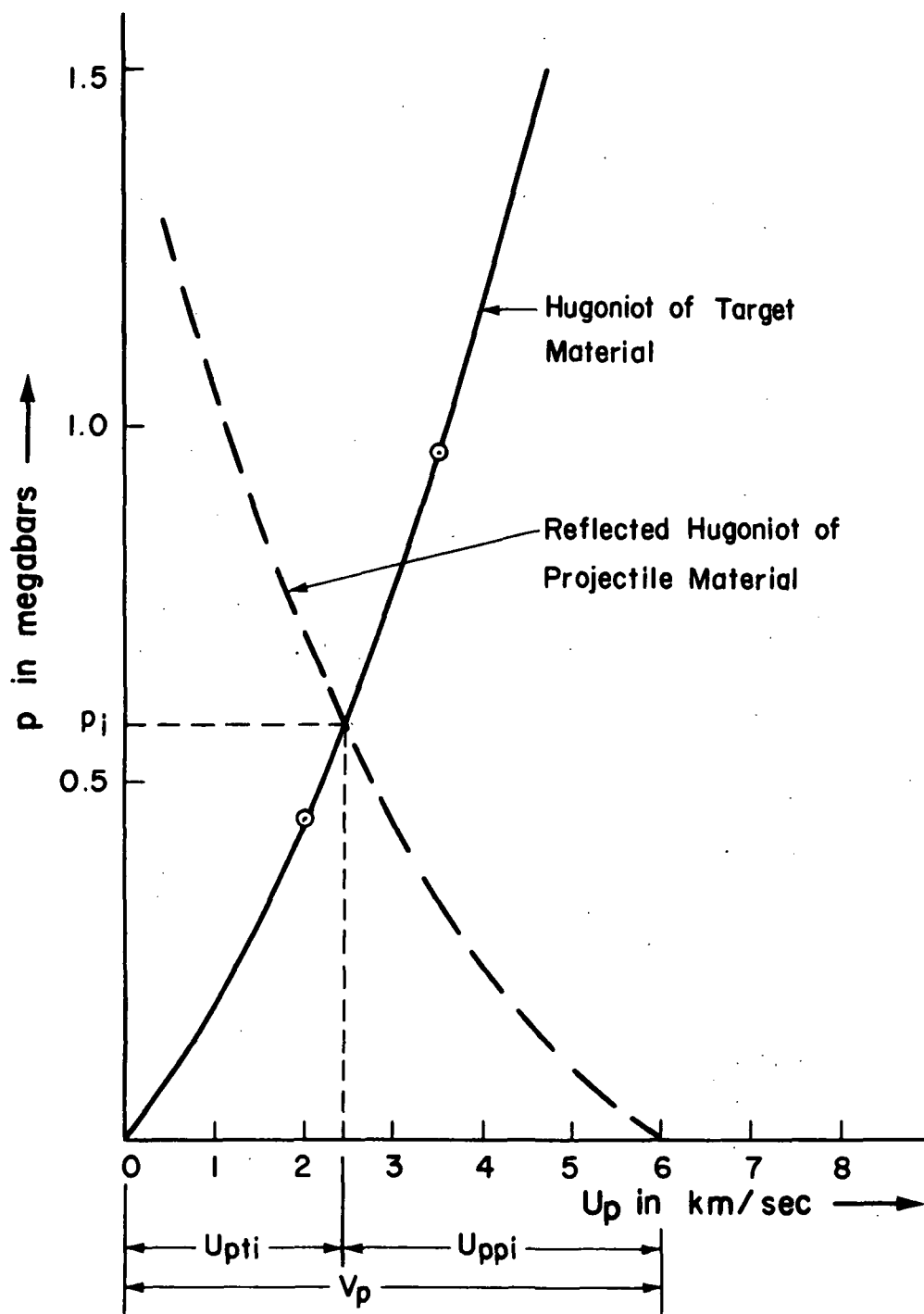


Fig. B-1 Graphical Impedance Matching

Calculations of the Steady state Regime

Since $V_p < U_{spi}$ equations (7.5&7.6) were used to compute the time and the corresponding distance along the axis of symmetry where the rarefactions catch up with the chock wave in the target.

From the isentropic properties of the materials, the following velocities were obtained for the rarefaction wave in the shock compressed projectile and target materials;

$$c_{rp} = \sqrt{\left(\frac{\partial p}{\partial \rho}\right)_s} = 15.847 \text{ km/sec}$$

$$c_{rt} = \sqrt{\left(\frac{\partial p}{\partial \rho}\right)_s} = 8.413 \text{ km/sec.}$$

$$t_1 = \left(\frac{c_{rt}}{c_{rp}}\right) \left[\frac{d_p}{U_{spi} + V_p}\right] \left[\frac{U_{pti} + U_{spi} + c_{rp}}{U_{pti} + c_{rt} - U_{sti}}\right]$$

$$t_1 = 0.178 \text{ } \mu \text{ sec.}$$

$$Z_1 = (U_{sti}) t_1$$

$$Z_1 = 0.153 \text{ cm.}$$

Attenuation of the peak pressure

Based on hydrodynamic and blast wave considerations, the various constants needed for the calculation of peak pressure as affected by rarefactions were calculated as follows:

$$\bar{L} = \frac{d_p}{2} (2)^{1/3} = 0.025 \text{ cm.}$$

$$K_1 = 0.368 \left[1 + 0.15 \left(1 - \frac{\rho_{op}}{\rho_{ot}} \right) \right] \left\{ \frac{v_p}{c_{oh}} \right\}^{-1/3}$$

The Hugoniot intercept c_{oh} of the U_{st} -vs- U_{pt} Shock Hugoniot is

$$c_{oh} = 5.20 \text{ km/sec.}$$

$$K_1 = 0.368 \left[1 + 0.15 \left(1 - \frac{2.230}{2.785} \right) \right] \left\{ \frac{6.03}{5.20} \right\}^{-1/3}$$

$$K_1 = 0.361$$

$$k_1 = K_1 \sqrt{\bar{L}} = 0.057 \sqrt{\text{cm}}$$

$$d_1 = \frac{p_i}{p_i + \left[1 - \frac{\rho_{ot}}{\rho_t} \right] p_i'} ; d_2 = \frac{2 p_i'}{\left[1 - \frac{\rho_{ot}}{\rho_t} \right] p_i''}$$

$$\text{At } p_i = 0.579 \text{ megabars, } \frac{\rho_{ot}}{\rho_t} = 0.717$$

$$p_i' = \left(\frac{\partial p}{\partial \frac{\rho_{ot}}{\rho_t}} \right)_H = 3.8 \text{ megabars}$$

$$p_i'' = \left(\frac{\partial p_i'}{\partial \frac{\rho_{ot}}{\rho_t}} \right)_H = -18.846 \text{ megabars}$$

$$d_1 = -1.168$$

$$d_2 = 1.427$$

$$\beta = 4 d_1 \left(1 - \frac{d_1}{d_2}\right)$$

$$\beta = -8.499$$

$$A_1 = U_{sti} \left\{ \frac{51 - 44\beta + 8\beta^2 - 3\sqrt{33 - 8\beta}}{8(1 - \beta)(4 - \beta)} \right\}$$

$$A_1 = 9.81 \text{ km/sec.}$$

$$Z_0 = Z_1 - \left[\frac{2 K_1}{1 - \sqrt{\frac{U_{sti}}{A_1} + 1}} \right]^2 \bar{L}$$

$$Z_0 = 0.121 \text{ cm.}$$

Now, the speed of the shock wave as a function of distance is given by;

$$U_{st}(z) = \frac{4 A_1 k_1}{\sqrt{z - z_0}} - \frac{4 A_1 k_1^2}{z - z_0}$$

$$U_{st}(z) = \frac{2.238}{\sqrt{z - z_0}} - \frac{0.128}{z - z_0}$$

$$\dot{\epsilon} \approx \frac{\Delta U}{\Delta Z}$$

Using this equation shock speeds were calculated for different distances, Z . From the Hugoniot properties of the target material, the corresponding pressures and particle velocities were obtained. This enabled the determination of strain rates. This hydrodynamic analysis was terminated when the peak pressure dropped to 0.18 megabars in the case of 6061 Al. alloy targets.

Z cm	U_{st} km/sec	p Magabars	U_p km/sec	$\epsilon \times 10^{-6}$ sec. ⁻¹
0 to 0.153	8.572	0.579	2.435	4.477
0.172	7.429	0.326	1.573	2.985
0.192	6.610	0.180	0.970	

Material Strength Effects

Letting Y to be the dynamic stress under high pressure compression for a plate with lateral expansion prevented, the following calculation were made;

Modulus of rigidity = $\mu = 258.6$ kilobars

At $p = 180$ kilobars; $\frac{\rho_{ot}}{\rho_t} = 0.854$

$$\bar{e}_{zz} = 1 - 0.854 = 0.146$$

Slope of p -vs- $\frac{\rho_o}{\rho}$ isentrope = $k_s = 1690$ kilobars

$$2Y = Y_o \left[\frac{4}{3} + \frac{k_s}{\mu} (1 - \bar{e}_{zz}) \right]$$

$$Y_o = 2.517 \text{ kilobars}$$

$$2Y = 17.411 \text{ kilobars; } \frac{2}{3} Y = 11.607 \text{ kilobars}$$

$$c_0 = \frac{k_s + \frac{4}{3} \frac{\mu}{(1-\frac{\mu}{2z})}}{\rho}$$

$$c_0 = 8.009 \text{ km/sec.}$$

$$c_1 = \sqrt{\frac{k_s}{\rho}}$$

$$c_1 = 7.196 \text{ km/sec}$$

$$c_2 = \frac{p}{U_p}$$

$$c_2 = \frac{180}{0.94} = 5.867 \text{ km/sec.}$$

$$c_2' = U_{st} \text{ (at } p = 180 \text{ kilobars)}$$

$$c_2' = 6.610 \text{ km/sec.}$$

$$c_3 = 5.478 \text{ km/sec.}$$

The computations for the tail behind the shock wave with a peak of 175 kilobars are as follows and are shown in Figure B.2.

p kilobars	t μsec.	Δt μsec.
180	0.251144853	
175	0.251591821	0.00045

At $p = 175$ kilobars;

$$\frac{U_p + c}{U_{st}} - 1 = \frac{7.93}{6.60} - 1$$

$$= 0.2015151520$$

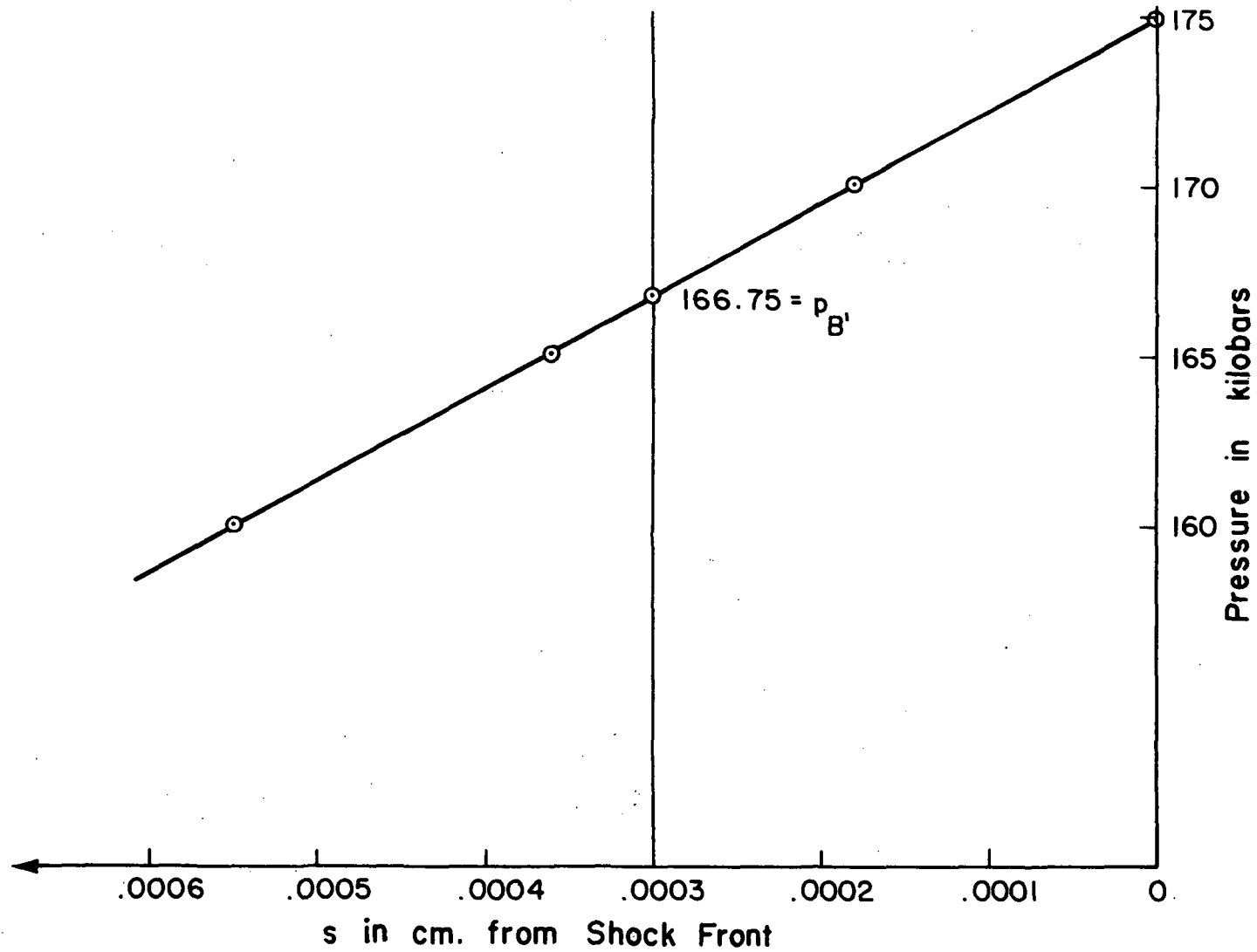


Fig. B-2 Tail of the Shock Wave

$$\Delta S = \Delta Z \frac{U + c}{U_{st}} - 1$$

P Kilobars	ΔZ cm.	ΔS cm.
175		
170	0.00089	0.00018
165	0.00180	0.00036
160	0.00272	0.00055

$$U_{st} \Delta t = 6.61 (.00045) = .000295 \text{ cm.}$$

The attenuation constants A_3 and B_3 were calculated as follows;

$$A_3 = 180 - \frac{2}{3}Y = 168.393 \text{ kilobars}$$

$$q_{B'} = p_{B'} - \frac{2}{3}Y = 155.143 \text{ kilobars}$$

$$A_3 - B_3 (\Delta t) = 155.143$$

$$B_3 = \frac{13.25000}{0.00045} = 29,644.18 \frac{\text{kilobars}}{\mu\text{sec.}}$$

The stress immediately behind the shock wave is given by

$$\overline{\sigma_{zz}}(t) = 168.393 - 5771.366 (t - t_m)$$

For $t - t_m = 0.01, 0.02 \mu\text{sec.}$, the stresses were calculated.

$$U_p = \frac{\sigma_{zz}}{\rho c_2^2}$$

Z cm.	σ Kilobars	U_p km/sec.	$\dot{\epsilon}$ sec. ⁻¹
0.199	110.680	0.535	
			4.018x10 ⁶
0.205	52.970	0.270	

Strain Rates

The strain rates, produced by hypervelocity impact of a projectile on semi-infinite target considering the effects of rarefaction and material strength for the various projectile target combinations that were experimented, are listed in the following tables. The calculations as outlined above are performed on these targets. The results presented in these tables are the values along the axis of symmetry. The projectiles used are pyrex sheres. In the following tables, the units are as follows.

Z	in cm.
U_{st}	in km/sec.
p	in megabars
$\bar{\sigma}_{zz}$	in kilobars
U_p	in km/sec.
$\dot{\epsilon}$	in sec. ⁻¹

Shot number: 6-106

Target material: 1100 Aluminum

Projectile diameter = $d_p = 0.159$ cm.Projectile velocity = $V_p = 5.580$ km/sec.

Z cm.	U_{st} km/sec.	p megabars	$\bar{\sigma}_{zz}$ kilobars	U_p km/sec.	$\dot{\epsilon} \times 10^{-6}$ sec. ⁻¹
0 to 0.635	8.300	0.513	-	2.226	
					1.126
0.655	8.007	0.402		2.000	1.139
0.675	7.704	0.381		1.773	1.046
0.695	7.416	0.324		1.564	0.990
0.715	7.151	0.271		1.366	0.922
0.735	6.910	0.228		1.181	0.827
0.755	6.690	0.190		1.016	0.727
0.781	6.430	0.150		0.825	0.637
0.818	6.110	0.100		0.590	
0.824	"		80.90	0.438	1.484
0.830	"		63.27	0.347	1.517
0.837	"		45.65	0.254	1.553
0.845	"		28.03	0.159	1.616
0.849	"		10.41	0.061	

(Hydrodynamic)
considerationsStrength
Effects

Shot number: 6-117

Target material: 1100 Aluminum

Projectile diameter: 0.1 cm.

Projectile velocity: 5.59 km/sec.

Z	U_{st}	p	$\bar{\sigma}_{zz}$	U_p	$\dot{\epsilon} \times 10^{-6}$
0 to 0.396	8.310	0.523		2.233	
0.420	7.740	0.390		1.802	1.788
0.440	7.290	0.298		1.472	1.652
0.460	6.897	0.226		1.171	1.504
0.480	6.558	0.168		0.919	1.262
0.489	6.420	0.150		0.818	1.119
0.512	6.110	0.100		0.590	1.010
0.512	6.110		79.51	0.430	1.583
0.524	"		60.51	0.333	1.640
0.530	"		41.50	0.233	1.701
0.536	"		22.49	0.129	1.772
0.542	"		3.49	0.020	

Shot number: 6-161

Target material: 1100 Aluminum

Projectile diameter: 0.159 cm.

Projectile velocity: 8.3 km/sec.

Z	U_{st}	P	$\bar{\sigma}_{zz}$	U_p	$\dot{\epsilon} \times 10^{-6}$
0 to 0.456	9.972	0.963		3.500	
0.480	9.414	0.800		3.053	1.999
0.500	8.927	0.670		2.764	1.446
0.520	8.492	0.560		2.370	1.971
0.540	8.109	0.470		2.078	1.457
0.560	7.771	0.396		1.826	1.263
0.580	7.472	0.334		1.604	1.109
0.600	7.206	0.282		1.408	0.983
0.620	6.966	0.240		1.224	0.917
0.640	6.750	0.200		1.060	0.821
0.660	6.553	0.149		0.916	0.722
0.680	6.373	0.123		0.783	0.661
0.713	6.110	0.100		0.590	0.593
0.713	6.110		98.00	0.590	
0.719			42.59	0.279	5.090

Shot number: 6-162

Target material: 1100 Aluminum

Projectile diameter: 0.159 cm.

Projectile Velocity: 8.33 km/sec.

Z	U_{st}	p	$\bar{\sigma}_{zz}$	U_p	$\dot{\epsilon} \times 10^{-6}$
0 to 0.457	9.988	0.968		3.515	2.013
0.480	9.411	0.800		3.051	1.797
0.500	8.923	0.668		2.691	1.621
0.520	8.488	0.559		2.367	1.457
0.540	8.105	0.468		2.076	1.261
0.560	7.768	0.385		1.824	1.107
0.580	7.470	0.334		1.602	0.983
0.600	7.203	0.281		1.406	0.916
0.620	6.964	0.237		1.223	0.820
0.640	6.748	0.200		1.059	0.721
0.660	6.551	0.167		0.914	0.660
0.680	6.372	0.139		0.782	0.593
0.712	6.110	0.100		0.590	
0.712	"		98.00	0.590	
0.719	"		42.58	0.278	5.106

Shot number: 6-108

Target material: 6061 Al. alloy.

Projectile diameter: 0.159 cm.

Projectile velocity: 5.60 km/sec.

Z	U_{st}	p	$\bar{\sigma}_{zz}$	U_p	$\dot{\epsilon} \times 10^{-6}$
0 to 0.823	8.337	0.523		2.335	1.372
0.843	8.094	0.466		2.060	1.115
0.863	7.787	0.400		1.838	1.088
0.883	7.494	0.339		1.620	0.989
0.903	7.225	0.285		1.422	0.943
0.923	6.979	0.240		1.234	0.776
0.957	6.610	0.180		0.970	
0.963	"		144.38	0.669	1.962
0.970	"		113.75	0.539	2.288
0.976	"		83.11	0.388	1.896
0.983	"		52.48	0.263	2.260
0.990	"		21.84	0.113	

Shot number: 6-124

Target material: 6061 Al. alloy

Projectile diameter: 0.100 cm.

Projectile velocity: 6.140 km/sec.

Z	U_{st}	p	$\bar{\sigma}_{zz}$	U_p	$\dot{\epsilon} \times 10^{-6}$
0 to 0.708	8.736	0.620		2.547	1.885
0.720	8.429	0.549		2.325	2.000
0.740	7.898	0.422		1.924	1.613
0.760	7.428	0.331		1.602	1.517
0.780	7.025	0.254		1.298	1.346
0.804	6.610	0.180		0.970	
0.811	"		140.26	0.668	2.111
0.818	"		109.62	0.529	2.023
0.824	"		78.99	0.395	2.215
0.831	"		48.35	0.248	2.334
0.837	"		17.72	0.094	

Shot number: 6-147
 Target material: 6061 Al. alloy
 Projectile diameter: 0.040 cm.
 Projectile velocity: 6.03 km/sec.

Z	U_{st}	p	$\bar{\sigma}_{zz}$	U_p	$\dot{\epsilon} \times 10^{-6}$
0 to 0.153	8.572	0.579		2.435	
0.172	7.430	0.326		1.573	4.477
0.192	6.610	0.180		0.970	2.985
0.199	"		110.68	0.535	
0.205	"		52.97	0.270	4.018

Shot number: 6-111
 Target material: Mild Steel
 Projectile diameter: 0.159 cm.
 Projectile velocity: 5.62 km./sec.

Z	U_{st}	p	$\bar{\sigma}_{zz}$	U_p	$\dot{\epsilon} \times 10^{-6}$
0 to 0.419	6.268	0.728		1.479	0.566
0.439	6.067	0.652		1.366	0.614
0.459	5.848	0.568		1.243	0.604
0.479	5.637	0.496		1.122	0.570
0.499	5.440	0.432		1.008	0.515
0.519	5.260	0.376		0.905	0.461
0.539	5.095	0.328		0.813	0.416
0.559	4.944	0.285		0.730	0.373
0.579	4.805	0.250		0.655	0.336
0.610	4.610	0.200		0.550	
0.628	"		166.78	0.412	0.355
0.647	"		138.17	0.346	0.366
0.665	"		109.56	0.279	0.372
0.684	"		80.95	0.210	0.443
0.702	"		52.34	0.139	0.403
0.721	"		23.73	0.064	

Shot number: 6-147

Target material: Mild steel

Projectile diameter: 0.10 cm.

Projectile velocity: 6.13 km/sec.

Z	U_{st}	p	$\bar{\sigma}_{zz}$	U_p	$\dot{\epsilon} \times 10^{-6}$
0 to 0.216	6.555	0.850		1.700	1.397
0.240	6.077	0.654		1.372	1.065
0.260	5.700	0.518		1.159	0.936
0.280	5.377	0.412		0.972	0.776
0.300	5.101	0.303		0.816	0.651
0.320	4.863	0.265		0.686	0.549
0.345	4.610	0.200		0.550	
0.354	"		170.50	0.421	0.675
0.363	"		145.62	0.364	0.632
0.372	"		120.73	0.306	0.649
0.382	"		95.84	0.246	0.655
0.391	"		70.95	0.185	0.680
0.400	"		46.07	0.123	0.706
0.409	"		21.18	0.058	

Shot number: 6-109

Target material: Lead

Projectile diameter: 0.159 cm.

Projectile velocity: 5.27 km/sec.

Z	U_{st}	p	$\bar{\sigma}_{zz}$	U_p	$\dot{\epsilon} \times 10^{-6}$
0 to 0.245	4.100	0.670		1.365	0.805
0.260	3.913	0.588		1.242	0.723
0.280	3.678	0.492		1.088	0.675
0.300	3.472	0.407		0.953	0.581
0.320	3.295	0.334		0.837	0.515
0.340	3.142	0.281		0.734	0.422
0.360	3.008	0.235		0.649	0.350
0.380	2.891	0.190		0.580	0.300
0.400	2.786	0.150		0.510	0.226
0.420	2.693	0.135		0.450	0.226
0.442	2.600	0.100		0.400	0.197
0.493	2.420	0.050		0.300	
0.498	"		44.61	0.141	0.283
0.502	"		39.59	0.127	0.279
0.507	"		34.57	0.113	0.324
0.512	"		29.56	0.098	0.340

0.517	"	24.54	0.081	0.341
0.521	"	19.52	0.065	0.327
0.527	"	14.51	0.049	0.332
0.531	"	9.49	0.033	0.356
0.536	"	4.48	0.016	

Shot number: 6-127

Target material: Lead

Projectile diameter: 0.10 cm.

Projectile velocity: 6.12 km/sec.

Z	U_{st}	p	$\bar{\sigma}_{zz}$	U_p	$\dot{\epsilon} \times 10^{-6}$
0 to 0.143	4.543	0.850		1.650	1.519
0.160	4.136	0.690		1.388	1.290
0.180	3.742	0.510		1.130	0.996
0.200	3.439	0.380		0.931	0.704
0.220	3.199	0.300		0.790	0.700
0.240	3.004	0.240		0.650	0.450
0.260	2.842	0.175		0.560	0.400
0.280	2.705	0.130		0.480	0.350
0.300	2.586	0.100		0.410	0.300
0.320	2.482	0.065		0.350	0.250
0.333	2.420	0.050		0.300	
0.337	"		30.71	0.101	1.649
0.341	"		11.80	0.041	

VITA

Basavaraju Chakrapani [REDACTED]

[REDACTED] His parents are Mr. B. Atchyuta Rao and Mrs. B. [REDACTED]. After graduation with a first rank from MVRZP High School at Aukiripalli in March 1960, he studied at SRR & CVR Govt. College, Vijayawada and passed the Pre-University examination with first class and with a second rank in the college. He received his B. E. degree in Mechanical Engineering with a first class-distinction from Andhra University in May 1967. He was awarded Smt. Sushilabai Sadasiva Rao Merit Prize for Engineering students. He received the Govt. of India National Merit Scholarship during the period 1962-67 and the Govt. of India Post Graduate Scholarship during the period 1967-69. The author received his M. Tech. degree in Mechanical Engineering from Indian Institute of Technology in July 1969. The author joined the graduate college of Texas A&M University in September 1969 to pursue his doctoral studies in Mechanical Engineering. In the course of obtaining his doctor's degree, he was sponsored by a NASA Research Grant to work in the area of Hypervelocity Impact Effects.

The author was married to Lakshmi Nagaratnam on February 10, 1966. The author's permanent address in India is Edara; (Via) Aukiripalli, Krishna Dist., A.P., India.

The typist for this dissertation was Mrs. Donna Gallt.